DEVELOPMENT OF A HIGH CONCENTRATION SOLAR FLUX MAPPING SYSTEM

Brandon Luke van Bakel

In fulfilment of the academic requirements for the degree of Master of Science in Mechanical Engineering, College of Agriculture, Engineering and Science, University of KwaZulu-Natal

December 2018

Examiner's copy

Supervisor: Dr. Michael. J. Brooks

Co-Supervisor: Mr. Jean-Francois Pitot de la Beaujardiere

DECLARATION 1– PLAGIARISM

I, Brandon Luke van Bakel, declare that:

1. The research reported in this thesis, except where otherwise indicated, is my original research.

2. This thesis has not been submitted for any degree or examination at any other university.

3. This thesis does not contain other persons' data, pictures, graphs or other information, unless specifically acknowledged as being sourced from other persons.

4. This thesis does not contain other persons' writing, unless specifically acknowledged as being sourced from other researchers. Where other written sources have been quoted, then:

    a. Their words have been re-written but the general information attributed to them has been referenced

    b. Where their exact words have been used, then their writing has been placed inside quotation marks, and referenced.

5. This thesis does not contain text, graphics or tables copied and pasted from the Internet, unless specifically acknowledged, and the source being detailed in the thesis and in the References sections.

Signed:_____ Date: _____

Mr. Brandon Luke van Bakel

As the candidate's supervisor, I have approved this dissertation for

submission. Signed:_____ Date: _____

Dr. Michael Brooks

As the candidate's co-supervisor, I have approved this dissertation for

submission. Signed:_____ Date: _____

Mr. Jean-Francois Pitot de la Beaujardiere

DECLARATION 2 – PUBLICATIONS

van Bakel, B.L, Brooks, M.J & Pitot de la Beaujardiere, J.P, (2016). Development of a High Concentration Solar Flux Mapping Method. In: *The 4th Southern African Solar Energy Conference*. Stellenbosch, Cape Town, 31 October - 2 November.

van Bakel, B.L, Brooks, M.J & Pitot de la Beaujardiere, J.P, (2018). Description of the SERAFF Target Irradiance System (STIMS) for characterisation of concentrated solar flux. In: *The 5th Southern African Solar Energy Conference*. Durban, South Africa, 25 - 27 June.

Signed:_____ Date: _____

Mr. Brandon Luke van Bakel

ACKNOWLEDGEMENTS

I would sincerely like to thank my supervisor, Dr. Michael Brooks and co-supervisor, Mr. Jean-Francois Pitot de la Beaujardiere for their mentorship and guidance during my studies. You have both been exemplary role models to learn from.

To my peers from the GSET, ASREG and EMERG research groups, these past few years have been enjoyable and I have learnt so much from each of you. I will never forget the memories of fun and mischief times we have shared together. Thank you for making this experience that much more enjoyable.

My thanks go out to the SERAFF final year project groups of 2016, 2017 and 2018 and the workshop technicians for your commitment in seeing this project achieve its goals.

Lastly, to my friends and family. Thank you all for your support, love and motivation through this experience.

ABSTRACT

The Group for Solar Energy Thermodynamics (GSET) is in the process of commissioning the Solar Energy Research Amplified Flux Facility (SERAFF), which is South Africa's first solar furnace facility. SERAFF is situated at the University of KwaZulu-Natal's Howard College campus and assumes an on-axis optical configuration, comprising a 9 m^2 non-focusing heliostat reflector, a 3 m diameter paraboloidal dish concentrator and a test article platform. The facility was designed to aid research in the fields of high temperature materials testing, concentrating solar energy and solar thermochemistry. The concentrated radiative energy output of a solar furnace establishes the energy input to prototype receivers, reactors or materials that aim to be tested using the facility.

The challenge is compounded by the temporal and spatial variation of SERAFF's radiative energy output, influenced by weather-related and geometric factors. In this study, an indirect spatial flux mapping system is developed to characterise SERAFF's spatial radiative energy output. SERAFF's theoretical spatial radiative energy output is estimated through Monte Carlo ray-tracing techniques to provide benchmark performance parameters including total thermal power output, peak concentration ratio and focal spot size. The indirect system uses optical measurement techniques, in which spatial solar flux is measured via diffuse reflection off a Lambertian target using a digital CMOS camera through a neutral density filter and lens. Pixel intensities are calibrated against reference measurements acquired from a circular-foil Gardon gauge heat flux transducer. The calibrated CMOS camera can be used to measure values of radiative flux, incident at the focal plane from 0 kW/m^2 - 468.19 kW/m^2.

Measurements were restricted to a brief testing period and are not representative of SERAFF's peak operating conditions. Spatial flux measurements indicated a thermal power output of 3.83 kW, with a corresponding peak solar flux of 227.8 kW/m^2 within a focal diameter of 250 mm. The study demonstrated successful integration of an indirect spatial flux mapping system into the SERAFF solar furnace.

TABLE OF CONTENTS

DECLARATION 1– PLAGIARISM i

DECLARATION 2 – PUBLICATIONS ii

ACKNOWLEDGEMENTS iii

ABSTRACT iv

TABLE OF CONTENTS v

LIST OF FIGURES viii

LIST OF TABLES xii

NOMENCLATURE xiii

Chapter 1 Introduction 1

1.1 Solar furnace operating principles 1

1.1.1 Solar Energy Research Amplified Flux Facility (SERAFF) 2

1.1.2 Solar flux characterisation techniques 3

1.1.3 Assessment of solar flux characterisation techniques 6

1.2 Research objectives 8

1.3 Methodology 9

1.4 Thesis outline 10

Chapter 2 SERAFF optical performance modelling 11

2.1 Monte Carlo ray-tracing analysis 11

2.2 SERAFF ray-tracing model 11

2.2.1 Sunshape model 12

2.2.2 Direct normal irradiance and observer-sun angles 13

2.2.3 Optical errors 14

2.2.3 Ray-tracing results 16

Chapter 3 SERAFF target irradiance mapping system 18

3.1 Indirect flux characterisation 18

3.2 Imaging sensors 18

3.3 Image sensor characteristics 21

3.3.1 Pinned photodiode 21

3.3.2 Dark current 22
3.3.2 Quantum efficiency 23
3.3.3 Full-well capacity 23
3.3.4 Vignetting 24
3.4 Lambertian diffusion 24
3.4.1 Lambert's law of diffuse reflection 24
3.4.2 Lambertian target design 27
3.4.3 Transient heat transfer analysis 30
3.4 Actively-cooled Lambertian target design 32
3.4.1 Conjugate heat transfer analysis 32
3.4.3 Lambertian target fabrication 39
3.5 Target Positioning System 40
Chapter 4 Measurement methods and instrumentation 44
4.1. CMOS camera photo response characterisation 44
4.2. Image sensor light intensity attenuation 47
4.3 Image size minimisation process 49
4.4 Calibration methods 51
4.4.1 Spatial correction 52
4.4.2 Circular foil Gardon gauge 55
4.4.3 Directional considerations 56
4.4.4 Pixel intensity calibration 56
Chapter 5 SERAFF measured performance 64
5.1 SERAFF target irradiance mapping system (STIMS) 64
5.2 Spatial flux characterisation 66
5.3 Pixel measurement errors 73
Chapter 6 Conclusion 75
References 78
APPENDIX A Ray-tracing simulation results 85
APPENDIX B Water-cooled Lambertian target CAD drawings 86

APPENDIX C Target positioning system user interface 88
APPENDIX D CMOS camera photo response images 89
APPENDIX E Region of interest user interface 91
APPENDIX F Gardon gauge calibration certificate 93
APPENDIX G Spatial flux plots 95

LIST OF FIGURES

Figure 1-1: Solar furnace operation schematic 2
Figure 1-2: SERAFF solar furnace system components 2
Figure 2-1: Ray-tracing simulation procedure diagram 12
Figure 2-2: Coordinate system for describing azimuth and elevation angles in the southern hemisphere 13
Figure 2-3: SERAFF site location on Cato Manor reservoir situated within Howard College 14
Figure 2-4: Illustration of surface slope error (a) and surface specularity error (b) 15
Figure 2-5: Theoretical Near-Gaussian solar flux intensity distribution at the focal plane of a parabolic dish concentrator 15
Figure 2-6: SERAFF spatial flux distribution at the focal plane for (a) the summer solstice (22 December) at 11:58 am and (b) the winter solstice (22 June) at 11:54 am 16
Figure 3-1: Indirect flux mapping system design workflow diagram 18
Figure 3-2: The effective spectral composition of sunlight at sea level for a clear-sky day. The dotted curve indicates the extraterrestrial spectrum 19
Figure 3-3: Sequential charge-coupled transfer method for a CCD camera 20
Figure 3-4: Simultaneous readout method of a CMOS camera 20
Figure 3-5: Photodiode photon excitation diagram 22
Figure 3-6: Quantum efficiency curve for a CMOS APS image sensor 23
Figure 3-7: Diffuse-reflection off a Lambertian surface 24
Figure 3-8: Diffuse-reflected irradiance on a small portion of a Lambertian surface detected by a single pixel element 25
Figure 3-9: Solid angle subtended from a portion of a Lambertian diffuser to the camera iris 25
Figure 3-10: Illustration of the bidirectional reflectance distribution function (BRDF) 26
Figure 3-11: CAD model of SERAFF's 3 m diameter parabolic concentrator and the petal adjustment mechanism assembly 28
Figure 3-12: Non-dimensional radiative intensity distribution on a 500 mm x 500 mm refractory board after the petal alignment procedure 28
Figure 3-13: Lambertian target design workflow diagram 29
Figure 3-14: Maximum temperature on the aluminium substrate from 0 s to 300 s 31
Figure 3-15: Temperature distribution on the front face of the aluminium substrate after 300 s 32
Figure 3-16: Illustration of the fluid and solid domains for the Lambertian target conjugate heat transfer assembly 33

Figure 3-17: Meshed Lambertian target front view (a) and back view (b) 34
Figure 3-18: Detailed section of the meshed Lambertian target cooling channels with prism layers 36
Figure 3-19: Residuals monitor for the conjugate heat transfer analysis indicating convergence 37
Figure 3-20: Average fluid outlet and heat transfer coefficient plots as a function of solver iteration number 37
Figure 3-21: Wall temperature distribution of the water-cooled Lambertian target fluid domain 38
Figure 3-22: Temperature distribution on the front face of the Lambertian target 38
Figure 3-23: Schematic of the plasma-spraying process 39
Figure 3-24: Assembled water-cooled Lambertian target back view (a) and front view (b) . 40
Figure 3-25: Assembled target positioning system (TPS) at the SERAFF site 41
Figure 3-26: TPS motor control circuitry 42
Figure 4-1: CMOS Image sensor signal digitalisation and grayscale image display 45
Figure 4-2: Lambertian target illuminated by direct sunlight 46
Figure 4-3: Measured pixel values vs exposure indicating the logarithmic and linear photo response of the CMOS image sensor 47
Figure 4-4: Indirect spatial flux mapping system setup 48
Figure 4-5: Allowable grayscale intensity measurement range for the Canon EOS 1200D CMOS camera 49
Figure 4-6: Schematic of the focal plane optimisation procedure 50
Figure 4-7: Qualitative comparison of the radiative energy distribution intercepted by the moving Lambertian target 51
Figure 4-8: Image sensor field of view at the focal plane 52
Figure 4-9: Image of the cropped spatial calibration circle used for pixel scaling 53
Figure 4-10: Image thresholding operation for an 8-bit grayscale image 54
Figure 4-11: Binary image of the spatial correction circle in pixel co-ordinates and the associated physical dimensions that each pixel detects 54
Figure 4-12: Schematic diagram of a circular-foil Gardon gauge heat flux sensor 55
Figure 4-13: Total directional reflectivity vs angle of incidence for pyrolytic graphite and amorphous carbon materials 56
Figure 4-14: TG1000-1 water-cooled circular-foil Gardon gauge manufactured by Vatell Corporation™ 57
Figure 4-15: Side view of the Gardon gauge mounting fixture (a) and front view (b) 58
Figure 4-16: Manually defined rectangular ROI of the Gardon gauge sensor region (a) and the extracted ROI displayed in LabVIEW (b) 59

Figure 4-17: Gardon gauge influencing region defined in pixel co-ordinates 60
Figure 4-18: Error encountered by the Gardon gauge sensor approximation method (a) and error reduction by including the half-pixel intensity at the corners of the circular area approximation 60
Figure 4-19: Relationship between the radiative solar flux measured by the Gardon gauge and the corresponding pixel grayscale intensity obtained experimentally..... 61
Figure 5-1: Conversion from grayscale intensity image to calibrated spatial solar flux map 64
Figure 5-2: 9 m^2 non-focusing heliostat (a) and the 3 m diameter parabolic dish with the spatial flux measurement components (b) 65
Figure 5-3: Measured spatial flux maps acquired at (a) 9:00 am (b) 10:00 am (c), 11:00 am (d), 12:00 pm (e), 13:00 pm (f), 14:00 pm and (g) 15:00 pm over a square region of 276 mm x 276 mm on 24 October 2018..... 67
Figure 5-4: One-dimensional plot of the spatial x and y coordinates and their corresponding intensity for the spatial flux data acquired at 12:00 pm 69
Figure 5-5: Grayscale image conversion to a masked grayscale image with a user defined diameter..... 70
Figure 5-6: Cumulative thermal power vs target diameter for the measured spatial flux distribution obtained at 12:00 pm 71
Figure 5-7: CAD model of the SERAFF parabolic concentrator..... 71
Figure 5-8: Comparison of the measured solar flux distribution at 12:00 pm on 24 October 2018 to normalised simulated results obtained for varying slope and specularity standard deviation errors 72
Figure A-1: Spatial flux results (a) and 2-dimensional solar flux intensity curve (b) for the winter solstice ray-tracing simulations……85
Figure A-2: Spatial flux results (a) and one-dimensional solar flux intensity curve (b) for the summer solstice ray-tracing simulations..... 85
Figure B-1: Water-cooled Lambertian target isometric drawing……86
Figure B-2: Water-cooled Lambertian target assembly drawing..... 87
Figure C-1: Target positioning system linear actuator control panel within the SERAFF LabVIEW control software……..88
Figure D-1: 100-pixel square region of the Lambertian target for the Canon EOS 1200D photo response characterisation experiment (images ‘a’ to ‘t’ are shown)……89
Figure D-2: 100-pixel square region of the Lambertian target for the Canon EOS 1200D photo response characterisation experiment (images ‘u’ and ‘v’ are shown) 90
Figure E-1: Region of interest (ROI) control panel within the SERAFF LabVIEW control software……..91

Figure F-1: Calibration certificate for the TG1000-1 circular-foil Gardon gauge purchased from Vatell Corporation™……...93
Figure F-2: Linear regression calibration curve of the TG1000-1 circular-foil Gardon gauge purchased from Vatell Corporation™..... 94
Figure G-1: One-dimensional x-y intensity plots for the spatial flux measurements obtained at (a) 9:00 am, (b) 10:00 am, (c) 11:00 am, (d) 12:00 pm, (e) 13:00 pm, (f) 14:00 pm……..95
Figure G-2: One-dimensional x-y intensity plots for the spatial flux measurement obtained at 15:00 pm 96

LIST OF TABLES

Table 1-1: List of developed solar furnace facilities 3
Table 1-2: Solar furnace facilities that utilise indirect solar flux mapping methods 6
Table 1-3: List of requirements to meet the design specifications for a high concentration spatial flux mapping system 6
Table 1-4: Evaluation of various solar flux mapping techniques. Primary requirements are scored from 1 - 5, secondary requirements are scored from 1-3 7
Table 2-1: Sun angle and intensity for the winter and summer solstice days 14
Table 3-1: Optical measurement device used by conventional CSP systems for solar flux characterisation 21
Table 3-2: Material and mesh properties of aluminium Lambertian target model 30
Table 3-3: Lambertian target boundary condition specifications 33
Table 3-4: Mesh details for the water-cooled Lambertian target 34
Table 4-1: Canon EOS 1200D CMOS camera specifications 44
Table 4-2: Maximum recorded grayscale intensity for the acquired images 51
Table 5-1: Performance metrics for the spatial flux data measured at 12:00 pm 70
Table 5-2: Pixel measurement error for STIMS 74
Table D-1: Results for the images recorded by the Canon EOS 1200D CMOS camera for the phot response characterisation experiment 90

NOMENCLATURE

Symbol	Description	Unit
A_H	Heliostat surface area	m^2
A_I	Camera iris area	m^2
A_T	Projected area	m^2
c	Speed of light	m/s
E_{pixel}	Pixel irradiance	W/m^2
E_s	Surface irradiance	W/m^2
f	Focal length	m
F_s	Spectral correction factor	-
GV	Grayscale intensity	-
h	Planck's constant	J.s
I	Radiant intensity	W/sr
$\dot{m}$	Mass flow rate	kg/s
OD	Optical density	-
P	Wetted perimeter	m
px	Pixel length	m
$\bar{q}$	Average flux density	W/m^2
q_{DNI}	Direct normal irradiance	W/m^2
Q_{tot}	Total thermal power	W
QE	Quantum efficiency	%
Re	Reynolds number	-
T	Transmittance	%
T_s	Stagnation temperature	°C
t_{exp}	Exposure time	s
u_*	Near-wall velocity	m/s
y	Boundary layer thickness	m
y^+	Wall treatment constant	-
α	Absorptivity	-
α_z	Elevation angle	degrees
$\delta\Omega$	Camera iris solid angle	degrees
η_{opt}	Optical efficiency	-
θ_r	Polar angle	degrees
θ_z	Zenith angle	degrees

λ	Wavelength	nm
μ	Dynamic viscosity	Pas
μ_e	Free carrier electrons	e-
μ_p	Photon count	e-
ρ	Diffuse reflectivity	-
σ_B	Steffen Boltzmann constant	W/m^2K^4
σ_{slope}	Slope error	mrad
σ_{spec}	Specularity error	mrad
ν	Kinematic viscosity	m^2/s
φ	Azimuth angle	degrees
Φ_{gauge}	Gardon gauge measurement	W/m^2
Φ_{GV}	Averaged grayscale intensity factor	-

ACRONYMS

AM	Airmass
APS	Active pixel sensor
BDRF	Bidirectional reflectance distribution function
CCD	Charged-coupled device
CFD	Computational fluid dynamics
CMOS	Complementary metal-oxide-semiconductor
CSP	Concentrating solar power
CSR	Circumsolar ratio
DNI	Direct normal irradiance
DLR	Deutsches Zentrum für Luft- und Raumfahrt
DSLR	Digital single-lens reflex
EOS	Electro-optical system
FWC	Full-well capacity
GSET	Group for Solar Energy Thermodynamics
GUI	Graphical user interface
ITL	Interline transfer lag
KIER	Korea Institute of Energy Research
NIST	National Institute of Standards and Technology
NREL	National Renewable Energy Laboratory
PPD	Pinned photodiode
PSA	Plataforma Solar de Almería

PWM	Pulse width modulation
RANS	Reynolds-Averaged Navier stokes
SERAFF	Solar Energy Research Amplified Flux Facility
ROI	Region of interest
STIMS	SERAFF target irradiance mapping system
SAURAN	South African Universities Radiometric Network
TPS	Target-positioning system

Chapter 1 Introduction

1.1 Solar furnace operating principles

Solar energy has become a promising alternative to conventional methods of producing fuels and electricity that utilise a diminishing supply of fossil fuels and other natural resources. Concentrating solar energy systems have attracted a lot of attention for a variety of high temperature materials testing and thermochemical processes. Concentrating solar energy systems utilise lenses or specular reflective materials to collect and redirect the direct normal irradiance (DNI) to a focal point, where the concentrated solar flux heats up a receiver that intercepts the rays. Some high temperature materials processes include thermal surface treatments (Masuri et al., 1992), synthesis of corrosion resistant coatings (Sierra & Vázquez, 2006), and ceramic material sintering (Oliveira et al., 2005). In the field of solar thermochemistry, topics that have been investigated include solar waste processing and detoxification (Funken et al., 1999) and solar fuels production (Meier & Sattler, 2009). These processes typically require an intense level of thermal energy, demanding temperatures greater than 750 ºC and average radiative fluxes above 100 kW/m^2 (Levêque et al., 2017).

To attain the high thermal energy input required to drive these processes, a solar furnace configuration is typically utilised. A solar furnace is an optical system that collects the direct beam component of sunlight in a controlled manner and concentrates it onto a target. A solar furnace typically comprises a paraboloidal dish and receiver stand mounted in a fixed orientation within a housing structure. An external heliostat is used to redirect the solar radiation at a fixed angle to the paraboloidal dish. The elevation and azimuthal angle of the heliostat is constantly adjusted to maintain this fixed angle as the sun transits across the sky. The paraboloidal dish concentrates solar radiation to a focal point, the characteristics of which are dependent on the geometry of the dish. Solar furnaces typically generate average solar fluxes between 1 MW/m^2 and 6 MW/m^2, distributed across a focal spot with diameters ranging from 2 cm to 12 cm (Baldry & Taylor, 2016; Duncan et al., 2016). Objects that intercept the concentrated solar radiation can reach elevated as high as 3500 ºC (Haueter et al., 1999). The basic operation of a solar furnace system is illustrated in Figure 1-1.

The thermal energy output of a solar furnace is directly related to the and quality of the optical components. Poor reflective surface quality and surface warpage are major characteristics that influence the overall performance of solar furnace systems. These characteristics are greatly influenced by the quality of the optical materials and manufacturing procedures used for the fabrication of the optical components. However, high quality reflective materials and advanced manufacturing practices are often expensive to obtain in practice.

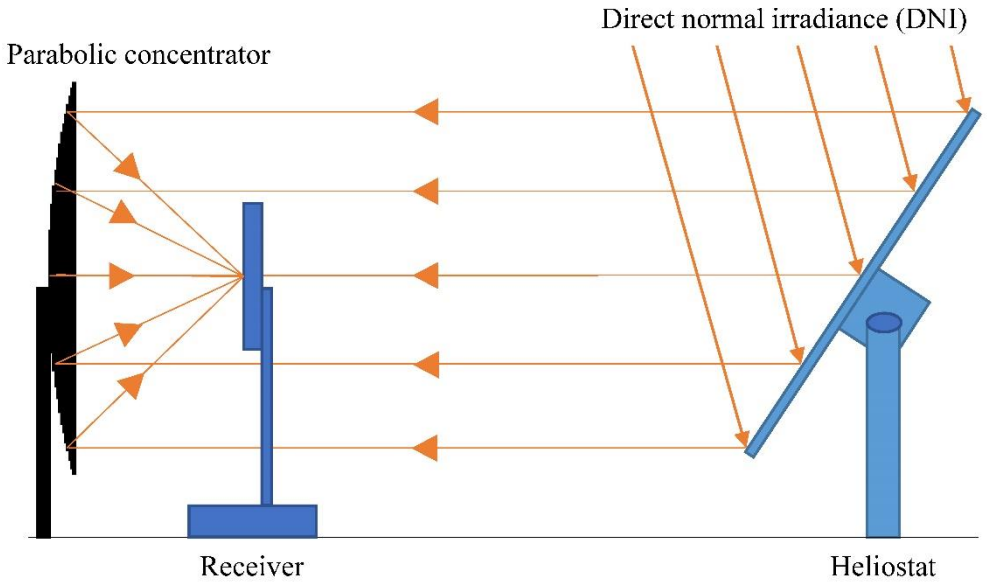

Figure 1-1: Solar furnace operation schematic

1.1.1 Solar Energy Research Amplified Flux Facility (SERAFF)

To aid advancements in concentrating solar power (CSP) technology, solar thermochemistry and high temperature materials testing within South Africa, the Group for Solar Energy Thermodynamics located at the University of KwaZulu-Natal, initiated the Solar Energy Research Amplified Flux Facility solar furnace project at the start of 2014 (Perumall et al., 2015; van Bakel et al., 2016). The facility, currently under development, is the first of its kind in South Africa and comprises a 9 m^2 non-focusing heliostat and a 3 m diameter paraboloidal dish concentrator (Figure 1-2).

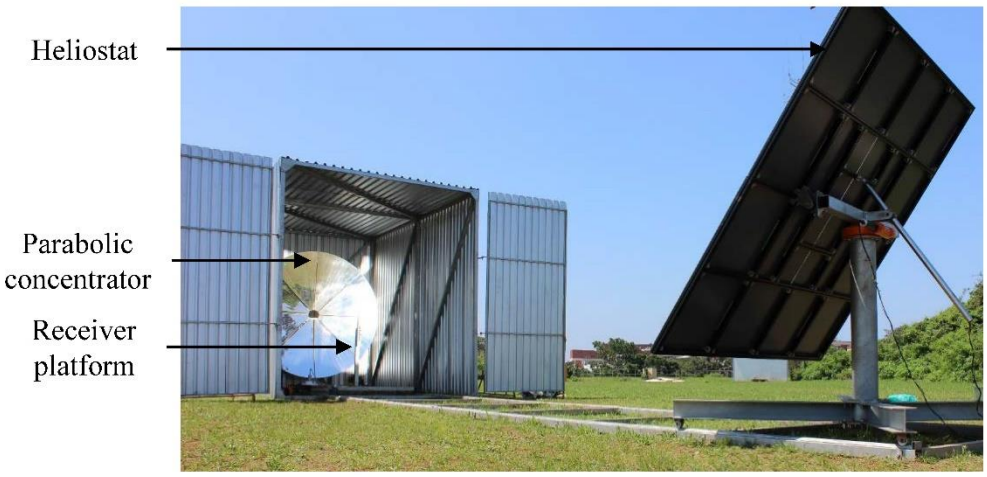

Figure 1-2: SERAFF solar furnace system components

There are several established solar furnace facilities that are used for a variety of high temperature applications. Table 1-1 lists a few well established solar furnace facilities and their respective performance parameters.

Table 1-1: List of developed solar furnace facilities

Facility Name	Application	Thermal Power (kW)	Peak thermal flux (kW/m^2)
PSA SF-5 (Rodríguez et al., 2014)	- Materials treatment	5	6000
Valparaiso University (Duncan et al., 2016)	- Solar thermal reactors - Materials testing	10	3000
DLR (Neumann & Groer, 1996)	- Solar chemistry - Materials testing - Receiver development	20	4000
KIER (Cho et al., 2014)	- Solar thermochemistry	45	5050
PSA SF-60 (Fernández-Reche et al., 2006)	- Thermochemical processing - PV cell testing	60	3000

Thermal power levels range from approximately 5 kW for lower-end solar furnace systems to as high as 60 kW. The optical components of the SERAFF solar furnace were designed to provide a peak thermal power output of 5 kW with an associative peak solar flux of approximately 2.1 MW/m^2 (Perumall et al., 2016).

1.1.2 Solar flux characterisation techniques

Accurate characterisation of a solar furnace's distributed energy output provides essential information about the optical system's concentrated radiative energy output and concentration accuracy. Moreover, the intensity of concentrated solar radiation incident on prototype receivers or reactors must be quantified to enable assessment of their performance. Knowledge of a solar furnace's concentrated solar flux distribution provides a foundation for other essential optical performance parameters to be calculated. These include maximum and average concentration ratios, which is the ratio of maximum and average solar flux to the direct normal irradiance (DNI) received by the heliostat, total thermal power output, blackbody stagnation temperature and optical efficiency (Lee et al., 2014).

Methods for quantifying spatial solar flux can be either direct or indirect. In a direct method, heat flux gauges are used that output a signal that is proportional to the radiative flux absorbed by the sensing element (Llorente et al., 2011; Wong & Chong, 2016). Sequential and simultaneous methods are incorporated to discretely measure the two-dimensional flux distribution at the measurement plane. In a sequential method, a single sensor is traversed

across the measurement plane at set intervals. The readings recorded at each interval are superimposed to generate a spatial representation of the flux in the measurement plane. Measurements with this configuration can take between 5 min and 10 min to map the focal region, depending on the response time and surface area of the sensor as well as the overall size of the focal region. Therefore, measurements obtained with this technique are sensitive to changes in DNI, prevailing atmospheric conditions and heliostat tracking errors that are present during the measurement period (Guillot et al., 2014).

Simultaneous methods utilise a series or array of heat flux gauges to record flux according to their position in the focal plane (Ballestrín & Monterreal, 2004). The sensors are moved simultaneously to different regions in focal plane, where their signal output relative to their position is recorded. Unlike sequential methods, the time required to measure each region in the focal plane is significantly reduced by introducing multiple heat flux gauges in series or parallel to map the focal region. An uncertainty in flux measurements reported in these cases is approximately ±3 % (Ballestrín et al., 2006). The resulting spatial resolution in both cases is, however limited to the size of the sensing area of the heat flux sensor.

Water calorimeters are also used to measure radiative solar flux. These devices provide a calorimetric measurement of the solar radiation absorbed by a black body absorber surrounded by flowing fluid, which is typically water. Heat transfer between the flowing fluid and absorber allows for the thermal energy transmitted to the flowing fluid to be calculated by measuring the temperature of the fluid before and after contact with the black body absorber and the mass flow rate of the fluid (Mouzouris et al., 2002). The accuracy of the mass flow rate and temperature sensors as well as the design of the black body absorber impact the overall performance of these devices. The absorptivity of the sensor surface depends on the absorption co-efficient of the coating applied to the surface and spectral composition of the incoming solar radiation. The thermal energy balance of the device also depends on the convective and radiative energy exchange to the surrounding environment. Response times can vary from a few seconds to approximately 2 min, depending on the size of the sensor surface and the flow rate of the heat transfer fluid (Guillot et al., 2014).

Indirect spatial flux mapping systems use principles of photometry and radiometry to quantify the spatial distribution of radiative solar flux reflected off a Lambertian diffuse surface. The reflected light distribution is measured by a charge-coupled device (CCD) or complementary metal-oxide semiconductor (CMOS) camera (Röger et al., 2014). The non-dimensional grayscale intensity recorded by the digital camera is calibrated by directly measuring the radiative flux at the measurement plane using a heat flux gauge (Röger et al., 2011). These

measurement principles have been applied using different techniques to measure spatial solar flux.

One method is to use a small Lambertian strip that moves across the focal spot region, while a camera captures multiple images of the strip as it traverses the focal region. The area of the moving bar is cropped in each image and combined to generate a representation of the spatial solar flux of the focal region (Lüpfert et al., 2000). The combined image is calibrated according to a reference measurement obtained by a heat flux gauge. Measurements using this method can take up to several minutes depending on the size of the moving target, the size of the focal region and speed of the traversing mechanism.

Another method is to position a Lambertian target, with dimensions slightly larger than the estimated focal spot size, at the focal region. The solar radiation that intercepts the target is measured instantly, without the need to combine images or incorporate a traversing mechanism. Commercially available absorptive neutral density filters are mounted onto the camera lens to attenuate the intensity of light that reaches the camera image sensor to prevent pixel saturation and damage. This makes it possible to integrate this technique into systems that generate high intensity radiative flux.

The high spatial resolution of image sensors and fast response time of the camera's shutter mechanism allows the radiative flux at all locations in the measurement plane be measured accurately and quickly. Additionally, only one heat flux sensor is required for calibration purposes. The approximate measurement uncertainty of solar flux using an indirect method ranges from -4.7% to +4.1% (Ulmer et al., 2002) . This uncertainty depends on the system setup and the measuring equipment used as other cases report measurement uncertainties of about ±6% (Strachan & Houser, 1993). These systems also identify the heat flux gauge used for calibration accounts for ±3% of the overall measurement uncertainty in each case.

An alternative to using a heat flux gauge to calibrate the brightness images recorded by the digital camera is to record an image of the sun (Ho & Khalsa, 2012). In this method, a brightness image of the sun, captured by a digital CCD or CMOS camera, is compared to a DNI reading. The sun image serves two purposes in this method. Firstly, they provide an irradiance reference as the measured pixel intensities within the sun influencing region are comparable to the reference DNI reading, allowing the pixel values to be scaled to represent power (in watts). Secondly, they provide a spatial reference to determine the meters-per-pixel conversion factor. A major drawback to this method is that the reflectivity of the receiver must be quantified to obtain accurate measurements.

In general, indirect flux mapping techniques using either a moving strip or stationary target are commonly used for spatial solar flux characterisation. These methods offer good response

times, high spatial resolution and low measurement uncertainties (Röger et al., 2014). Table 1-2 lists solar furnace systems that utilise an indirect flux mapping method.

Table 1-2: Solar furnace facilities that utilise indirect solar flux mapping methods

Solar furnace facility	Thermal power output (kW)	Peak flux (kW/m^2)
Platforma Solar de Almeria (Ulmer et al., 2002)	50	1640
KIER (Lee et al., 2014)	40	5050
DLR (Neumann & Groer, 1996)	20	4000
SFL (Baldry & Taylor, 2016)	6.4	1000

1.1.3 Assessment of solar flux characterisation techniques

A set of criteria was established to select the best method for characterising SERAFF's concentrated spatial solar flux distribution. These requirements were split into primary and secondary sub-categories. In this analysis, the primary requirements carry greater weighting than the secondary requirements. Table 1-3 shows the selection criteria that were considered in this analysis.

Table 1-3: List of requirements to meet the design specifications for a high concentration spatial flux mapping system

No.	Primary requirements	Secondary requirements
1	Measure solar flux	High repeatability
2	Low response time	Low susceptibility to environment
3	High spatial resolution	Low cost
4	Good temperature stability	Low complexity
5	Low measurement uncertainty	

Each direct and indirect method was evaluated under the selection criteria provided in Table 1-3. Primary and secondary factors were weighted differently, with primary factors being scored out of a maximum of 5 (1 being undesirable and 5 being desirable) and secondary factors scored out of 3. Each factor was evaluated within the context of high concentration spatial solar flux measurements and not in terms of general performance. The decision matrix is given in Table 1-4.

Direct methods offer low measurement uncertainty, good response times and temperature stability, but scored low in terms of scalability, complexity and spatial resolution. Indirect methods have considerably higher measurement uncertainties due to errors with the digital camera and reflective properties of the Lambertian target. However, these systems offer superior response times, high spatial resolutions, high repeatability and low complexity. The

total scores provided in Table 1-4 indicated that an indirect flux mapping system would be best suited to characterise SERAFF's spatial solar flux distribution.

Table 1-4: Evaluation of various solar flux mapping techniques. Primary requirements are scored from 1 - 5, secondary requirements are scored from 1-3

	Primary requirements					Secondary requirements				
Direct methods	**1**	**2**	**3**	**4**	**5**	**1**	**2**	**3**	**4**	**Total**
Sequential	5	3	2	3	4	3	2	2	1	**27**
Simultaneous	5	3	2	3	4	3	2	2	1	**28**
Water calorimeters	5	2	1	1	2	3	3	2	3	**26**
Indirect methods										
Moving stripe target	5	5	4	3	3	3	2	2	1	**31**
Stationary target	5	5	4	4	3	3	2	2	3	**36**
Sun calibration	5	5	4	4	2	3	2	2	2	**33**

With regards to using a moving stripe target and sequential method, the mechanical traversing mechanism needs to be synchronised with the camera shutter mechanism to ensure that all regions within the focal plane are measured, making these systems rather complex. These systems scored low in terms of response time (primary requirement 2) as the stripe or sensor would have to move across the entire focal plane to acquire a measurement. Mechanical moving parts are also susceptible to environmental conditions, including humidity and thermal loads that are present when measurements are being made and would require constant maintenance to maintain good repeatability.

High spatial resolution (primary requirement 3) is an important requirement for spatial flux characterisation to ensure that solar flux gradients distributed across the focal spot are accurately captured. Direct methods use heat flux sensors, the resolution of which is dependent on the size of the sensing element, whereas indirect methods use high resolution cameras to capture the flux profile.

Objects that intercept the focal spot of a solar furnace can reach exceedingly high temperatures (up to approximately 3500 ℃) requiring that the measurement system must be stable at high temperature (primary requirement 4). Heat flux sensors and Lambertian targets can be stabilised at high temperatures by passing a cooling fluid through the device during use.

Neutral density filters can be equipped to cameras to prevent damage to the image sensors when capturing an image of the concentrated solar radiation.

The indirect systems listed (besides the sun calibration method) require a heat flux gauge to calibrate the camera. Since these heat flux sensors measure the solar flux directly, the uncertainty of the measurement lies with the sensor alone. For this reason, direct methods offer lower measurement uncertainties (primary requirement 5) compared to indirect systems that require a camera and diffuse reflective target, which adds to the overall system measurement uncertainty.

Designing a stationary Lambertian target that covers the focal plane region instead of using a moving bar significantly reduces the complexity of the system. The sun calibration method eliminates the need to have additional sensors to calibrate the digital camera, which reduces overall system cost (secondary requirement 3). Measurement uncertainties with this method were reported to be high and required additional equipment to characterise the Lambertian target reflectivity (Ho & Khalsa, 2012).

Each method was assessed and scored according to the aforementioned factors. Systems that use a direct method offered very good response times and stability at high temperatures, but severely lacked high spatial resolution. Indirect methods surpassed direct methods in terms of high spatial resolution and response time but fell short in terms of measurement uncertainty. Based on this assessment, it was decided to develop the SERAFF target irradiance mapping system (STIMS), incorporating a digital camera, stationary Lambertian target and heat flux gauge.

1.2 Research objectives

The primary objective of this work is to design and fabricate a high concentration solar flux mapping system, in order to characterise the spatial solar flux distribution at the focal plane of the SERAFF solar furnace. To achieve this, an indirect spatial flux characterisation method is to be utilised, which requires a digital camera, Lambertian diffuse target and a heat flux gauge for calibration. The study had the following research objectives:

1. Investigate solar flux mapping technologies and select the appropriate technology for the SERAFF solar furnace.
2. Generate theoretical performance models of the SERAFF solar furnace through Monte Carlo ray-tracing simulations.
3. Design the components used for the indirect flux mapping method to be used within SERAFF that meet both financial and practical constraints.

4. Fabricate and install the indirect flux mapping system at the SERAFF solar furnace with consideration that other facility operations are not impeded.
5. Development of image processing procedures and an autonomous control algorithm for the indirect flux mapping method.
6. Design a software user-interface to enable on-demand data acquisition processes related to the indirect flux mapping system. Optical system calibration, graphical display of 2-dimensional spatial solar flux data and other key performance parameters are to be displayed in the user-interface.

1.3 Methodology

To satisfy the above research objectives, the following activities were undertaken:

1. Perform an assessment of solar flux mapping techniques and formulate a set of selection criteria to select the appropriate technique for this application.
2. Idealised optical performance modelling of SERAFF's existing heliostat and primary concentrator to evaluate the expected performance range of the facility throughout the year using the Monte-Carlo ray-tracing programme Tonatiuh^{TM}.
3. Investigation of the principles of photometry and radiometry and review of existing indirect spatial flux mapping systems within the context of high concentration solar flux characterisation.
4. Conceptual design formulation of a water-cooled Lambertian diffuse-reflective target using peak estimated spatial flux data obtained from the Tonatiuh^{TM} ray-tracing simulations.
5. Validate water-cooled Lambertian target design with a conjugate heat transfer simulation.
6. Design of a target-positioning system to enable effective use of the Lambertian target within the focal plane of the SERAFF solar furnace by overcoming various spatial constraints.
7. Characterise the photo-response curve of the CMOS camera used to acquire spatial solar flux measurements to determine its effective measurement range.
8. Fabrication, assembly, calibration and testing of the indirect flux mapping system components at the SERAFF solar furnace.
9. Comparison of a CMOS camera's grayscale intensity output to reference measurements of solar flux acquired with a Gardon gauge heat flux sensor.
10. Acquire performance parameters of SERAFF in its current form through experimentation.

1.4 Thesis outline

Chapter 2 describes the idealised performance modelling of the SERAFF solar furnace through Monte Carlo ray-tracing simulations using Tonatiuh^{TM}. The chapter outlines benchmark performance parameters of the SERAFF solar furnace during the winter and summer solstice days respectively.

Chapter 3 outlines the relevant digital camera characteristics for spatial solar flux measurements. A detailed design methodology for the indirect flux mapping system is described with respect to mechanical and optical aspects. This includes the selection of the optical measurement device, heat transfer analysis of the Lambertian target, mechanical design of a target positioning system and selection of the heat flux sensor for calibration.

Chapter 4 describes a method for determining the linearity curve for a digital CMOS camera. The camera pixel intensity calibration method is discussed.

Chapter 5 discusses the spatial flux measurement methodology and provides performance parameters of the SERAFF solar furnace.

Chapter 6 highlights the key findings of the research and concludes the study.

Chapter 2 SERAFF optical performance modelling

2.1 Monte Carlo ray-tracing analysis

Knowledge of SERAFF's expected thermal power output, concentrated solar flux output and focal spot size was essential to the design of the indirect flux mapping system. These parameters were estimated using ray-tracing methods and provide an indication of the effective measurement range and spatial constraints at the focal plane of the solar furnace. Ray-tracing procedures are widely used in optical system design. This method involves the stochastic trajectory of several rays that intersect with the optical surfaces with each ray carrying the same amount of energy. The reflected direction of each ray is determined by the Fresnel optics rule and the power density of each ray is dependent on the reflective, absorptive and emissive properties of the optical surfaces. Using this approach, it was possible to calculate the expected flux distribution developed by the optical system. SERAFF performance simulations were performed using Tonatiuh™, which is an open-source Monte Carlo ray-tracing programme developed to aid in the design of CSP systems (Blanco et al., 2011).

In the context of solar flux characterisation, the maximum magnitude of solar flux generated by the SERAFF solar furnace must be estimated so that an appropriate heat flux gauge and digital camera can be selected. However, due to the temporal variation of the solar resource, a ray-tracing analysis would have to be executed for each day of the year to determine the maximum thermal power output and solar flux generated by the SERAFF facility. This would prove to be a tedious and time-consuming task and was avoided by limiting the analysis to the winter solstice and summer solstice days only. A solstice occurs when the equatorial plane is tilted relative to the Earth-sun line at the most positive and most negative declination angle (Stine & Harrigan, 1985). In the Southern hemisphere, the winter solstice occurs when the sun is the furthest away from the earth at the most positive declination angle and most negative during the summer solstice. Consequently, lower DNI and fewer daylight hours can be expected during the winter solstice when compared to the summer solstice. Thus, using these cases allows for a conservative determination of the theoretical performance range of the SERAFF facility throughout the year.

2.2 SERAFF ray-tracing model

An idealised ray-tracing model was established using existing geometry profile data developed previously by GSET (Perumall, 2016). Figure 2-1 illustrates the setup and procedure of running the SERAFF idealised performance ray-tracing simulations within Tonatiuh™.

The pre-processing phase involved recreating the SERAFF optical components within the Tonatiuh™ environment. Parametric shape functions tools were used to generate the heliostat

and parabolic concentrator geometries by defining their dimensions. Geometric and material specifications were defined to replicate SERAFF's existing optical components. The heliostat glass mirror reflective surface is 3 m x 3 m square with a reflectivity of 0.84 (Khan et al., 2016). The 3 m diameter parabolic concentrator dish was fabricated using ALANOD-MIRO™ aluminium sheets with a reflectivity of 95% (Cassim et al., 2015).

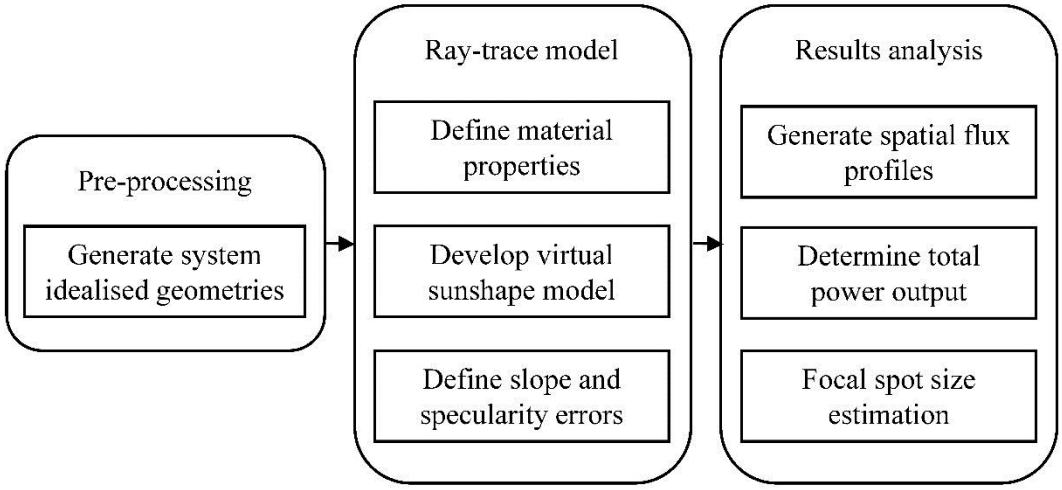

Figure 2-1: Ray-tracing simulation procedure diagram

To analyse the flux distribution at the focal plane, a virtual target was generated and positioned in front of the parabolic concentrator at a distance equal to the focal length of the dish (3 m). The virtual target was modelled as a perfect black body absorber with 100 % absorptivity.

2.2.1 Sunshape model

An important aspect of ray-tracing simulations is the suitable definition of a light source from which rays are generated. When considering CSP ray-tracing simulations, the solar flux distribution developed at the focal plane is influenced by the sunshape of the incident solar flux.

When collimated sunlight reaches the Earth, forward scattering occurs due to interactions with particulates within the Earth's atmosphere, broadening the overall distribution of the incident light and forming the solar aureole (Buie et al., 2003). Tonatiuh™ utilises a probabilistic grid source from which rays are stochastically generated. The sun's intensity distribution is defined by the Buie sunshape model, which also considers the energy contained within the circumsolar region of the sun's disc (Buie & Monger, 2004).

The radial energy distribution along the sun's disk and circumsolar region (solar aureole) influences the distribution of concentrated solar flux at the focal plane of the concentrating solar energy system. The intensity and distribution of the incident solar energy is altered by a variety of conditions associated with geographic location, climate, season and time of day. The

sunshape model used in Tonatiuh^{TM} is not influenced by geographic location when defined by the ratio of energy contained within the circumsolar region and total energy within the beam component, known as the circumsolar ratio (CSR). Generic sunshape models have been developed for CSRs between 0 % and 40 %. Based on a statistical analysis performed by Neumann et al. (2002), a sunshape model with a CSR of 5 % was the most frequently measured profile. To this end, the sunshape model used for the SERAFF ray-tracing simulations was generated using a CSR of 5 %.

2.2.2 Direct normal irradiance and observer-sun angles

The intensity of solar radiation contained within each generated ray was determined by specifying the time, date and location specific direct normal irradiance (DNI). The DNI data for the winter solstice (22 June) summer solstice (22 December) days was obtained from the Southern African Radiometric Network (SAURAN) (Brooks et al., 2015). The primary function of the heliostat is to direct the rays emanating from the sun to a defined fixed point. The sun's position relative to a point defined by latitude and longitude co-ordinates is described by the angle between central ray and the horizontal plane (α) or complement of the solar zenith angle (θ_z) and the angle measured clockwise from the north co-ordinate axis to the projection of the central ray (A) as shown in Figure 2-2.

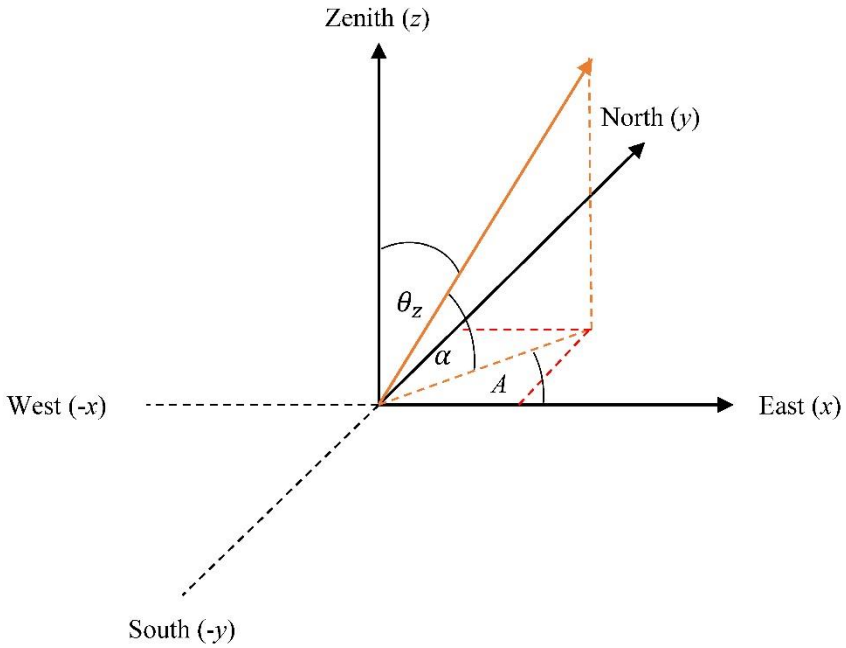

Figure 2-2: Coordinate system for describing azimuth and elevation angles in the southern hemisphere

For specular reflective surfaces, the angle of incidence is equal to the angle of reflection, requiring the heliostat to be tilted such that the reflected rays intersect a plane perpendicular

to the aimed surface normal. The sun's position relative to the SERAFF site location (Figure 2-3) was determined using the Solar Position Algorithm (NREL, 2003).

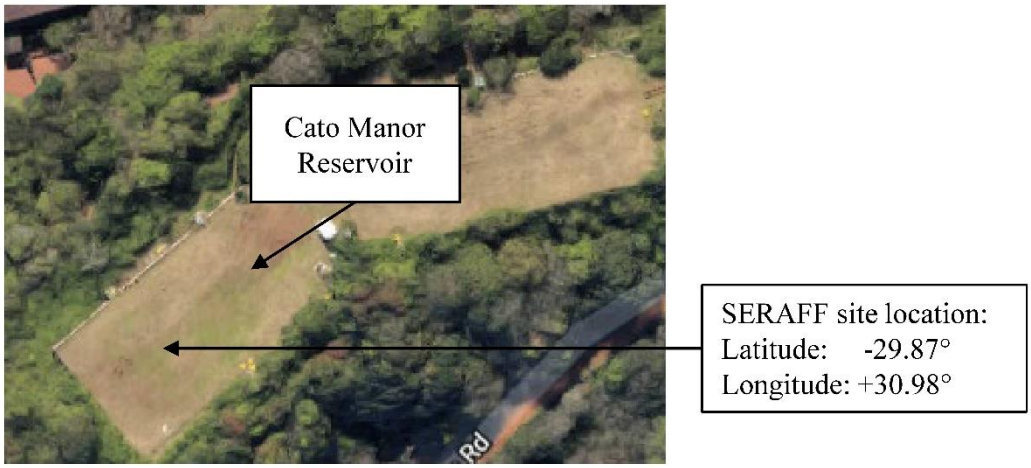

Figure 2-3: SERAFF site location on Cato Manor reservoir situated within Howard College

A summary of inputs used to generate the sun model for the winter and summer solstice days at solar noon is given in Table 2-1.

Table 2-1: Sun angle and intensity for the winter and summer solstice days

Specification	Winter solstice	Summer solstice
Date	22 June	22 December
Time	11:58 am	11:54 am
Solar elevation angle	36.7 º	83.6°
Solar azimuth angle	0°	0°
Direct normal irradiance	804 W/m^2	1026 W/m^2
Heliostat elevation angle	71.65°	48.2º
Heliostat azimuth angle	0º	0º

2.2.3 Optical errors

Curvature imperfections are generally encountered along the surfaces of practical reflectors, which cause reflected rays to deviate from their intended paths. The two primary forms of errors found in real-world optical systems are slope errors (macroscopic) and specularity errors (microscopic). These errors are random in nature and are represented by normal probability distribution (Osório et al., 2016; Bannerot, 1986). These errors are illustrated in Figure 2-4.

As a consequence of these errors and the sunray half angle, there is a misdirection of sunlight at the focal plane and a finite focal spot size. Instead of the light converging to an infinitesimally small focal point, the light spreads across a broad focal spot, with an energy distribution profile that is approximately Gaussian (Figure 2-5).

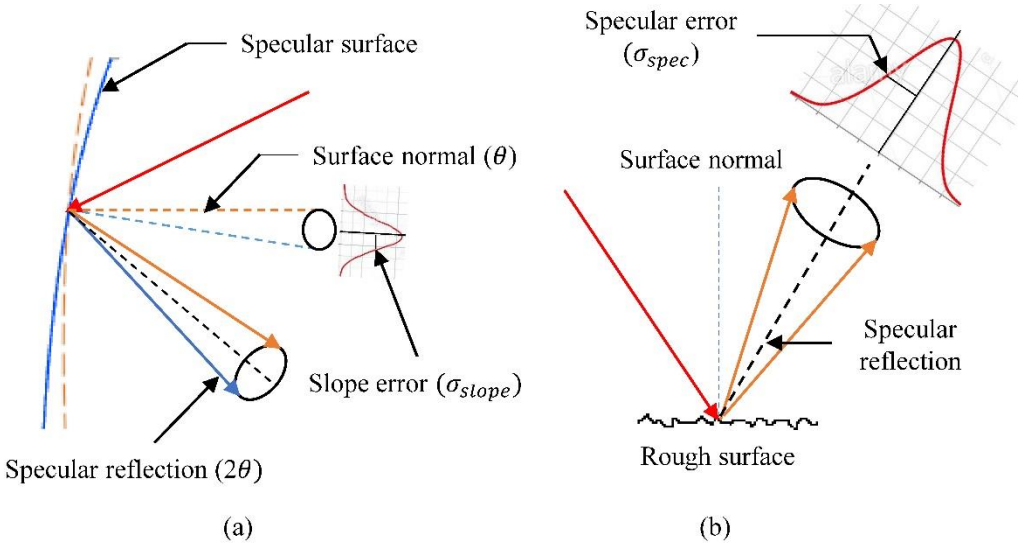

Figure 2-4: Illustration of surface slope error (a) and surface specularity error (b)

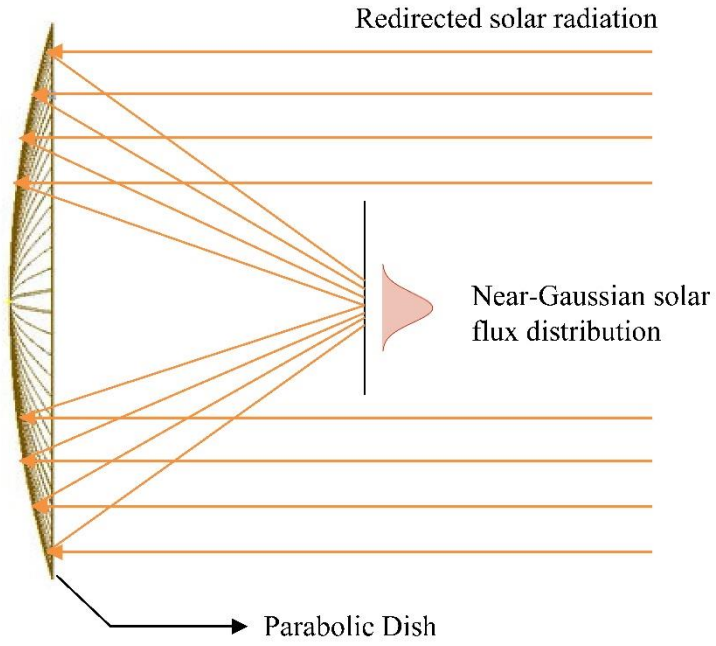

Figure 2-5: Theoretical Near-Gaussian solar flux intensity distribution at the focal plane of a parabolic dish concentrator

Slope and specularity errors were applied to the heliostat and parabolic concentrator in the ray-tracing environment. Since slope and specularity errors are typically probabilistic and difficult to measure, values were obtained from literature for use in this study. Heliostat slope errors are typically 1.5 mrad (SolarPACES, 2000), whereas slope errors for parabolic dish systems are typically 3 mrad (Meyen et al., 2010). Specularity errors are microscopic surface imperfections associated with the quality of the optical material. Typical specularity error values for heliostats and parabolic concentrators are 0.25 mrad and 3 mrad respectively

(Stine & Harrigan, 1985). A specularity error of 1.5 mrad was applied to both the heliostat and parabolic concentrator.

2.2.3 Ray-tracing results

The accuracy of a ray-tracing simulation is dependent on the number of ray-surface interactions. This solving method requires an iterative approach since it is difficult to predict how many rays the solver requires to reach convergence. In this study, a low number of rays were initially prescribed for Tonatiuh^{TM} to process. Additional rays were then added to successive solutions and simulation convergence was determined by monitoring the change in average flux on the receiver surface after each iteration. When only minor changes to the average flux value was observed, the simulation was deemed to have reached convergence. For these simulations, solver convergence was achieved after processing 75 000 000 rays. The spatial flux distribution for the summer and winter solstices are shown in Figure 2-6.

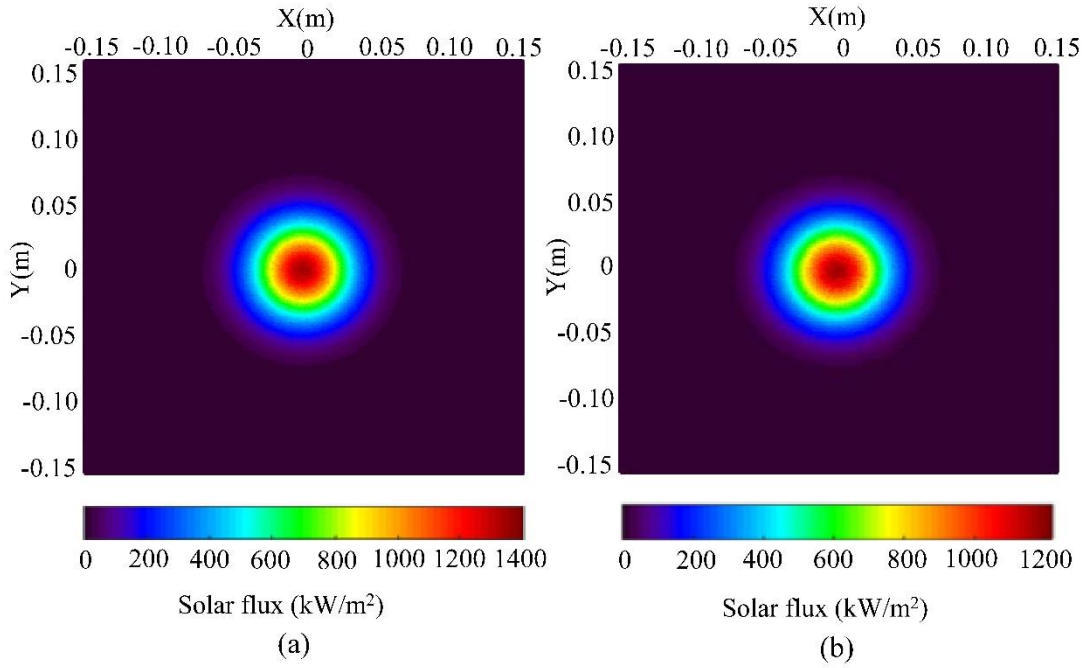

Figure 2-6: SERAFF spatial flux distribution at the focal plane for (a) the summer solstice (22 December) at 11:58 am and (b) the winter solstice (22 June) at 11:54 am

The total thermal power output was calculated to be 4.8 kW and 4.36 kW during the summer and winter solstice days respectively. This indicated a 9% decrease in thermal power output during the winter solstice compared to the summer solstice. The simulated annual variation peak concentrated solar flux generated by SERAFF ranges from 1.26 MW/m^2 to 1.4 MW/m^2. The flux is distributed across a focal spot that is approximately 180 mm in diameter. Two-dimensional plots of the spatial flux distributions are given in Appendix A.

These results provided a benchmark for designing the Lambertian target and selecting the digital camera for the indirect spatial flux mapping system, which is discussed in Chapters 3 and 4 respectively. Although the ray-tracing software considers the influence of slope and specularity errors on concentration accuracy, there are still other real-world factors that greatly hinder the performance of optical systems. These include heliostat tracking and receiver misalignment errors that are difficult to quantify and cannot easily be modelled in the ray-tracing environment. The purpose of this ray-tracing analysis was to provide a benchmark of SERAFF's thermal energy output in terms of thermal power output, focus size and maximum solar flux. These parameters were used to select an appropriate digital camera, design the Lambertian target and select a heat flux gauge.

Chapter 3 SERAFF target irradiance mapping system

3.1 Indirect flux characterisation

As previously discussed in Chapter 1, an indirect flux mapping technique was the preferred method to characterise SERAFF's spatial solar flux distribution. In this configuration, the concentrated solar flux is measured in two-dimensions by optically viewing the solar radiation reflected off a white diffuse-reflective Lambertian target with a digital camera. This type of system comprises three major components, which include a digital camera, Lambertian target and heat flux gauge for calibration. To design a reliable and robust spatial flux characterisation system for the SERAFF solar furnace that offered high measurement accuracy and repeatability, a research and design workflow procedure for the major components was established (Figure 3-1).

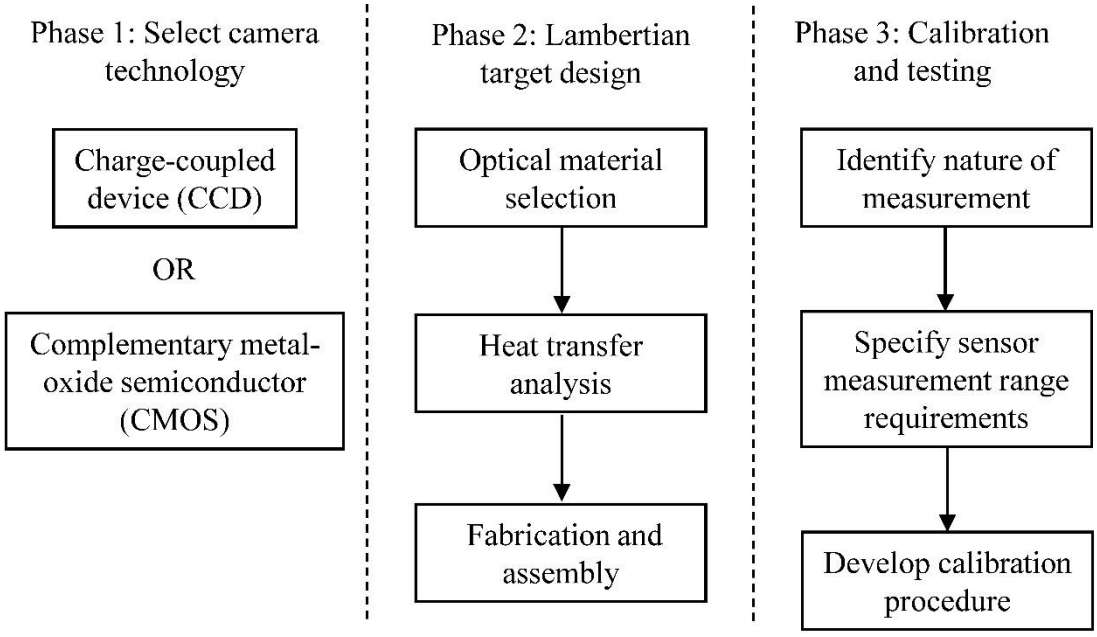

Figure 3-1: Indirect flux mapping system design workflow diagram

Each process was investigated in detail to meet the practical and financial constraints of the project and ensure successful integration with the SERAFF solar furnace.

3.2 Imaging sensors

Image sensors are photosensitive devices that convert incident light into an electrical signal that contains the intensity characteristics of the measured light. Digital image sensors are constructed from arrays of photosensitive semiconductor elements known as pixels. Each independent pixel measures the light intensity reflected off an illuminated surface in real space

(Taylor, 1998). The data captured at each pixel is digitised and processed as a two-dimensional array.

When designing an optical measurement device, the spectral composition of the radiative source must be considered. Solar furnace systems utilise the direct beam component of sunlight, which is light that travels along a straight path from the sun to the earth's surface. A large portion of irradiance falls within the visible bandgap of the solar spectrum between wavelengths of 360 nm to 830 nm with radiation above 800 nm falling into the infrared region (Figure 3-2). CCD and CMOS image sensors are sensitive to visible light and near infrared wavelengths of approximately 350 nm to 1050 nm (Darmont, 2009). Although image sensors cannot detect radiation across the entire solar spectrum, they are still suitable for capturing most of the energy contained within sunlight.

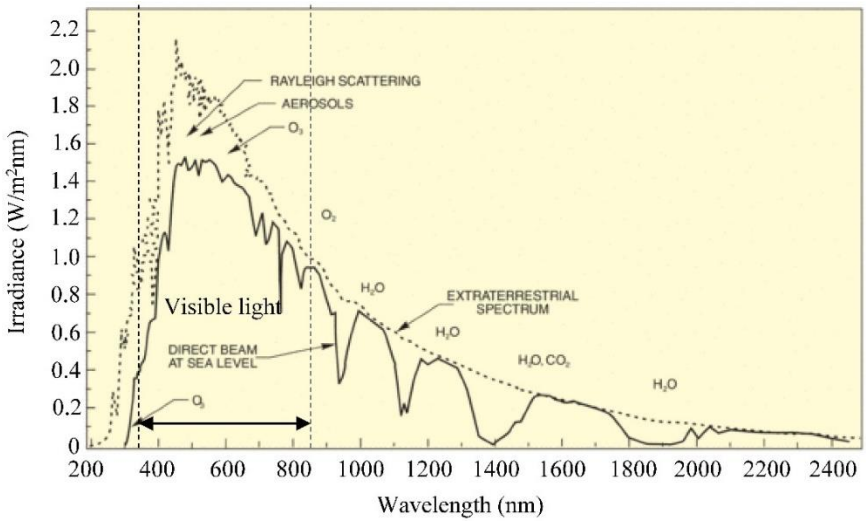

Figure 3-2: The effective spectral composition of sunlight at sea level for a clear-sky day. The dotted curve indicates the extraterrestrial spectrum (Iqbal, 1983)

The dominant photographic technologies on the market are CCD and CMOS image sensors. The major difference between them is the photon to charge readout methods. CCD image sensors generate images by sequentially transferring the electron-charge at each pixel to the readout amplifier. The advantage of sequential charge transfer is that there is no capacitance or resistance to degrade the signal since all the charge information is passed through a single output amplifier. This provides good image quality with minimum pixel noise. However, since all the pixels are coupled, blooming can occur where the charge collected at the pixels spills into adjacent pixels, affecting overall image quality and accuracy (Virto et al., 2002). Figure 3-3 illustrates the sequential charge transfer procedure for a CCD camera.

Unlike CCD image sensors, CMOS sensors have their signal processing and timing control circuitry integrated onto the sensor. Each photodiode pixel is directly connected to a charge

amplifier eliminating the need for sequential processing of the individual pixel data since the charge-to-voltage conversion is determined at each pixel simultaneously (Figure 3-4). Advances in CMOS image sensor technology offer improved image quality to that of CCD technology. This has been achieved by introducing the same pinned photodiode image sensor used for CCD imagers to CMOS fabrication processes. This change has significantly reduced cost, power consumption and readout noise of CMOS image sensors used in digital single-lens reflex (DSLR) cameras (Choubey et al., 2016). Another major advance was the development of the active pixel sensor (APS), which added additional circuity and amplifiers at each pixel of conventional CMOS image sensors to significantly reduce noise and improve image quality (Furth, 2015).

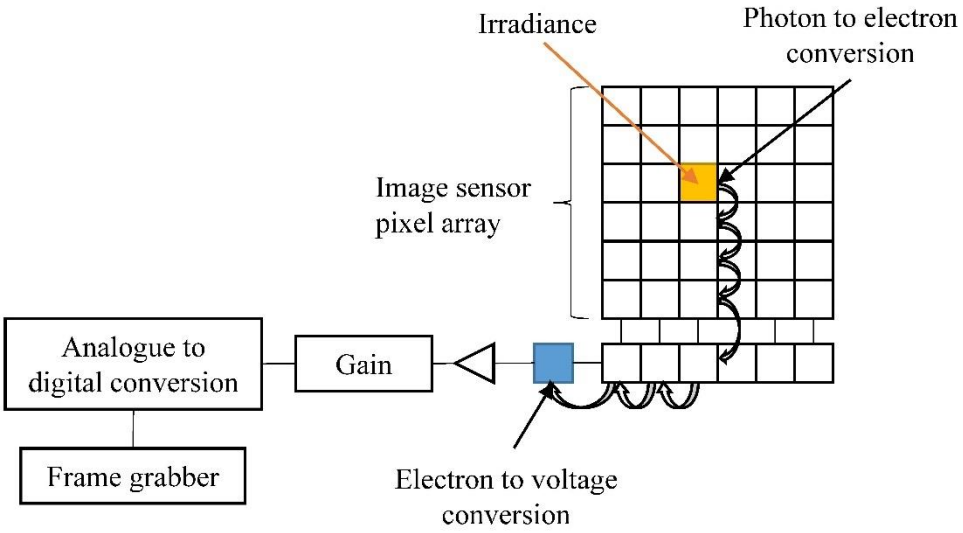

Figure 3-3: Sequential charge-coupled transfer method for a CCD camera

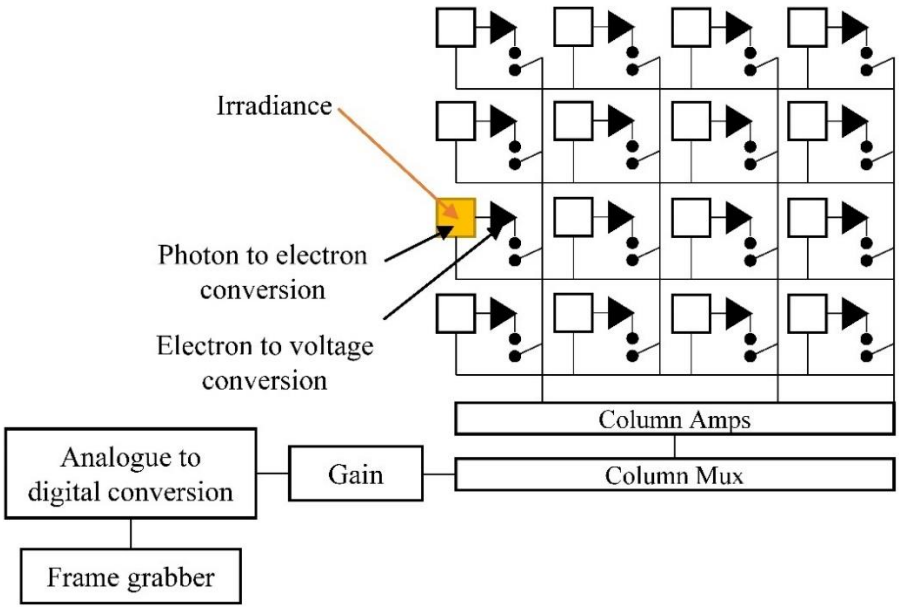

Figure 3-4: Simultaneous readout method of a CMOS camera

In this study, conventional indirect flux mapping systems used for solar flux characterisation were investigated to determine the feasibility of using a CCD or CMOS camera. The results are given in Table 3-1.

Table 3-1: Optical measurement device used by conventional solar furnace systems for solar flux characterisation

Concentrating solar energy system	Peak concentration ratio (suns)	Peak power output (kW)	Image sensor technology
University of New South Wales solar furnace (Baldry & Taylor, 2016)	1000	6.4	CMOS
KIER solar furnace (Lee et al., 2014)	5050	40	CCD
University of Stellenbosch (Bode et al., 2012)	0.635	-	CMOS
DLR solar furnace (A. Neumann & Groer, 1996)	4000	20.5	CCD

CCD cameras are more frequently used than CMOS cameras for solar flux characterisation systems due to their superior image sensor design (Röger et al., 2014). However, recent advances in CMOS image sensor design have placed them on par with CCD performance at a significantly lower cost (Choubey, 2016). For this work, a CMOS camera with an APS image sensor was used for the SERAFF indirect flux mapping system. Further details on the camera's specifications are discussed in Chapter 4.

3.3 Image sensor characteristics

The purpose of this research is to characterise radiative solar flux using an optical measurement device. It is therefore essential to understand image sensor characteristics in relation to pixel design and readout circuitry. As with most measurement systems hardware, there are imperfections in their design which limit their functionality. In digital photography, these imperfections are associated with the design of the pinned photodiode, quantum efficiency, dark current, full-well capacity and vignetting.

3.3.1 Pinned photodiode

A photodiode is a photosensitive device that generates an electrical signal based on the intensity of light that it absorbs. These devices operate on the principle of the photoelectric effect, namely that when a photon with sufficient energy (usually larger than the bandgap of silicon) strikes the photosensitive surface it will emit an electron in response to the incident light (Wheaton, 2009). A photodiode consists of *n*-type and *p*-type semiconductor materials, which are fused together to form a *pn*-junction. When photons are absorbed by the photodiode,

an electron-hole pair is created. As a result, the internal electric field within the depletion region sweeps free electrons to fill the holes within the p-type material (Figure 3-5). Consequently, the holes within the p-type material are swept to the n-type material (Jain, 2016).

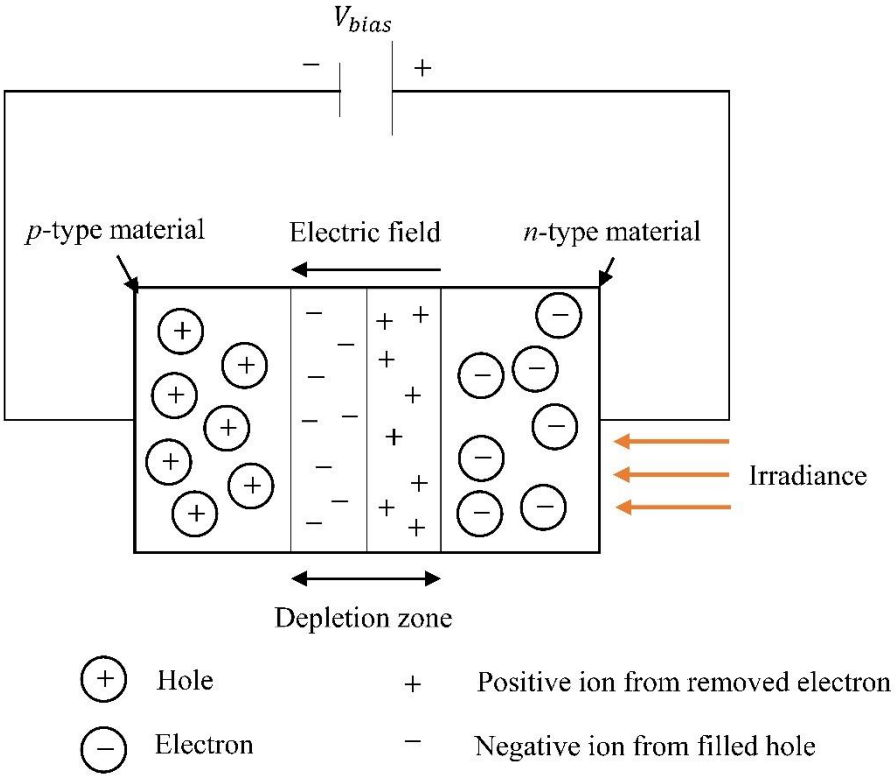

Figure 3-5: Photodiode photon excitation diagram

This diffusion of electrons and holes generates a photoelectric current that flows from the *n*-type to *p*-type material. When the *pn*-junctions are operated in reverse bias, the photoelectric current generated from the diffusion of electrons characterises the intensity of incident light absorbed by the photodiode (Xu, 2015). To resolve interline transfer lag (ITL) and capacitance reset noise associated with early photodiode devices, a p^+ layer was added to the *n*-type material of the original photodiode structure (Fossum et al., 2014). The new structure was named the pinned photodiode (PPD) and is fabricated into all modern CMOS and CCD image sensors due to its improved performance capabilities. Compared to the standard photodiode, the implementation of a heavily doped p^+ layer significantly reduces dark current, noise and increases quantum efficiency.

3.3.2 Dark current

In an ideal case, a photodiode should only generate a signal when illuminated. In reality, a small amount of signal is generated even in the absence of light. This small leakage of electrons is referred to as dark current and is a result of physical phenomena that occur in a PPD (Jain,

2016). For CMOS image sensors, this error is generally random since each PPD has its own readout circuitry. To account for this error, an image of the measuring plane is acquired in the absence of light before exposing the image sensor to the light source. The pixel data from the dark frame image is then subtracted from the light intensity image (Porter et al., 2008).

3.3.2 Quantum efficiency

Quantum efficiency is an image sensor characteristic that defines how many photons within a particular bandgap are required to generate free electron carriers. Quantum efficiency is the ratio of average number or electrons generated in a single pixel to the average number of impinging photons. Ideally, for every impinging photon on the PPD, one electron-hole pair is generated. Practically, the photoelectric effect is imperfect in a PPD and not all impinging photons generate an electron-hole pair. Some photons are lost due to reflection on the PPD surface or by absorption through layers above the photosensitive area of the pixel. The absorption coefficient of the photosensitive material in a PPD changes with wavelength of the impinging photon (Jain, 2016). This means that the quantum efficiency of an image sensor is not flat over its entire spectral range. The quantum efficiency curve for a CMOS APS sensor is shown in Figure 3-6.

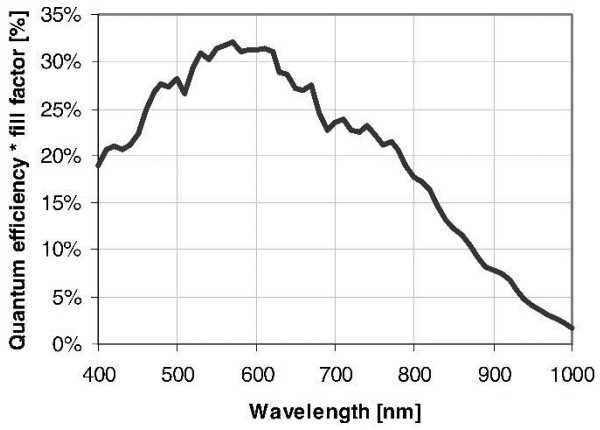

Figure 3-6: Quantum efficiency curve for a CMOS APS image sensor (Meynants et al., 2003)

The number of free-carrier electrons generated by the pixel is dependent on the wavelength of irradiance. Consequently, if an image sensor is calibrated to measure a certain light source, any changes to the spectral composition of that light source will affect the camera's calibration.

3.3.3 Full-well capacity

Each pixel in an image sensor has an electron storage capacity, commonly referred to as the full-well capacity (FWC). A pixel reaches saturation once all the free-carrier electrons available in the PPD have migrated into the depletion region and the capacity is reached. At

this point, the pixel signal output is constant even if light with greater intensity strikes the pixel (Jain, 2016). The full-well capacity of an image sensor is determined by the manufacturer.

3.3.4 Vignetting

In digital photography, images generally exhibit a radial reduction in pixel intensity towards the periphery of the image. This phenomenon is referred to as vignetting (Zheng et al., 2009). The major contributors of vignetting are optical and pixel vignetting. With optical vignetting, light paths are blocked within the lens body restricting the intensity of light measured striking the periphery of the image sensor. This can be reduced by stepping down the aperture to limit the light paths towards the centre and edges of the frame equally. The finite depth of the PPD wells in digital camera image sensors introduces an angular sensitivity to the light striking the pixel. The side walls of the photon well occlude light that impinges the pixel at steep angles, thus preventing the pixel from generating a signal (Goldman, 2010). Methods to prevent vignetting are discussed in further detail in Chapter 4.

3.4 Lambertian diffusion

To analyse the intensity distribution of concentrated solar radiation, a diffuse reflector was required. For this work, a Lambertian target was designed to intercept the focal plane, allowing the CMOS camera to capture an image of the energy distribution. In this chapter, principles of Lambertian diffusion and design of a Lambertian diffuse target are discussed.

3.4.1 Lambert's law of diffuse reflection

A Lambertian surface diffusely reflects light in all directions with the radiant intensity of light varying with cosine angle from the surface normal (Alma & Taylor, 2000). Consider an infinitesimal portion of a Lambertian surface denoted by A_T that receives an irradiance (E_s) from a light source as shown in Figure 3-7.

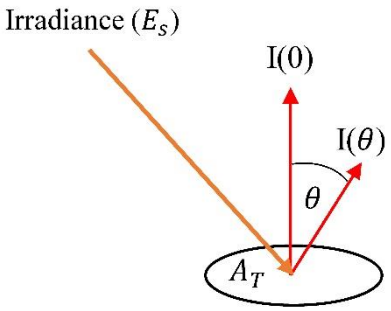

Figure 3-7: Diffuse-reflection off a Lambertian surface

The radiance is calculated by dividing the radiant intensity as a function of cosine angle (θ) by the projected area, as shown in Equation (3.1).

$$\frac{I(0)cos\theta}{A_T cos\theta} = \frac{I(0)}{A_T} \tag{3.1}$$

Since both intensity and apparent area follow the cosine law, it is evident that the radiance viewed at any angle from the normal of a Lambertian surface is the same. When a Lambertian surface is viewed by an image sensor, each pixel measures an infinitesimally small portion of the Lambertian surface (A_T) as shown in Figure 3-8.

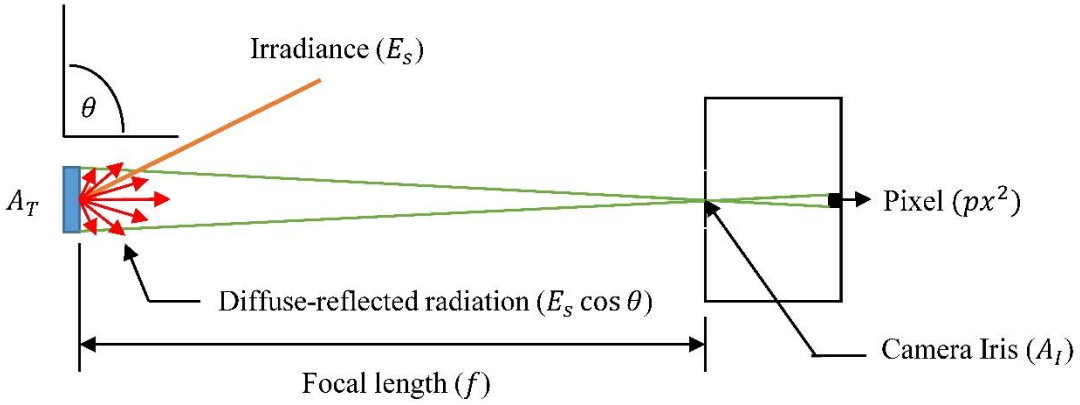

Figure 3-8: Diffuse-reflected irradiance on a small portion of a Lambertian surface detected by a single pixel element

A set of equations that describes the radiance viewed by each pixel in a digital camera was developed by Ho & Khalsa (2012). The signal response of a single pixel (*px*) in a CCD or CMOS camera is expressed in an arbitrary voltage that is produced due to an irradiance on the pixel. Consider an elemental portion of the Lambertian diffuse surface in two-dimensions illustrated in Figure 3-9.

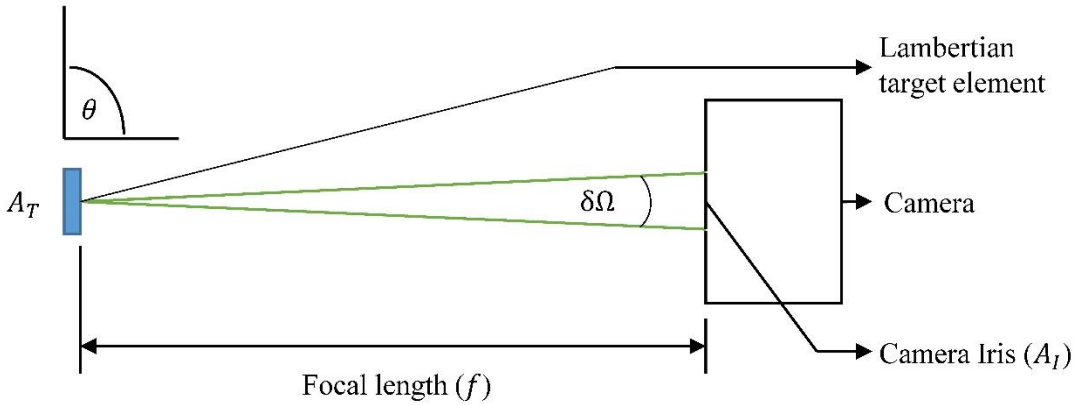

Figure 3-9: Solid angle subtended from a portion of a Lambertian diffuser to the camera iris

Since the radiant intensity (I_L) reflected off the Lambertian target element varies with the cosine angle (θ) between the target surface normal and the camera's line of sight. The irradiance measured by each pixel is equated as:

$$E_{pixel} = \frac{I_L \cos(\theta) \delta\Omega}{(px)^2} \tag{3.2}$$

where $\delta\Omega$ is the angle that subtends from the camera iris to the Lambertian surface (Figure 3-9). The reflected radiant intensity distribution off a Lambertian target can be defined by the bidirectional reflectance distribution function (BRDF), which quantifies the diffusion of Lambertian reflectance into a hemisphere (Figure 3-10).

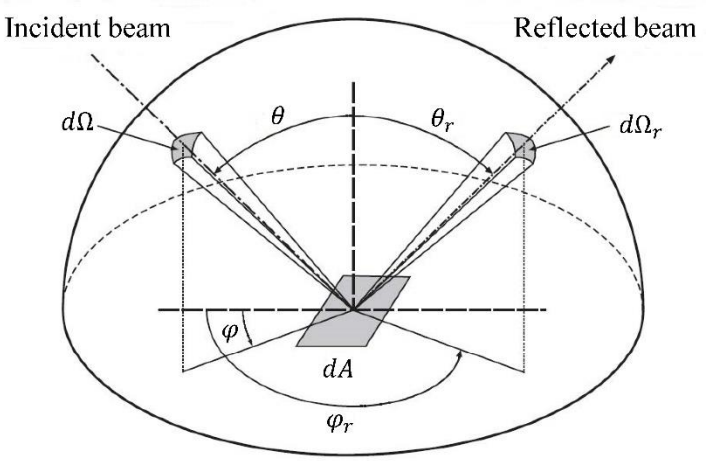

Figure 3-10: Illustration of the bidirectional reflectance distribution function (BRDF) (Göhring et al., 2011)

For energy to be conserved, the total power intercepted by the Lambertian target surface element (δA) with a known diffuse reflectivity (ρ) must be equal to the total radiant power diffuse-reflected into a hemisphere as shown in Figure 3-10. By recognising that angles θ_r and φ are the polar and azimuth angles in a spherical co-ordinate system, the energy balance can be equated as:

$$\rho E_s A_T = I_L \int_0^{2\pi} \int_0^{\pi/2} \cos(\theta_r) \sin(\theta_r)\, d\theta d\varphi \tag{3.3}$$

where E_s is the surface irradiance. Solving the double integral on the right-hand side of Equation (3.3) yields the following equation for reflected radiant intensity (I_L) from a Lambertian reflector:

$$I_L = \frac{\rho_s E_s A_T}{\pi} \tag{3.4}$$

The solid angle ($\delta\Omega$) from Equation (3.2) can be calculated with the assumption that the area of the camera iris (A_I) is small compared to the focal length (that is the distance from the camera to the target surface). The solid angle is therefore given as:

$$\delta\Omega = \frac{A_I}{f^2} \tag{3.5}$$

Substitution of Equations (3.4) and (3.5) into Equation (3.2) yields the following equation for pixel irradiance:

$$E_{pixel} = \frac{\rho_s E_s A_T \cos(\theta) A_I}{\pi (px)^2 f^2} \tag{3.6}$$

For a constant irradiance (E_s) on a Lambertian diffuse surface, the pixel irradiance intensity will change if the area of the camera iris (A_I) and focal length (f) are altered.

3.4.2 Lambertian target design

The purpose of the Lambertian target is to intercept the concentrated solar radiation at the focal plane of the solar furnace and redirect the diffuse reflected solar radiation towards the CMOS camera. To improve the concentration accuracy of SERAFF's parabolic concentrator, an adjustment mechanism was developed to incrementally adjust the position of each individual petal within the dish array (Khan et al., 2016). Figure 3-11 illustrates a CAD model of the petal adjustment mechanism.

The petal alignment process required a visual inspection of the change in light distribution once a rotational or translational adjustment was made to each individual petal. The concentration accuracy was determined qualitatively by optically viewing the light distribution diffused off a Lambertian target. In this procedure, a 500 mm x 500 mm matte white refractory board was used to intercept the radiative flux at the focal plane. Refractory boards have high diffuse reflectance, making it possible to approximate the focal spot size by analysing the intensity distribution with a digital camera. The spatial flux distribution measured across the refractory board is shown in Figure 3-12.

The irregular radiative flux distribution intercepted by the refractory board indicated a focal spot approximately 260 mm in diameter. Refractory boards are brittle and have an anisotropic surface roughness making them unsuitable as Lambertian targets for spatial flux characterisation. However, this result provided reasonable dimensional constraints for the design of a more robust Lambertian target.

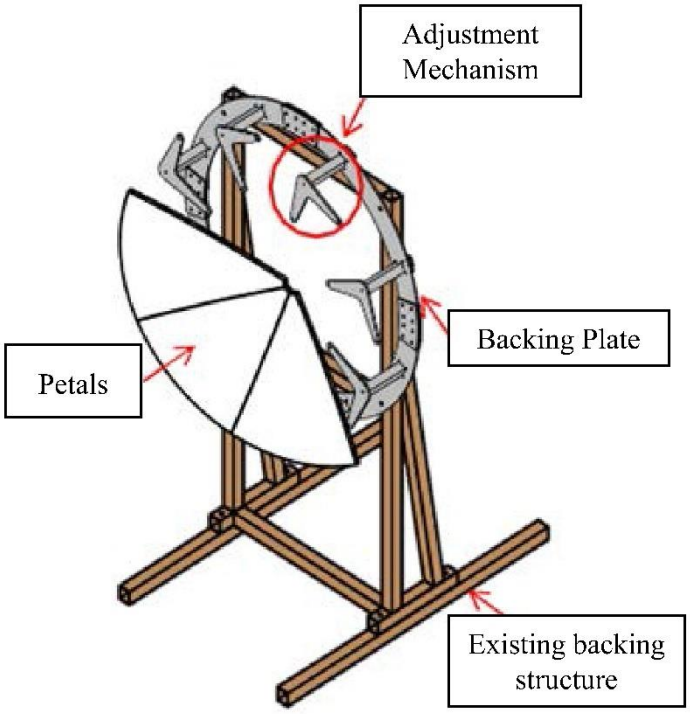

Figure 3-11: CAD model of SERAFF's 3 m diameter parabolic concentrator and the petal adjustment mechanism assembly (Khan et al., 2016)

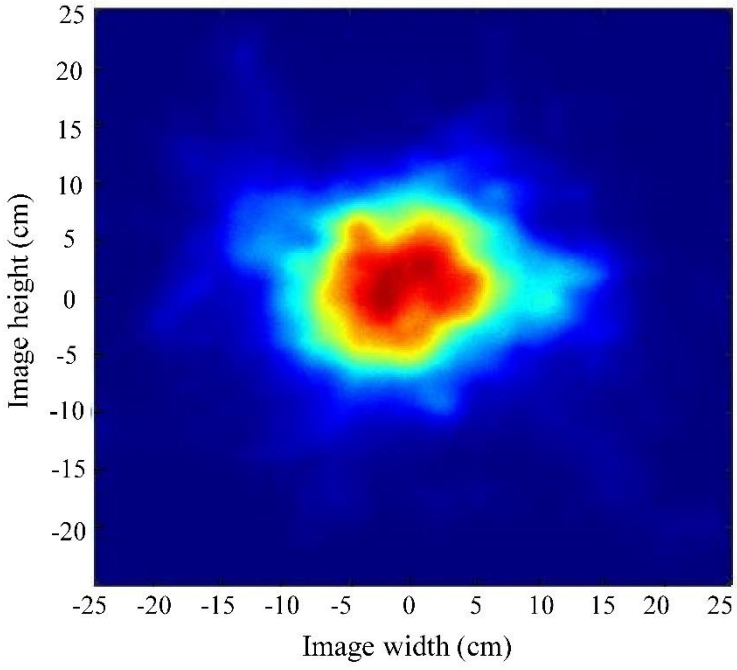

Figure 3-12: Non-dimensional radiative intensity distribution on a 500 mm x 500 mm refractory board after the petal alignment procedure

Conventional solar flux mapping systems typically employ a metal plate with a plasma-sprayed alumina surface as their Lambertian target (Ulmer et al., 2002; Lee et al., 2014; Röger

et al., 2014). Alumina (Al_2O_3) is a ceramic material that exhibits excellent wear resistance, high temperature resistance and high diffuse reflectance (Ctibor et al., 2007). When fine alumina particles are imbedded on to a metal substrate using plasma-spraying techniques, the sprayed surface inherits the properties of the ceramic material. Based on these factors, an alumina plasma-sprayed Lambertian target was selected for use in this study.

Plasma-spayed ceramic deposits have an anisotropic, porous and layered microstructure, reducing the strength of the polycrystalline microstructure (Kluthe & Kollenberg, 2013). The brittle nature of alumina also contributes to the likelihood of crack formation under cyclic thermal loading. Additionally, the variation in thermal properties of the metal substrate and alumina coating introduces susceptibility to the effects of thermal shock. Prolonged exposure to intensive solar flux loads during the petal alignment process or in the case of a facility malfunction may therefore result in cracks in the alumina surface due to stresses induced by the differential thermal expansion of the alumina coating and metal substrate. Irradiance that falls along the crack path will cause the reflected light to behave in an unpredictable manner. To this end, a Lambertian target was designed to withstand the high thermal loads at the focal plane of the SERAFF solar furnace. Figure 3-13 illustrates the workflow diagram used to design the Lambertian target.

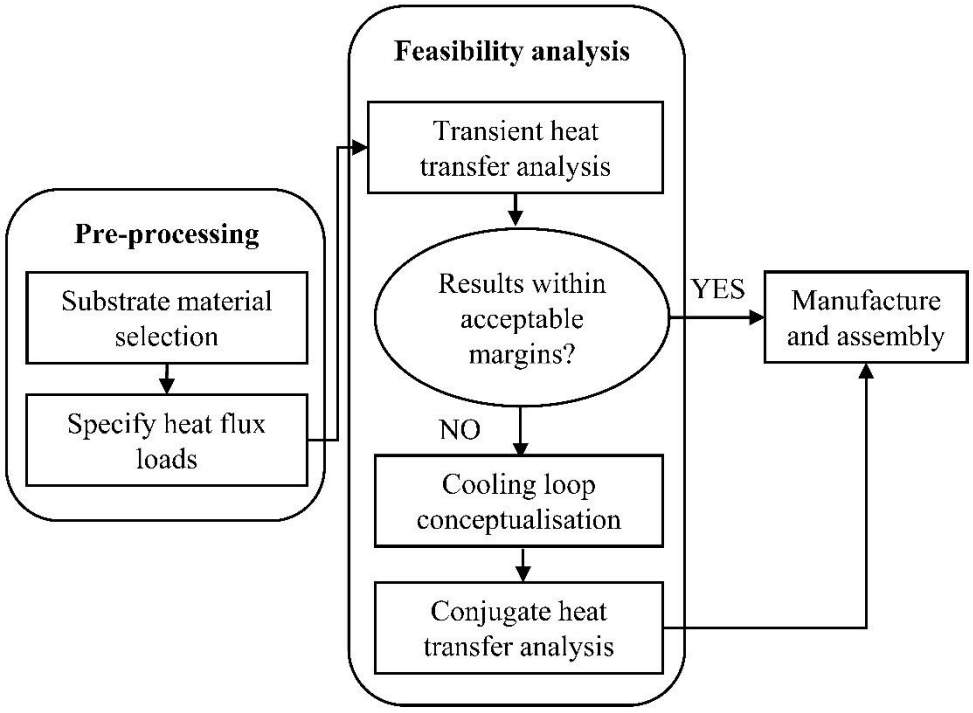

Figure 3-13: Lambertian target design workflow diagram

The following attributes were considered favourable in selecting an appropriate substrate material for the Lambertian target:

- Good stability at high temperatures

- Corrosion resistance
- Low weight

An aluminium plate was selected for use as the substrate material for the Lambertian target. Aluminium's low density makes it approximately three times lighter than steel and copper. An oxide layer forms over an aluminium surface when exposed to air, giving it good corrosion resistance. Lastly, aluminium has a high thermal conductivity, allowing heat to be extracted from it at a rapid rate when actively cooled using heat transfer fluids, thus reducing the surface temperature during use. To effectively capture the light spread across the focal plane, a 500 mm x 500 mm square aluminium plate with a thickness of 12 mm, was chosen as the substrate material for the Lambertian target. Even though the focal spot diameter was estimated to be approximately 260 mm, a larger target area was selected to compensate for a larger focal spot size.

3.4.3 Transient heat transfer analysis

A transient finite element heat transfer analysis was conducted using ANSYS™ to examine the variation in temperature distribution of the Lambertian target over time during prolonged exposure to a constant heat flux boundary load. ANSYS™ a finite element analysis software package used to simulate mechanical, structural, heat transfer, fluid dynamic engineering problems. The symmetrical nature of the square geometry being modelled and heat flux boundary allowed for one quarter of the plate to be modelled in this simulation. Due to the simplicity of the square geometry being modelled, the choice of using a quadrilateral mesh was considered sufficient to perform the transient heat transfer analysis. The axisymmetric nature of the concentrated solar flux distribution allowed the target to be modelled with quarter symmetry to greatly reduce solving time. The material and mesh properties used for the simulation are shown in Table 3-2.

Table 3-2: Material and mesh properties of aluminium Lambertian target model

Substrate Material Properties	
Material	Aluminium 6082
Thermal conductivity	185 W/mK
Specific heat	880 J/kgK
Density	2700 kg/m^3
Mesh Properties	
Element type	Quadrilateral
Element size	2.0 mm
No. elements	93750

The effective energy output of the SERAFF solar furnace is influenced by the sun's position and intensity, which are time and date specific factors. This makes it difficult to isolate the

specific time and date at which the facility is operating at peak performance. For this reason, the thermal power developed by SERAFF on 22 December (summer solstice) was considered to be a conservative representation of its peak performance. The spatial solar flux distribution obtained from the summer solstice ray-tracing analysis, conducted in Chapter 2, was used as the heat flux boundary load condition on the front face of the target. To account for greater intensities, a factor of 1.5 was applied to the spatial flux data.

Alumina plasma-sprayed coatings are approximately 0.15 mm thick and thus conduction through the coatings may be considered negligible. The reflectance of plasma-sprayed alumina coatings is reported to be approximately 80 % within the visible bandgap of the solar spectrum (Toru et al., 2016). As a result, approximately 20 % of the concentrated solar flux is absorbed by the aluminium substrate.

The spatial heat flux load was scaled by a factor of 0.2 and applied as a boundary condition to the front face of the aluminium target. Radiative and convection heat transfer coefficients were applied to each wall on the plate. The transient heat transfer solver was set to iterate the temperature distribution across the plate for 300 s with a step size of 10 s. The temperature history and temperature distribution on the front face of the target are shown in Figures 3-14 and 3-15 respectively.

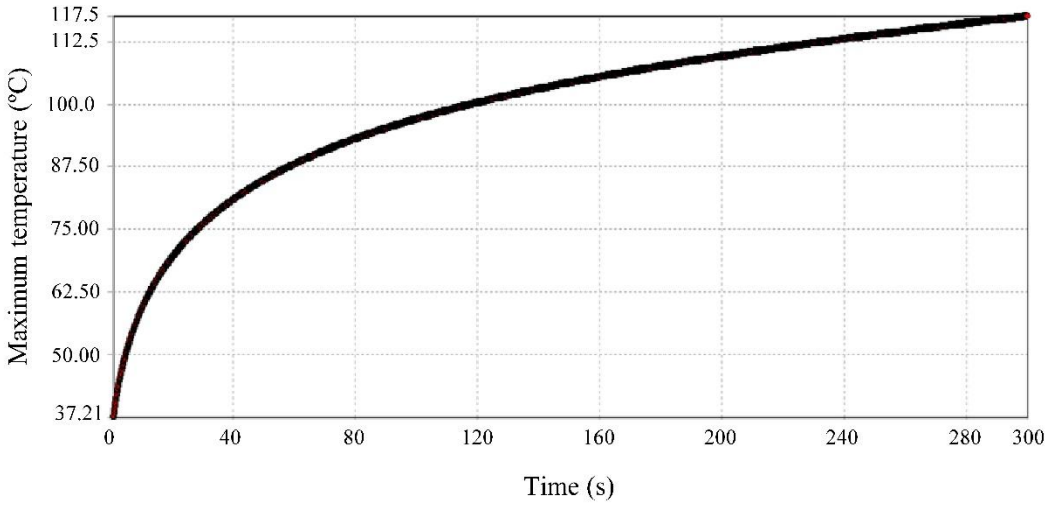

Figure 3-14: Maximum temperature on the aluminium substrate from 0 s to 300 s

The results indicated a rapid increase in target temperature during the first 2 min of exposure, reaching temperatures of approximately 100 °C toward the centre of the target. The thermal expansion rate of aluminium is approximately three times that of alumina. Alumina plasma-sprayed coatings have an anisotropic porous microstructure, reducing the surface area between adjacent particles and creating stress concentrations (Safai & Herman, 1977). The thermal expansion mismatch between the aluminium substrate and alumina coating may aggravate

thermal stresses of the alumina coating when heated. This can induce stress fields at different zones along the substrate-coating interface (Pawlowski, 1991). The presence of a surface crack within the alumina coating will influence the optical characteristics of the coating. As a result of these risks, a cooling system was designed to reduce the temperature distribution of the Lambertian target during use and to mitigate the effects of cyclic thermal loading.

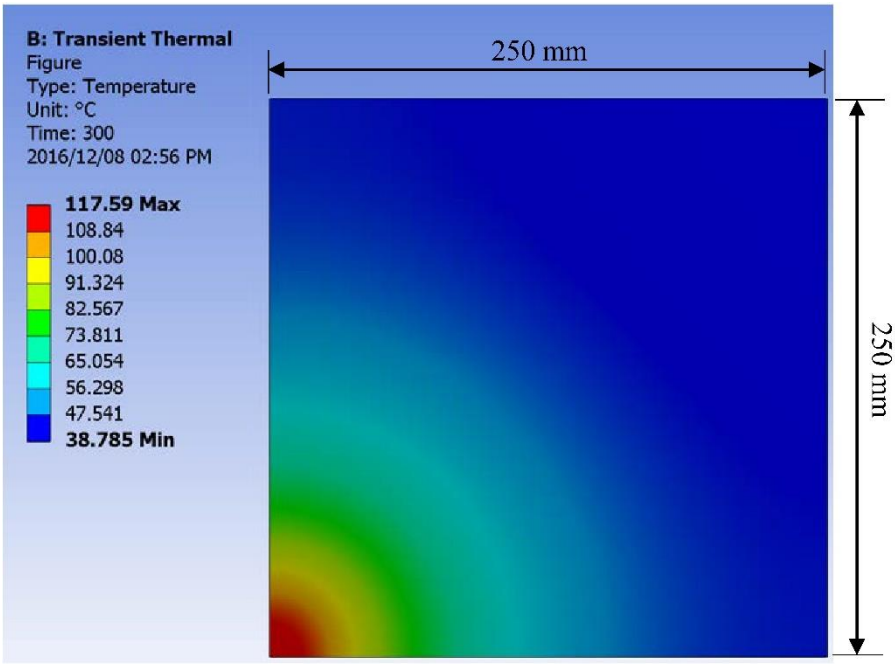

Figure 3-15: Temperature distribution on the front face of the aluminium substrate after 300 s

3.4 Actively-cooled Lambertian target design

An active water-cooling system was developed to reduce the working temperature of the Lambertian target during use. The distributed flux profile generated by the solar furnace is approximately Gaussian, thus there is a higher energy density towards the centre of the focal spot compared to the energy density at the periphery. The spatial flux distribution after the petal calibration process was spread across a focus diameter of approximately 260 mm. An eight-pass cooling loop that covers a 200 mm square region located at the centre of the aluminium substrate was adopted to provide adequate cooling to the exposed region of the Lambertian target.

3.4.1 Conjugate heat transfer analysis

A conjugate heat transfer analysis was required to determine the effectiveness of the Lambertian target cooling circuit. The STAR CCM+^{TM} computational fluid dynamics (CFD) software package was used in this study to simulate the exchange of thermal energy between the interfaces of the solid aluminium body and the fluid domain. The solid and fluid region

geometries were generated using CAD software with appropriate boundary conditions applied to each domain so as to define the interaction between the system and its surroundings. Figure 3-16 illustrates an exploded assembly of the solid and fluid domains for this simulation.

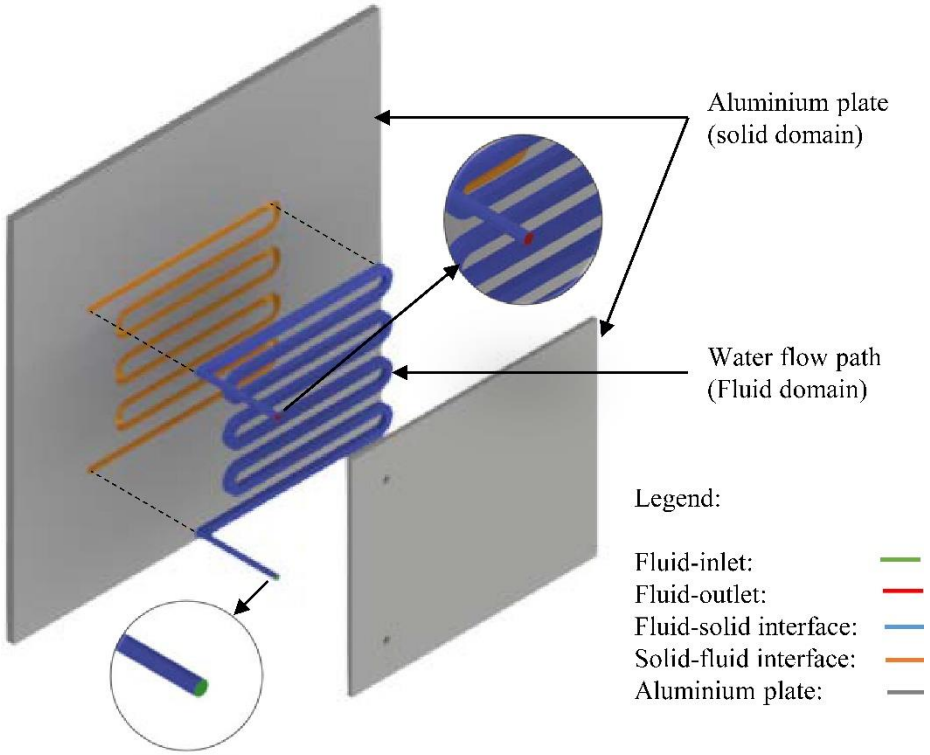

Figure 3-16: Illustration of the fluid and solid domains for the Lambertian target conjugate heat transfer assembly

The boundary condition type applied to each domain is given in Table 3-3.

Table 3-3: Lambertian target boundary condition specifications

Boundary designation	**Boundary type**
Fluid: inlet	Mass flow inlet
Fluid: outlet	Pressure outlet
Fluid: Fluid-solid interface	Contact interface boundary
Solid: Aluminium plate	Wall
Solid: Solid – Fluid interface	Contact interface boundary

A polyhedral mesher was used to generate a volume mesh composed of polyhedral-shaped cells in both the solid and fluid regions. Compared to tetrahedral cells, polyhedral cells have many faces allowing for efficient and accurate calculation of local flow distributions even along walls, edges and corners (Peric & Ferguson, 2004). The size of the fluid domain was significantly smaller than that of the aluminium plate, and so a small mesh size was required to accurately solve the energy equations at the solid-fluid interfaces. To reduce computational

solving time, mesh refinement was applied to the fluid domain only. Figure 3-17 illustrates the meshed Lambertian target assembly.

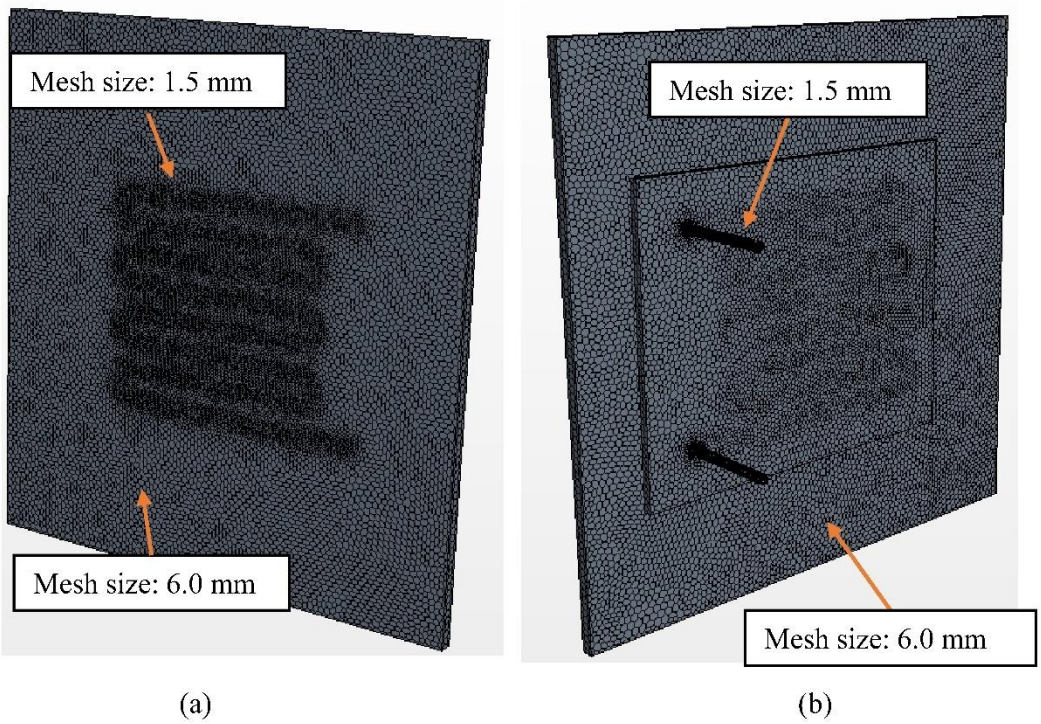

Figure 3-17: Meshed Lambertian target front view (a) and back view (b)

The mesh details for the simulation are provided in Table 3-4.

Table 3-4: Mesh details for the water-cooled Lambertian target

Mesh properties	
Mesh type	Polyhedral
Solid region base size	6.0 mm
Fluid region base size	1.5 mm
No. cells	172366

A pump system was used to circulate water through the cooling channels in the Lambertian target. The system comprised a PKM60 Pedrello centrifugal pump, drawing water from a tank situated within the SERAFF housing structure. The system head for the closed-loop water reticulation system was determined by adding the measured system head on both the suction and discharge sides of the pump. This was calculated to be 0.8 m, neglecting pipe frictional losses and the pressure drop across the cooling loop. The pump can supply a total head of up to 40 m, which exceeded the system head requirements for the given setup. A valve on the suction side was also available to adjust the fluid pressure and regulate the flow rate. The pump characteristic curve was used to estimate the flow rate through the cooling channels for a total system head of 10 m. The system head ensured that the Lambertian target was effectively

cooled during use. The mass flow rate inlet boundary condition was therefore set to 0.583 kg/s, which corresponded to a system head of 10 m.

A steady, incompressible and segregated flow model was selected for the simulation. The cooling channel flow regime was calculated using the dimensionless Reynolds number:

$$Re = \frac{4\dot{m}}{P\mu} \tag{3.7}$$

where $\dot{m}$ is the mass flow rate through the cooling channels, P is the cooling channel wetted perimeter and μ is the dynamic viscosity of water. The Reynolds number indicates wether the flow regime is laminar or turbulent, with laminar flow conditions expected for Re $\leq$ 2300 and turbulent conditions for larger values. The Reynolds number for these flow conditions indicated a turbulent flow regime for the water passing through the cooling channels. The Reynolds-Averaged Navier stokes (RANS) turbulent flow equations were selected for the simulation, implementing the k-epsilon turbulence model. This model was selected as a result of its low computational requirements and higher accuracy for high Reynolds number flow regions. The Realizable Two-layer K-Epsilon model was also selected, which includes additional equations for flow at the viscous sublayer. This model is combined with two-layer approach, which gains the added flexibility of an all y^+ solver.

Turbulent flows are greatly influenced by the presence of walls, where the viscosity-affected regions have large gradients in their solution. Accurate representation of these regions is thus required to predict the behaviour of wall bounded flow regimes. The wall-y^+ is a dimensionless distance often used in CFD to describe laminar and turbulent influences at the near-wall regions. An all-y^+ wall treatment solver was used in conjunction with the k-epsilon turbulence model. This solver was formulated as a hybrid for coarse meshes that use the high wall-y^+ and fine meshes that use a low all-y^+ treatment ($0 < y^+ < 300$). Prism layer meshing was used to solve internal near-wall boundary layer flow regimes. This is critical for determining heat transfer, drag and pressure drop at the wall of the viscous sublayer. The thickness of the viscous sublayer was estimated according to Equation (3.8).

$$y = \frac{y^+ \nu}{u^*} \tag{3.8}$$

In the above, ν is the kinematic viscosity of water and u^* is the near-wall velocity of the fluid domain. To solve this equation, a y^+ value was estimated that falls within the range of the solver. The parameters used to describe the wall treatment were validated by running an initial exploratory simulation and checking the y^+ values at the walls of the fluid domain. The calculated boundary layer thickness (y) was 1.8 mm. Three prism layers were used to make up

the overall boundary layer in the fluid domain. The resolved y^+ values were between 14 and 146, which was within the acceptable range of the all y^+ wall treatment solver. Therefore, the near-wall spacing was considered adequate for this flow regime. A detailed section of the meshed cooling channel is shown in Figure 3-18.

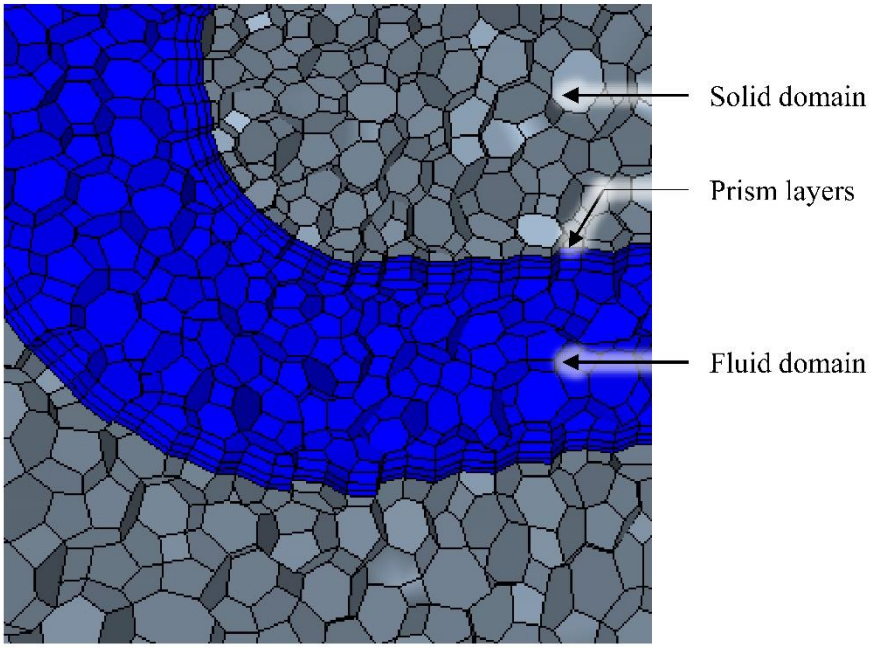

Figure 3-18: Detailed section of the meshed Lambertian target cooling channels with prism layers

The spatial heat flux data previously used to simulate the transient temperature distribution on the Lambertian target was used as the applied heat flux load for the conjugate heat transfer simulation. The heat flux thermal boundary on the front face of the target was therefore scaled by a factor of 0.8 to account for the 80 % reflectivity of the alumina surface. The thickness of plasma-sprayed alumina coatings is approximately 0.15 mm and conduction through the coating was therefore ignored. Simulation convergence was determined by monitoring the residuals (Figure 3-19), average fluid temperature at the outlet and the average heat transfer coefficient at the fluid-solid contact boundary (Figure 3-20).

The steady-state fluid temperature at the outlet was predicted to be approximately 25.4 ºC and the average heat transfer coefficient at the fluid-solid contact boundary was approximately 37510 W/m^{2}K. The water temperature is required to be maintained below 90 ℃ to prevent the water from boiling inside the aluminium plate. Under steady state conditions, the maximum temperature at the wall of the fluid domain was simulated to be 35.2 ºC towards the centre of the aluminium plate where the concentrated solar flux density is at a maximum. Figure 3-21 shows the temperature distribution at the wall of the fluid domain.

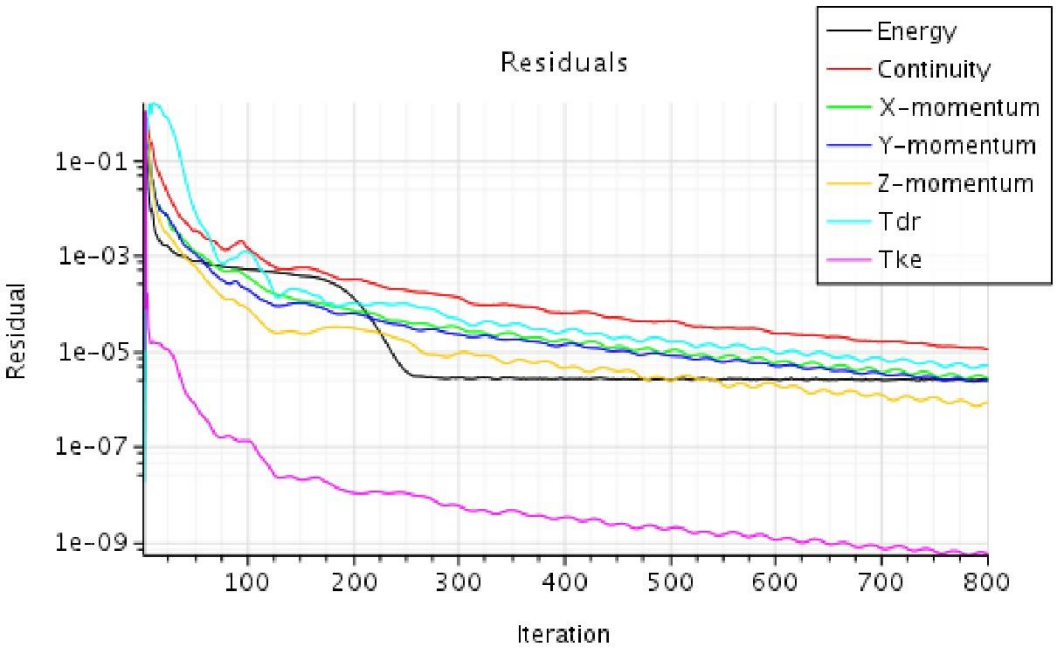

Figure 3-19: Residuals monitor for the conjugate heat transfer analysis indicating convergence

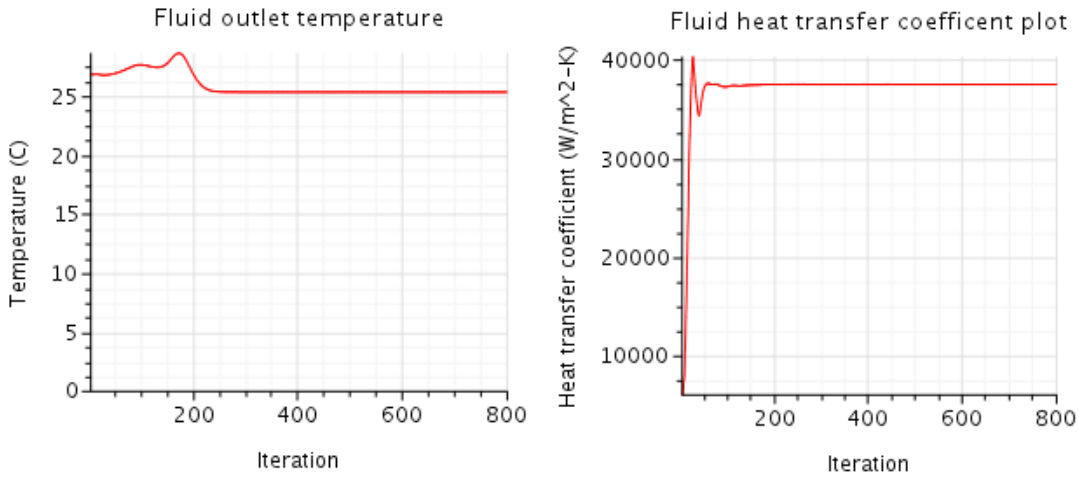

Figure 3-20: Average fluid outlet and heat transfer coefficient plots as a function of solver iteration number

The corresponding maximum plate temperature was calculated to be approximately 44 ºC towards the centre of the plate (Figure 3-22). The resultant temperature difference between the centre and outer regions of the aluminium plate was approximately 20 °C. In reality, lower temperatures can be expected due to the temporal and spatial variations in SERAFF's thermal energy output. These low temperature gradients on the alumina coated surface were considered insufficient to cause permanent damage to the target during operation and the cooling channel design was deemed adequate for this application.

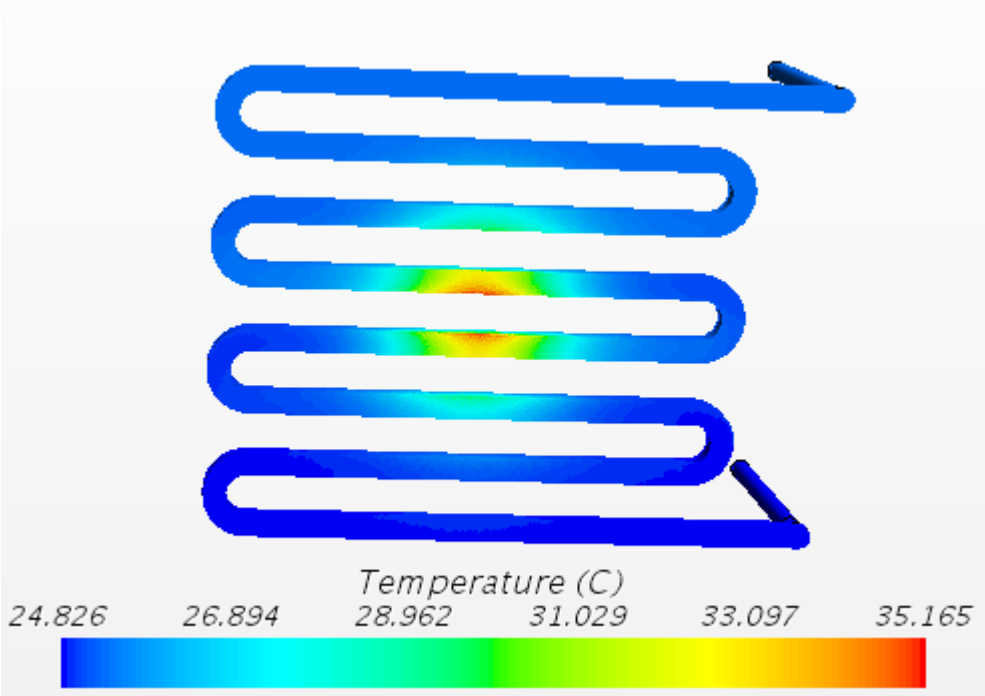

Figure 3-21: Wall temperature distribution of the water-cooled Lambertian target fluid domain

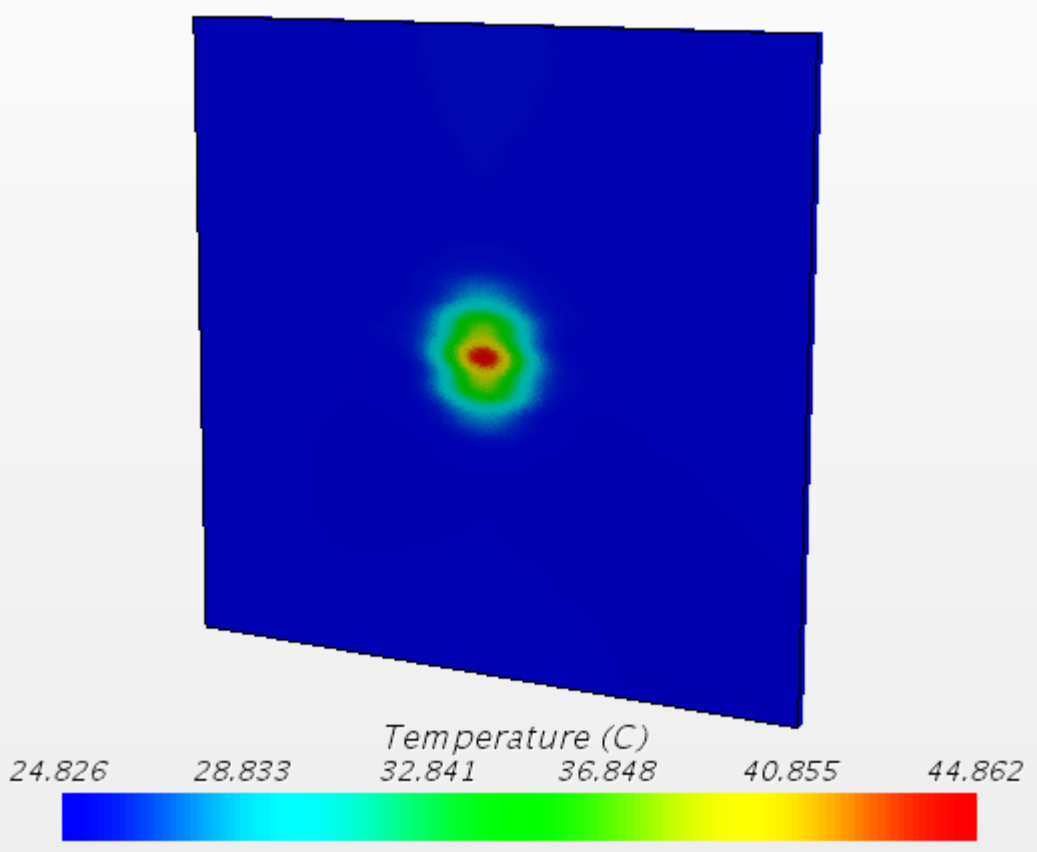

Figure 3-22: Temperature distribution on the front face of the Lambertian target

3.4.3 Lambertian target fabrication

The Lambertian target was fabricated from a 500 mm x 500 mm aluminium 6082 T6 plate with a thickness of 12 mm. Detailed CAD drawings for this component are given in Appendix B. The cooling channels were cut with a 10 mm end mill cutter on a 3-axis CNC machine.

To achieve a Lambertian diffuse surface, plasma-spraying techniques were employed. In this process, powder particles are infused on to a metal substrate by carrying the particles in an inert gas stream into a high temperature plasma jet. The particles are melted down and propelled towards the substrate material at high speeds, typically between 200 m/s and 300 m/s. As the accelerated particles collide with the stationary substrate material, they are flattened and quenched, creating a layered, porous microstructure coating on the exposed surface. Figure 3-23 illustrates the system setup for this procedure.

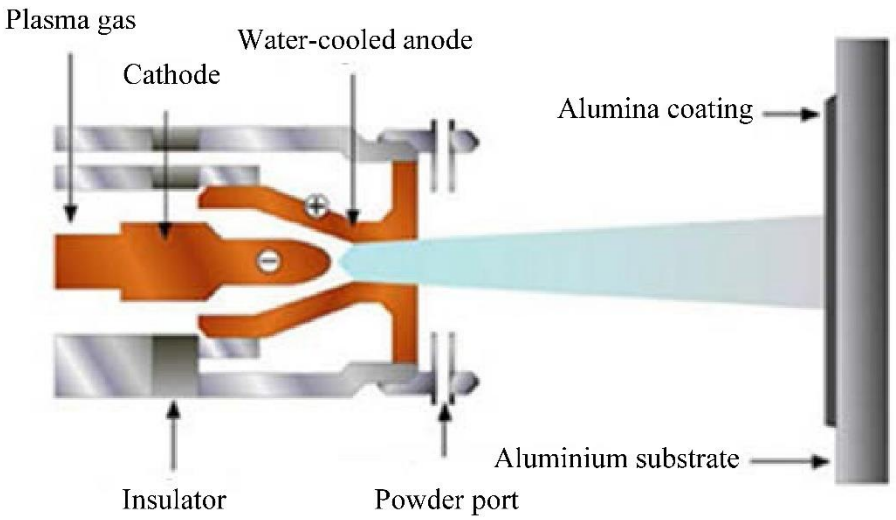

Figure 3-23: Schematic of the plasma-spraying process (de l'Avouerie, 2000)

Before plasma-spraying, the aluminium plate was sand-blasted to increase the surface roughness and improve the mechanical interlocking between the substrate material and alumina coating. To prevent the plate from warping from this procedure, a minimum substrate thickness of 12 mm was recommended by the company Thermaspray™. The Lambertian surface was then created by depositing 99% pure alumina powder particles on to the aluminium substrate. The fabricated Lambertian target is shown in Figure 3-24.

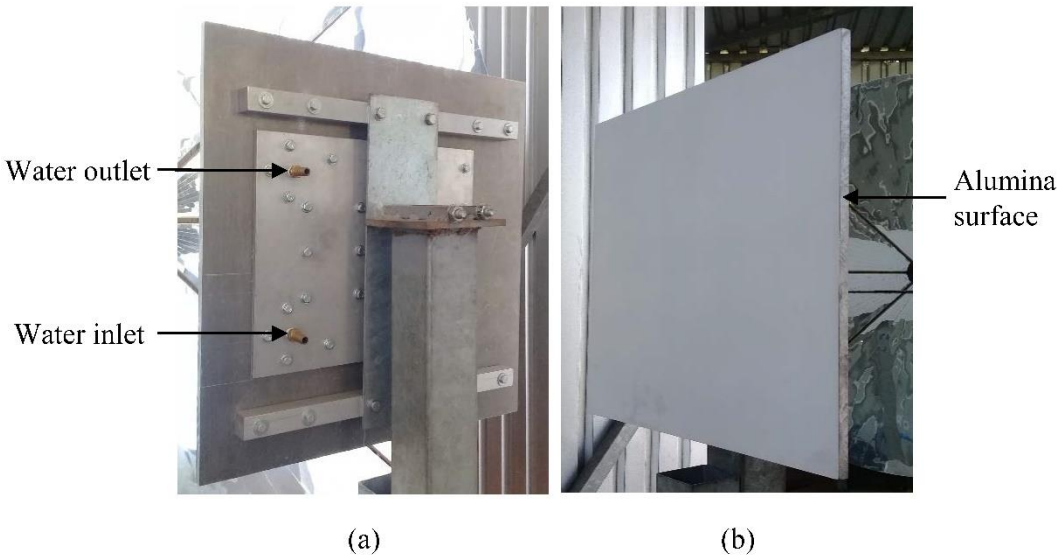

Figure 3-24: Assembled water-cooled Lambertian target back view (a) and front view (b)

3.5 Target Positioning System

The receiver stand that was previously used to mount test articles for the SERAFF solar furnace had minimal adjustment capabilities. Preliminary tests indicated that test articles mounted on the existing receiver stand were offset from the focal plane. This meant that only a fraction of the concentrated solar flux distribution could intercept receivers and test articles. To remedy this, a target-positioning system (TPS) was developed to adjust the position of the Lambertian target used for the solar flux characterisation system and future test articles designed for the SERAFF solar furnace. The TPS permits translational movement along the lateral (*x*-axis) and longitudinal (*z*-axis) directions respectively. The platform was assembled upon the existing SERAFF test bed that traverses along a rail system. The two translational axes are controlled independently using two platforms that move relative to each other along their specific translational axes.

The platform frames were built from modular t-slot aluminium extrusions. These 45 mm x 45 mm aluminium products are extruded into geometrically rigid shapes, resulting in a low-weight and low material quantity part with good structural rigidity. A major benefit of using these extrusions is that they do not require any welding to join to one another. Specially designed t-bolts and 90° corner brackets are used to join the aluminium extrusions together. The bottom frame varies the target's longitudinal position (*z*-axis) and another frame mounted directly above it varies the lateral position (*x*-axis). The assembled TPS is shown in Figure 3-25.

The overall platform height was restricted so that the structure does not shadow the bottom portion of the parabolic concentrator. R-groove sliding gate wheel brackets were manufactured

and mounted to the side of the aluminium frames to minimise the spacing between each platform. Galvanised round bar with a diameter of 16 mm was used as the linear guide for each wheel.

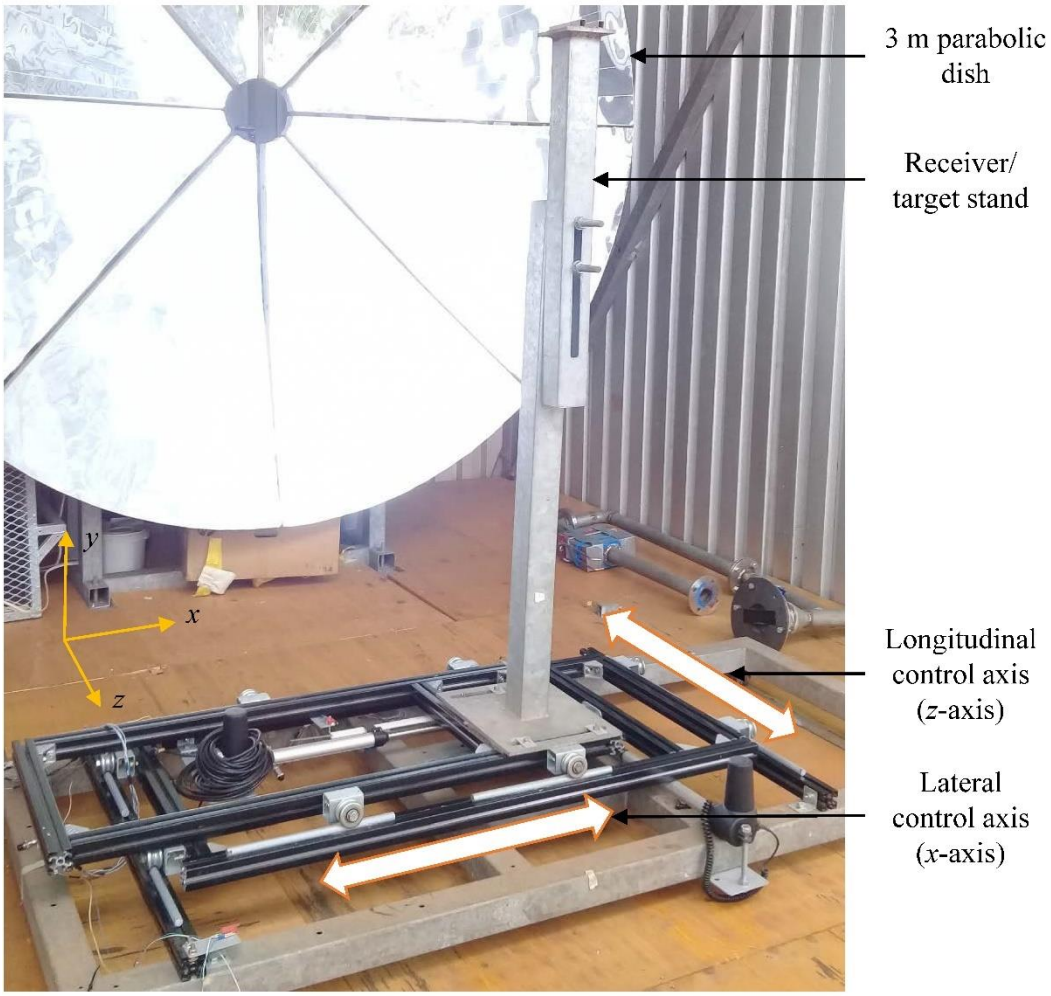

Figure 3-25: Assembled target positioning system (TPS) at the SERAFF site

Static beam loading calculations were used to determine the worst-case loading scenario of the TPS platform. The modified wheel kit assemblies were identified to be the weakest component of the structure. Each wheel was mounted on to a square bar bracket and bolted on to the side of the aluminium frame. When a receiver or test article is mounted on to the receiver stand, the static load is distributed to each wheel. The load that each wheel experiences reduces with increasing distance away from the receiver stand. Therefore, the wheel kits on the top platform, nearest to the receiver stand were considered for the worst-case loading scenario. By treating the M12 wheel axle bolts as rods fixed at a single end, the maximum allowable force to prevent the wheel axles from exceeding the maximum allowable bending stress was calculated to be 1063 N. Therefore, the maximum allowable mass of a test article mounted on the TPS is limited to 106 kgs.

Two SKF CARE33A linear actuators were used to adjust the target's position along the specified translational axes. The stroke length of each linear actuator is 300 mm with a rated push-pull load limit of 2000 N. Macro adjustments to the TPS's longitudinal position are made by traversing it along the rail system. Since the actuators have no built-in encoders for position feedback, limit switches were mounted on to the aluminium frame to stop the motors at their maximum and minimum displacements.

A graphical user interface (GUI) was designed using Laboratory Virtual Instrument Engineering Workbench (LabVIEW™) to control the actuators remotely. This ensures safe control of the Lambertian target or any test article during facility operation. LabVIEW™ is a versatile graphical programming tool developed by National Instruments. This programming environment was already used previously for the heliostat solar tracking algorithm due to its ability to perform real-time parallel processing at high speeds (Perumall, 2016). The goal was to use a single programming platform to control all SERAFF's control systems and data acquisition processes.

An Arduino mega 2560 microcontroller was used to control the linear actuators. This low-cost device has 52 digital input/output pins, 15 of which can be configured for pulse width modulation (PWM). The LINX software package was used to interact with the Arduino in the LabVIEW environment. An Olimex™ VNH3SP30 motor controller was used for polarity switching and surge protection and can be used for DC motors rated up to 36 V, 30 A. These specifications were sufficient as the linear actuator motors were rated for 24 V 4 A. Figure 3-26 shows the linear actuator control circuitry.

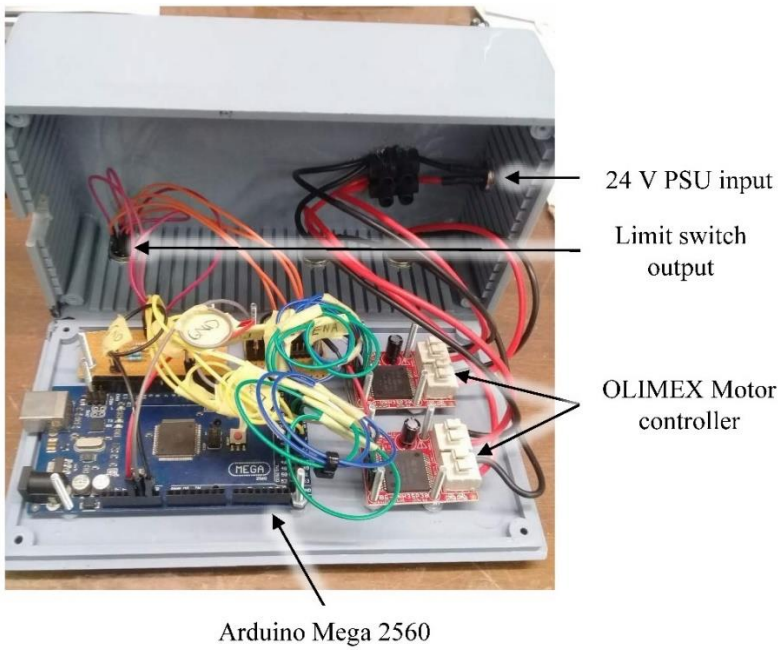

Figure 3-26: TPS motor control circuitry

The software application for the TPS was integrated with the existing heliostat control code. Using a tab-based selection panel, the user can alternate between the different control and data acquisition algorithms used for the SERAFF solar furnace. The user can specify the motor's direction by changing the state of the toggle switches on the front panel and or start the motors at will. In addition, the motor can be controlled programmatically allowing for safety protocols and other automated processes to call the TPS control algorithm within LabVIEW. The TPS GUI is shown in Appendix C.

Chapter 4 Measurement methods and instrumentation

4.1. CMOS camera photo response characterisation

Spatial measurements of concentrated solar flux were acquired using a Canon electro-optical system (EOS) 1200D DSLR camera. The camera was low in cost and featured a high-resolution APS imaging sensor. The camera was also compatible with LabVIEW allowing camera functions and settings to be programmatically controlled. The specifications are given in Table 4-1.

Table 4-1: Canon EOS 1200D CMOS camera specifications (Rhem, 2015)

Canon EOS 1200d specifications	
Specification	Value
Aperture range (f-stops)	f/5.6 – f/29
Shutter speed range	1/4000 – 30 s
ISO sensitivity range	100 – 6400
Image sensor size	14.9 x 22.3 mm
Pixel size	18.5 μm^2
Resolution	5202 x 3465
Pixel bit-depth	16-bits

The camera's wide aperture and shutter speed range provide sufficient exposure control to suit SERAFF's concentrated radiative energy output. The photo response of an image sensor is its ability to convert radiant energy into an electrical signal. In digital photography, the signal is amplified and passed through an analogue to digital converter so that the signal data can be read by a computer. The most simplistic form of an image is a two-dimensional array with each element in the array representing the measured intensity at each pixel. These images are referred to as grayscale images, since they only contain the pixel spatial data and the corresponding gray value that is proportional to the intensity of light measured by the pixel. The range of values that represent intensity at each pixel is dependent on the bit-depth of the camera. The Canon EOS 1200D camera has a bit-depth of 16, meaning that there are 2^{16} (65535) intensity values available at each pixel. Figure 4-1 illustrates conversion of measured pixel data into a grayscale image.

Ideally, a CMOS image sensor responds linearly to incident photons that impinge each pixel. However, to simulate the logarithmic photo response of the human eye, consumer grade cameras incorporate gamma encoding into the design of their image sensors. Gamma encoding redistributes higher values of measured luminance logarithmically so that the image sensor can operate over a broader range of illuminance (Hoang et al., 2010). To correlate the

measured grayscale output of the camera to solar flux, measurements must be restricted to the linear portion of the camera's photo response curve.

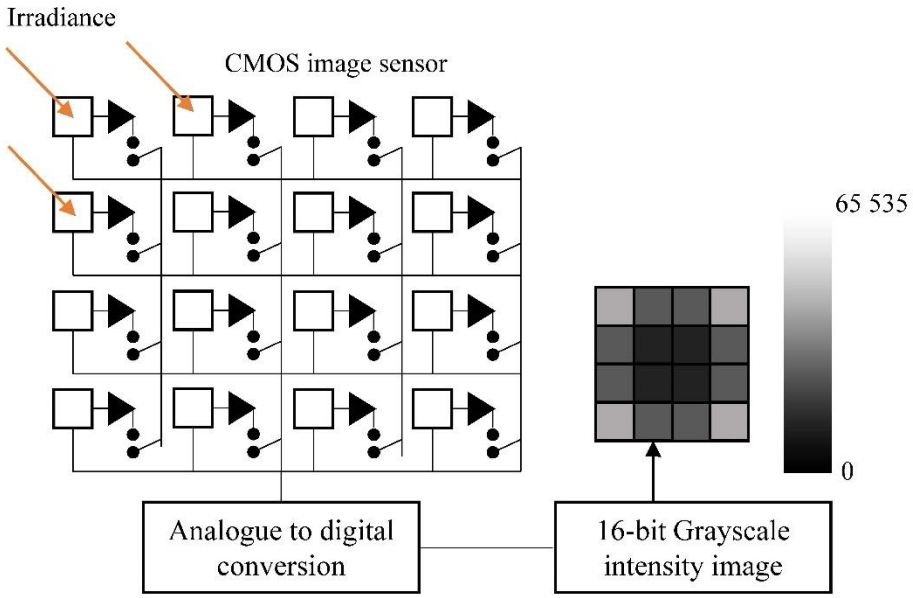

Figure 4-1: CMOS Image sensor signal digitalisation and grayscale image display

The photo response for each pixel can be expressed as the number of impinging photons (μ_p) that reaches each pixel (Jain, 2016). An expression for the number of impinging photons is given in Equation (4.1).

$$\mu_p = \frac{(px)^2 t_{exp} E_{pixel} \lambda}{hc} \tag{4.1}$$

Here t_{exp} is the exposure time, h is Planck's constant (6.626 x 10^{-34} Js) and c is the speed of light (3 x 10^8 m/s). For a constant irradiance striking a known pixel area, the number of impinging photons that the pixel measures can be altered by changing the exposure time (t_{exp}), while maintaining a constant aperture. This is equivalent to changing the intensity of the light source and keeping a constant shutter speed (Mojiri et al., 2015).

The photo response curve of the canon EOS 1200D image sensor was characterised by quantifying the spatial distribution of a Lambertian target illuminated under direct sunlight. Since it was not possible to vary the intensity of sunlight incident on the Lambertian surface, the shutter speed setting of the camera was altered to vary the exposure. The camera's position relative to the target, aperture and focus were held constant throughout the experiment.

The experiment was performed under clear-sky conditions so that the irradiance on the Lambertian surface would not be altered. The Lambertian target was moved out of the housing structure and exposed to direct sunlight (Figure 4-2).

Figure 4-2: Lambertian target illuminated by direct sunlight

To maintain collinearity between the target surface normal and the camera's central axis, the camera was mounted on to a tripod stand to view the target through a circular opening located at the centre of the parabolic dish. Multiple images of the illuminated Lambertian target were captured with different shutter speeds in quick succession. A total of 22 images were acquired and cropped at the same spatial co-ordinates so that the pixel data within a 100-pixel square region of the Lambertian target remained. The image sensor exposure was changed between images by doubling the shutter speed. A code was developed to process each image using the MATLAB Image Processing Toolbox™. The code processed each image as a 2-dimensional array with each element of the array representing the grayscale intensity that each pixel recorded. The code extracted the measured grayscale intensity values within the 100-pixel square region (10 000 pixels) and averaged them. The images and their respective averaged grayscale intensities can be seen in Appendix D. The 16-bit photo response curve is shown in Figure 4-3.

The image sensor of the canon EOS 1200D exhibits linear behavior up to a grayscale intensity of 41857, which is 63.8 % of the image sensor's full-well capacity. In other words, measured values above 41857 no longer follow a linear regression and therefore cannot be used to characterise solar flux. The data points for the linear regression curve with 95 % confidence level has a variance of 99.91 %. The value of the *y*-intercept of the linear regression curve only accounts for 0.25 % of the overall 16-bit depth and was insignificant. These results indicated

that measured grayscale values of solar radiation reflected off the Lambertian target must therefore be held under 41857 to maintain linearity.

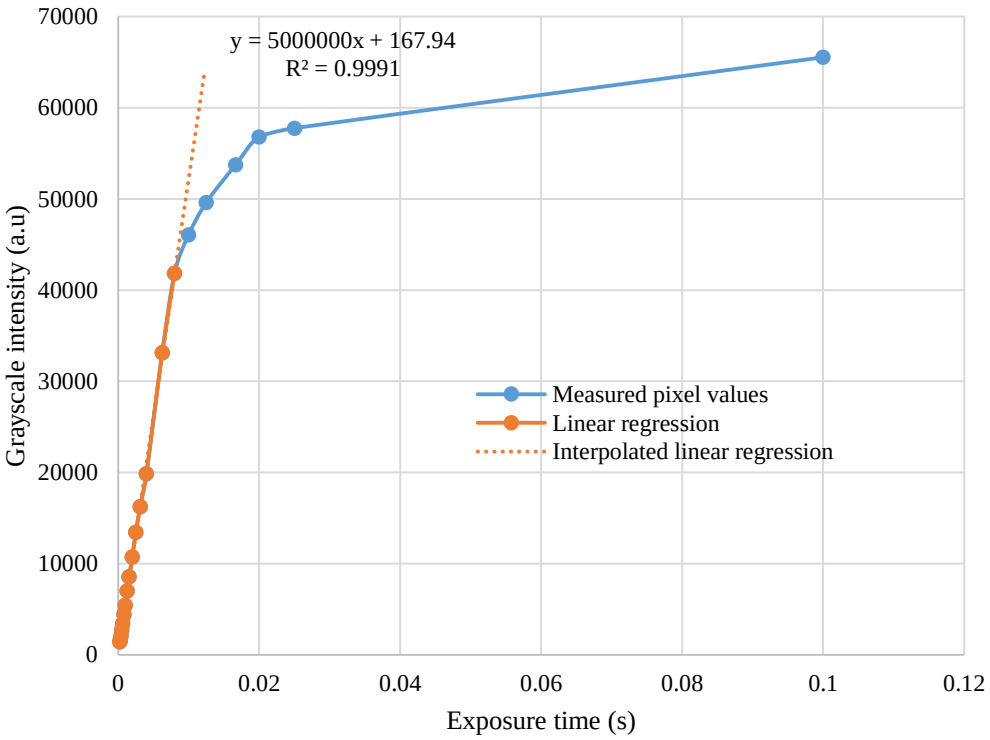

Figure 4-3: Measured pixel values vs exposure indicating the logarithmic and linear photo response of the CMOS image sensor

4.2. Image sensor light intensity attenuation

Consumer grade cameras are generally designed for ambient lighting conditions and exposure to concentrated solar radiation will saturate the sensor pixels. As discussed in Chapter 2, the estimated maximum intensity of concentrated solar radiation at the focal plane is approximately 1.4 MW/m^2 (1400 suns concentration).

Even though the camera shutter speed and aperture can be adjusted to attenuate the amount of light that reaches the image sensor, it is insufficient for these lighting conditions. To further restrict the amount of light that reaches the camera sensor, a neutral density filter was used. Neutral density filters attenuate light equally over the visible light portion of the solar spectrum through absorption. The transmittance of a neutral density filter depends on the optical density of the filter. For a given optical density (OD), the required transmittance (T) was calculated with Equation (4.2).

$$T = 10^{-OD} \tag{4.2}$$

The number of generated electrons per impinging photons is a function of the image sensor's quantum efficiency:

$$\mu_e = (QE)\mu_p \tag{4.3}$$

The full-well capacity (i.e number of available electrons) and average quantum efficiency for the Canon EOS 1200D camera are approximately 23104 e- and 37% respectively, provided by the image sensor manufacturer (Rhem., 2015). The expression for generated pixel electrons is given in Equation (4.4).

$$\mu_e = \frac{T(QE)A_T E_{pixel}\lambda}{hc} \tag{4.4}$$

As discussed in Chapter 3, the pixel irradiance (E_{pixel}) is dependent on the camera iris area and the square of the distance between the camera and focal plane. The proposed setup for the solar flux characterisation system is shown in Figure 4-4.

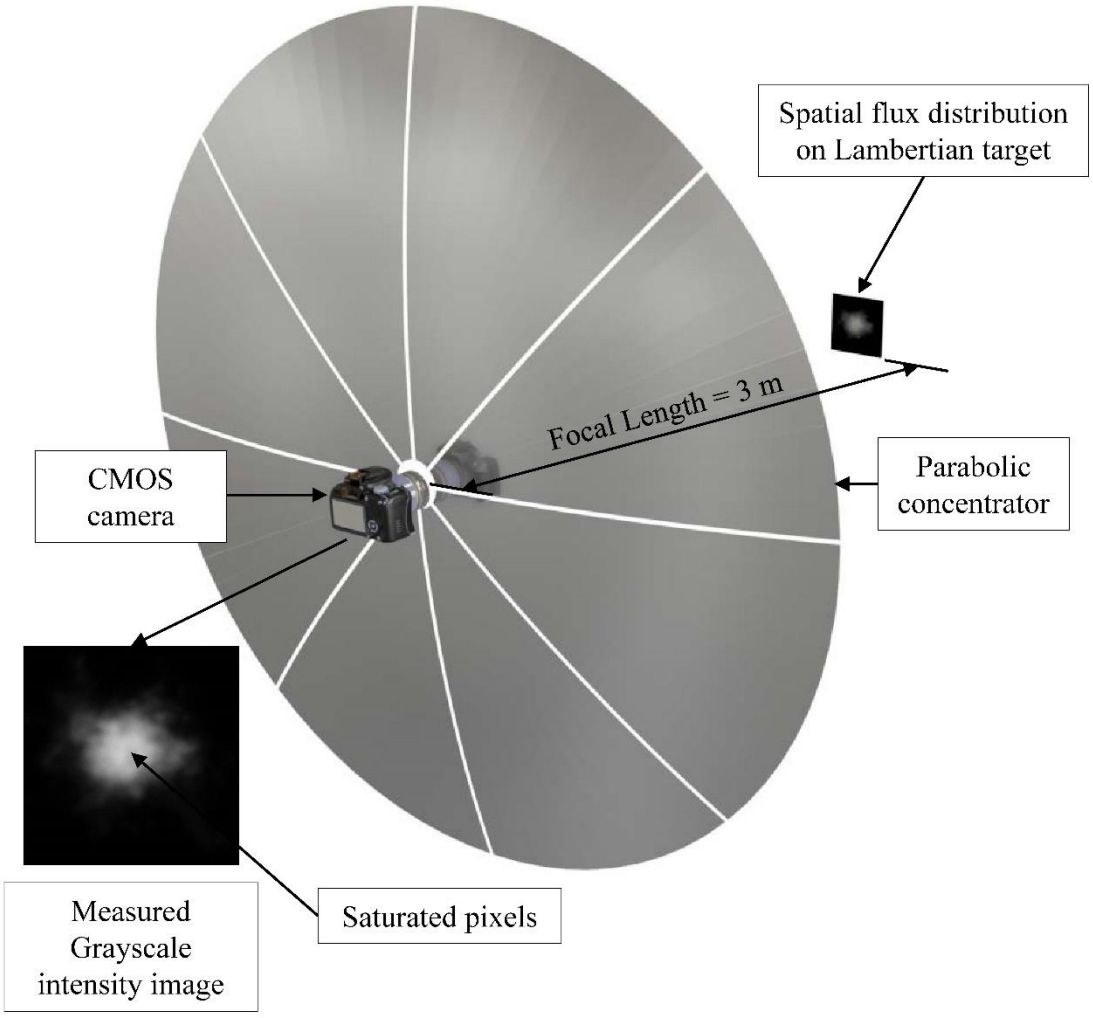

Figure 4-4: Indirect spatial flux mapping system setup

The exposure time (shutter speed) and aperture values were selected to account for greater intensities at the focal plane. Measurements acquired by the CMOS camera must fall within

the camera's linear photo response region. Therefore, a factor of 0.6 was also applied to account for the logarithmic response that occurs above 60% of the image sensor's full-well capacity. Solving for the required filter transmittance (T) in Equation (4.4) indicated a required transmittance of 0.0158 % to prevent pixel saturation. This corresponds to a filter optical density of 3.8. A Midopt™ ND400 absorptive neutral density filter was selected for this application. The filter has an optical density of 4.0 which correlates to a 0.01 % transmittance. The combination of shutter speed, aperture and filter ensured that the maximum attainable grayscale intensity under peak exposure was under 60 % of the full bit-depth of the camera (Figure 4-5).

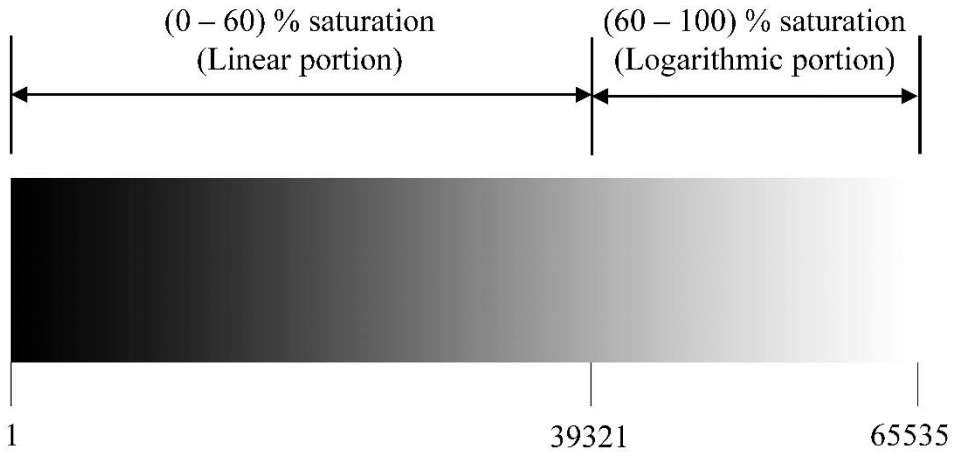

Figure 4-5: Allowable grayscale intensity measurement range for the Canon EOS 1200D CMOS camera

4.3 Image size minimisation process

Geometric flaws, surface waviness and misalignment of the system optical components contribute to the spreading of light at the focal plane of the solar furnace. These are generally classified as surface slope, non-specular surface reflection and receiver alignment errors (Shuai et al., 2008). The factors that influence these errors in reality are generally random and difficult to quantify. The cumulative effect of these errors enlarges the focal spot and reduces the overall optical performance of the system. Furthermore, the parabolic profile of the primary concentrator may deviate appreciably from design specifications, resulting in a shift of the dish's focal length. A qualitative method for determining the optimised focal spot position was devised. In this procedure, the concentrated radiative output of the parabolic concentrator was intercepted by a moving Lambertian target. Multiple images of intercepted solar flux were simultaneously recorded with the CMOS camera.

An optimised focal spot is considered to be the smallest possible area at which the reflected rays from the parabolic dish converge. The TPS longitudinal axis (z-axis) translational control

algorithm was used to move the water-cooled Lambertian target along the *z*-axis. The linear actuator was initially set to half its maximum stroke length (150 mm). The distance between the water-cooled Lambertian target surface and the parabolic dish was then set to 3 m (designed focal length of the parabolic dish). This set the Lambertian target in a neutral position where the theoretical focal plane is located. From this point, the linear actuator was extended to its maximum stroke length (150 mm from the neutral position). The target positioning process is illustrated in Figure 4-6.

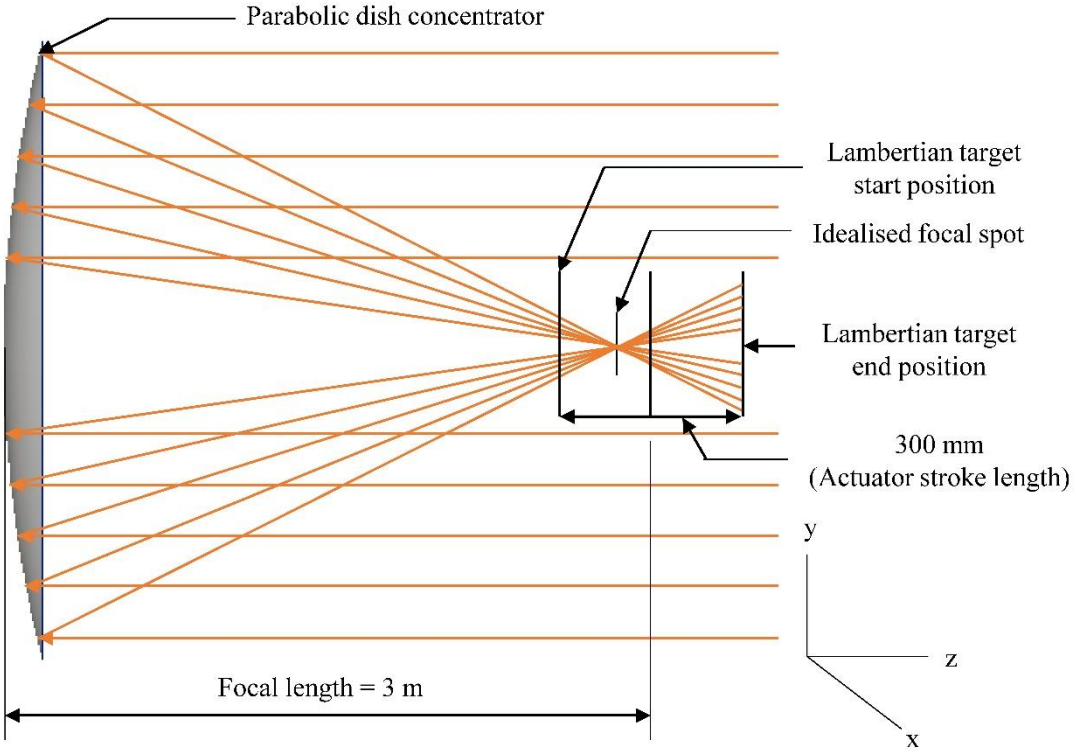

Figure 4-6: Schematic of the focal plane optimisation procedure

The linear actuator moves at constant speed making it possible to correlate the displacement of the linear actuator with time. The speed of the actuator was calculated to be approximately 11.5 mm/s. The continuous shooting mode feature of the CMOS camera was enabled to acquire images in equal time intervals. The neutral density filter was mounted onto the CMOS camera to prevent pixel saturation. A total of 66 images were captured during this test. The maximum grayscale values measured in each image were evaluated using a MATLAB™ code. The area on the Lambertian target that each pixel views changes as the distance between the target and camera is altered. For this reason, the focal spot size of each picture was not be determined. Further assessment of the images showed a visual change in the light distribution across the Lambertian target as it moved. The criteria for establishing which image represented the optimised focal point were highest attainable grayscale intensity and qualitative inspection

of the approximate focal spot size. Figure 4-7 illustrates the change in focal spot size with displacement and the results are given in Table 4-2.

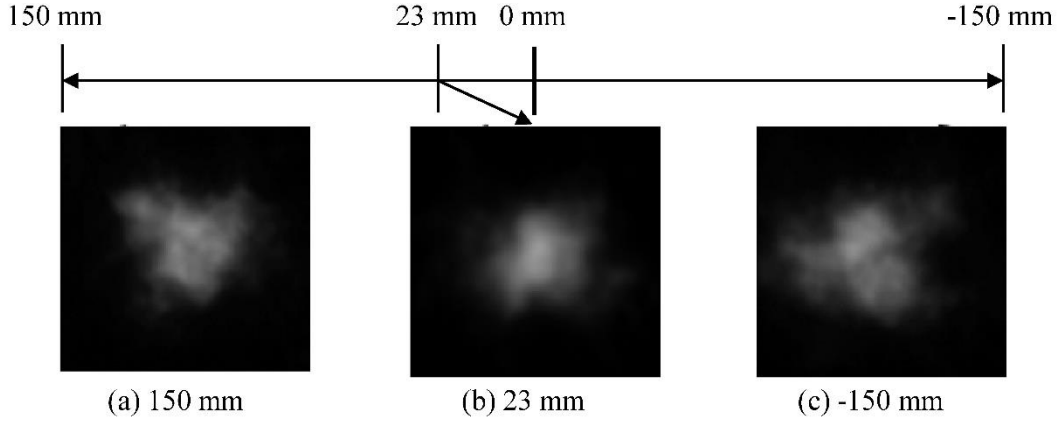

Figure 4-7: Qualitative comparison of the radiative energy distribution intercepted by the moving Lambertian target

Table 4-2: Maximum recorded grayscale intensity for the acquired images

Image quality results		
Image	Maximum grayscale intensity	% from saturation
(a) 150 mm	26598	40.59 %
(b) 23 mm	39657	60.51 %
(c) -150 mm	25124	38.33 %

Since the actual focal spot size was not determined, the images were evaluated qualitatively. There was an evident change in focal spot size as the Lambertian target travelled from its 150 mm offset position to its neutral position. The results indicated that the optimal location for the focal plane was 23 mm from the neutral position. The position of the longitudinal axis linear actuator was fixed for subsequent tests.

4.4 Calibration methods

The pixel intensity data of the grayscale intensity images captured by the CMOS camera require certain modification before they can be converted into spatial solar flux maps. These modifications include scaling the size of each pixel in relation to the physical size of the region (A_T) it observes on the Lambertian target (Figure 3-8).

Furthermore, a scaling factor must be applied to each grayscale pixel intensity to represent radiative solar flux. This is achieved by comparing the grayscale pixel intensities with a direct radiative flux measurement. In this study, a circular foil Gardon gauge was used to calibrate the intensity of the system.

4.4.1 Spatial correction

When performing spatial flux measurements, only the pixels that photograph the Lambertian target must be considered. For this system setup, the size of the target relative to the camera's field of view was noticeably small (Figure 4-8).

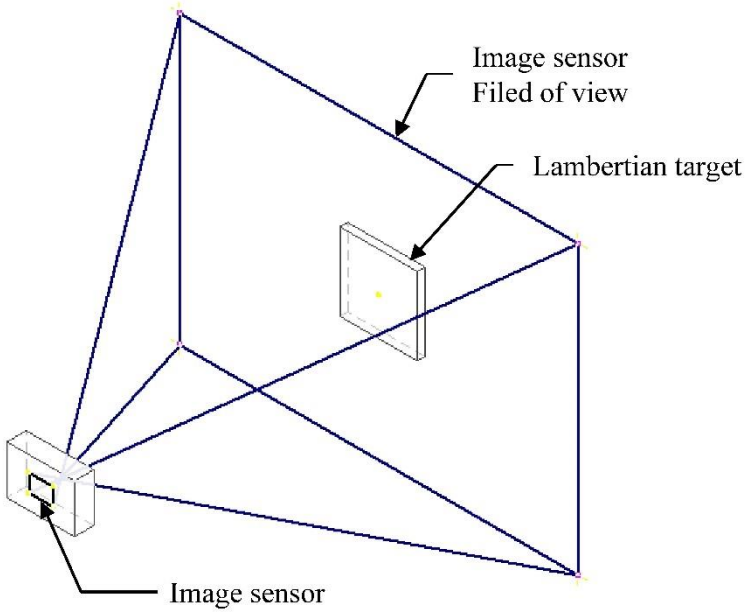

Figure 4-8: Image sensor field of view at the focal plane

This made it necessary to crop out the image data surrounding the target. By applying a region of interest (ROI) to an image, the image data can be constrained depending on the required operation. An ROI is a specification structure, defined by an arbitrary shaped region within an image. An ROI does not alter the pixel intensity data, but rather rebuilds the image according to the defined spatial constraints. A system calibration GUI was designed within LabVIEW™ to setup and run calibration procedures. Two methods were used for generating an ROI. The user can either specify a square ROI drawn in reference to an image's midpoint spatial co-ordinates or a rectangle ROI can be manually drawn on the image to extract the pixel data within that region. A detailed description for manually defining the system ROI is given in Appendix E.

Before measurements of the focal plane are acquired, the area that each pixel detects must first be translated into physical units. This was achieved by placing a two-dimensional artificial circular object with a known diameter within the same measuring plane as the Lambertian target. A circle was chosen for this procedure since its diameter is independent of its

orientation relative to the camera. The accuracy of obtaining a meter-per-pixel conversion factor is related to the size of the object and the distance at which it is viewed (Bailey, 1995). It was therefore decided to use a circle with a diameter of 60 mm printed on to a white sheet of paper to calculate this conversion factor. The circle was printed with black ink to achieve a good contrast between the circle and white sheet of paper. The circle was attached to the front face of the Lambertian target. With the CMOS camera lens zoom held constant, an image of the spatial calibration circle was acquired. An ROI was selected such that only the circle and small portion of the surrounding printed page were visible (Figure 4-9).

Figure 4-9: Image of the cropped spatial calibration circle used for pixel scaling

An image thresholding algorithm was developed to isolate the pixels occupying the area of the calibration circle. Thresholding is an image processing technique that compresses the grayscale pixel intensities outside a given range (Relf, 2004). Consider the image pixel data illustrated in Figure 4-10. The pixel intensities within the range of 0 to 17 represent light scattered off an absorptive surface. Pixel intensities outside that range represent light scattered from a diffuse-reflective surface. Performing a binary threshold operation on the image to the left suppresses the intensities outside the given range to zero, while setting the pixels whose intensities fall within the specified range to one, yielding the binary image to the right.

Furthermore, the resulting binary image was processed using a Danielsson distance mapping algorithm to find the centre spatial co-ordinates and pixel radius of circles within a binary image (Relf, 2004). The accuracy of the measurement was dependent on the resolution of the printer and quality of the ink used. Preliminary measurements revealed that the ink on the outline of the circle blended with the colour of the page, making it difficult to capture the true outer edge of the circle. This also made it difficult to determine if the selected threshold overestimated or underestimated the circle size. To rectify this, a second calibration circle was generated with a darker outline compared to the body fill colour of the circle. When the camera captured an image of the circle with the darker outline, the pixel intensities along the outline

of the circle become consistent with the body of the circle. Calculation of the circle pixel co-ordinates is illustrated in Figure 4-11.

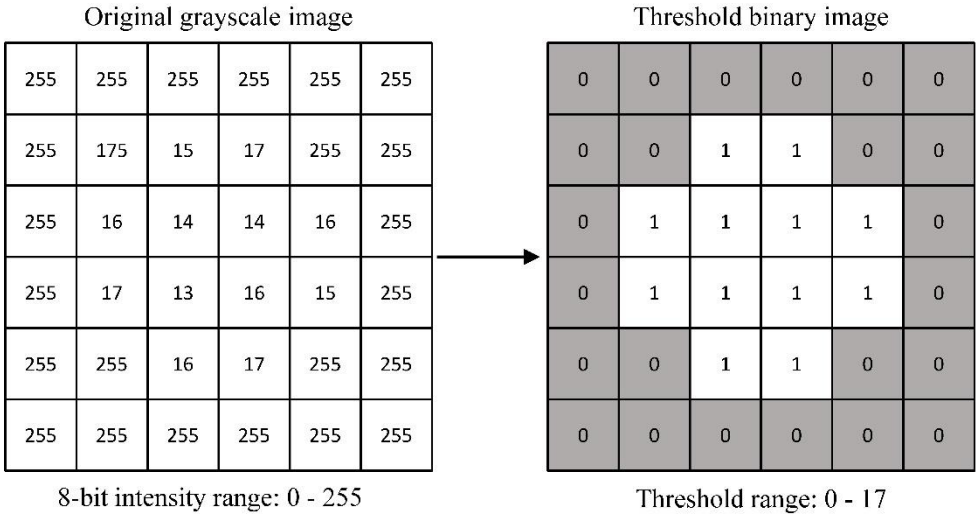

Figure 4-10: Image thresholding operation for an 8-bit grayscale image

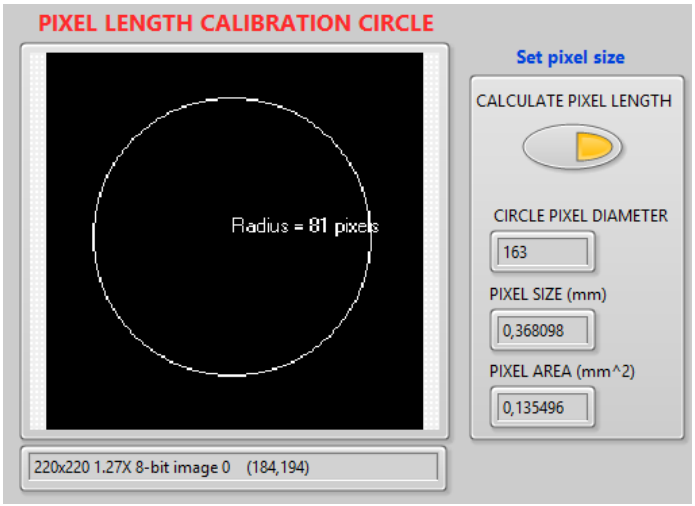

Figure 4-11: Binary image of the spatial correction circle in pixel co-ordinates and the associated physical dimensions that each pixel detects

The uncertainty of this process was evaluated by applying the same algorithm to multiple images of the spatial correction circle. These results indicated a ±1 pixel change in circle diameter calculations, corresponding to a pixel length size error 0.3680 mm ± 0.0043 mm. So long as the distance between the camera and Lambertian target surface and camera lens zoom remains constant, the calculated pixel length scale is valid for all measurements of spatial flux acquired at the measurement plane.

4.4.2 Circular foil Gardon gauge

The Gardon gauge sensor is a two-junction differential thermocouple that measures the temperature difference between the centre and the circumference of a thin circular disc. The circular foil disc is made of constantan, which is a copper-nickel alloy made up of 55% copper and 45% nickel, and is bonded to a water-cooled copper heat sink (Langley & Barnes, 2006). This combination of two dissimilar materials joined in series creates a differential thermocouple that outputs an EMF that is directly proportional to the temperature difference measured between the junction situated at centre and the perimeter of the circular foil disc respectively. Figure 4-12 shows a schematic of the Gardon gauge heat flux sensor.

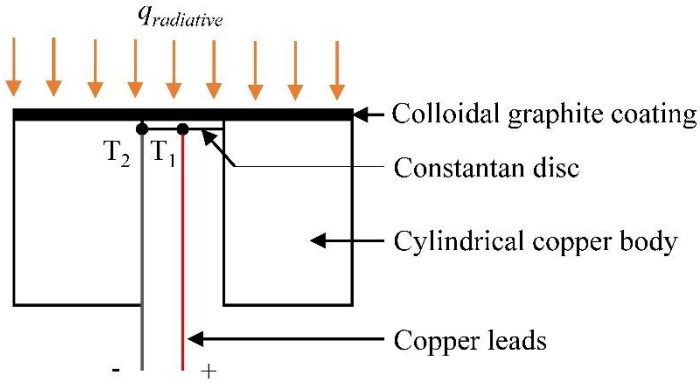

Figure 4-12: Schematic diagram of a circular-foil Gardon gauge heat flux sensor

The thermoelectric voltage produced is in the range of 0 – 10 mV regardless of the heat flux range. The procedure for calibrating the sensor involves inserting the commercially sold Gardon gauge and a reference gauge into opposite ends of a dual-cavity tube furnace. A graphite plate located at the end of the tube that irradiates symmetrically when an electrical current is passed through it. The tube is separated by an opaque divider, to allow its internal temperature to be measured by a National Institute of Standards and Technology (NIST) pyranometer. A graphite plate is positioned at one end of the tube and irradiates homogenously when an electrical current is passed through it. Once the temperature of the plate has stabilised, a reference gauge is inserted into the cavity until its sensing surface is very close to the graphite plate where its output is continuously recorded (Guillot et al., 2014).

The commercial sensor is then calibrated using the reference gauge by comparing their response when simultaneously exposed to the graphite plate. The range of radiative heat flux emitted from the plate is representative of the desired calibration range for the commercially sold sensor. The manufacturer reports a measurement uncertainty of up to ±3% with a repeatability of ±1% (Ballestrín, 2003). The exposed face of the sensor is sprayed with a high temperature resistant colloidal graphite coating. This creates a rough, matte black surface that increases absorption of solar radiation on the front face of the sensor.

4.4.3 Directional considerations

The directional distribution of solar flux incident on the absorbing surface of the Gardon gauge can alter the gauge's response. This is attributed by the directional dependence of the gauge's absorptive colloidal graphite coating. The directional reflectivity (ρ) of a coating is related to the directional absorptivity (α) by Equation (4.5).

$$\alpha = 1 - \rho \tag{4.5}$$

The directional dependency on the reflectivity of pyrolytic graphite and amorphous carbon materials is shown in Figure 4-13.

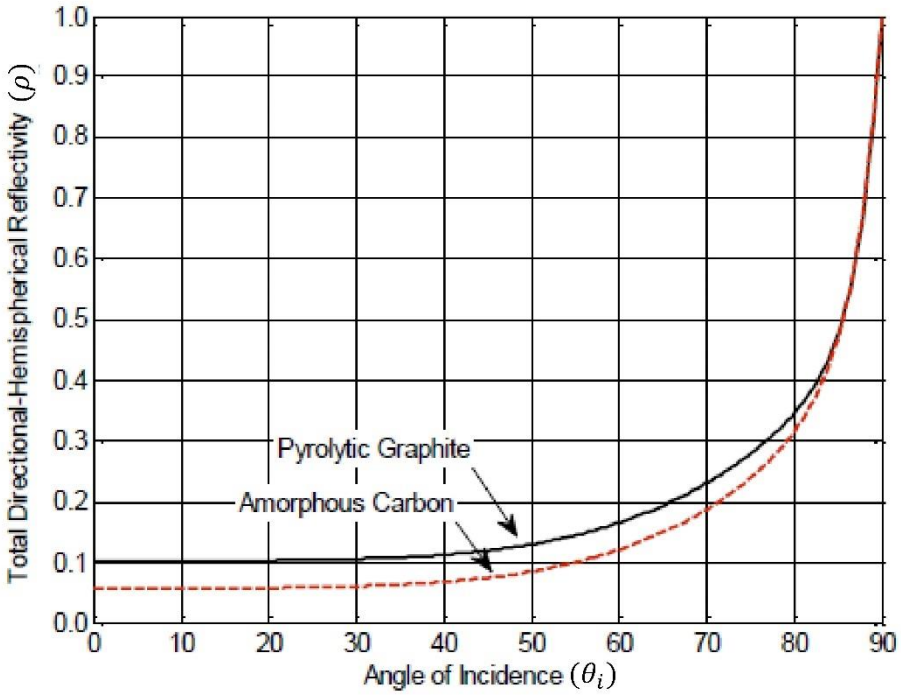

Figure 4-13: Total directional reflectivity vs angle of incidence for pyrolytic graphite and amorphous carbon materials (Krueger, 2012)

The parabolic concentrator used at the SERAFF facility was designed with a rim angle of 45°. Therefore, the direction at which reflected radiative solar flux strikes the Gardon gauge surface is at 45° or less. The change in directional reflectivity of the colloidal graphic coating is approximately 0.02 for incident angles from 0° to 45°. Therefore, the directional absorptivity dependence of the Gardon gauge is not considered significant here.

4.4.4 Pixel intensity calibration

Following the spatial correction procedure, the grayscale intensity pixel data measured by the CMOS camera is compared to measured values of solar flux obtained by the Gardon gauge. In this work, a TG1000-1 water-cooled Gardon gauge was purchased and calibrated by Vatell

Corporation™, with a readout range of 0 - 5.32 MW/m^2 for calibrating STIMS (Appendix F). According to the manufacturer's specifications, the sensor disc diameter is 2.0 mm with an overall body diameter of 25.3 mm. Figure 4-14 shows an image of the Gardon gauge purchased from Vatell Corporation™.

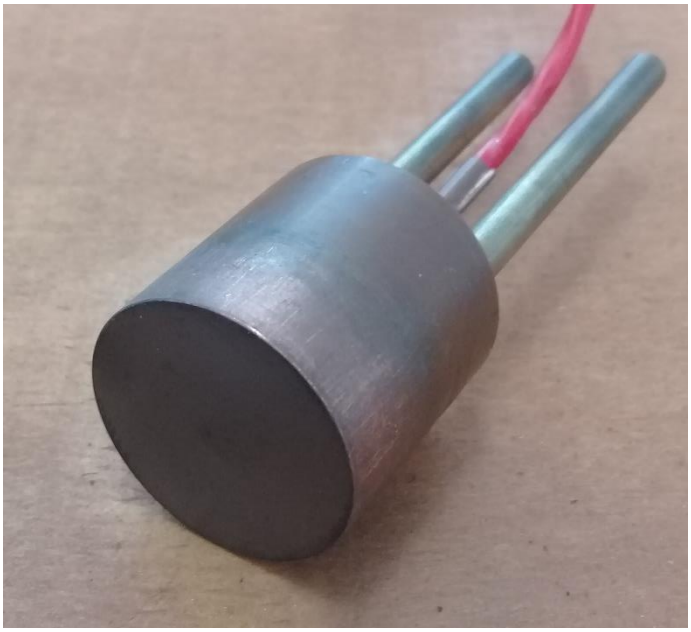

Figure 4-14: TG1000-1 water-cooled circular-foil Gardon gauge manufactured by Vatell Corporation™

In addition to the water-cooled Lambertian target, a smaller Lambertian target was designed to be used for the calibration and spatial flux measurement procedures. As before, an alumina plasma-spray coating was applied to a 12 mm thick (300 mm x 300 mm) aluminium substrate. The target was not used for applications that required prolonged exposure to the concentrated solar flux and so cooling the target during operation was deemed unnecessary.

To calibrate the CMOS camera to measure solar flux, the solar radiation measured by the camera's images sensor must be compared to the same intensity of solar radiation measured by the Gardon gauge. Conventional solar flux measurement systems embed the Gardon gauge into a hole positioned at the centre of the Lambertian target (Lee et al., 2014). However, the presence of the colloidal graphite surface coating of the Gardon gauge distorts the light scattered off the surface due to the high absorptivity of the coating. The brightness distribution off the Gardon gauge surface, viewed by the CMOS camera, would be of significantly lower magnitude compared to light scattered off a white diffuse surface. Therefore, a mounting fixture for the Gardon gauge was designed and fixed to the side of the smaller Lambertian target. The fixture was set such that the front face of the Lambertian target and Gardon gauge are coplanar.

To relate the grayscale values recorded by the CMOS camera to the solar flux intercepted by the Lambertian target, the solar flux is first measured by the Gardon gauge. The gauge readout is in response to the average radiative flux received over the sensor disc area (Ø2 mm). Therefore, the surrounding copper body must be neglected when mapping the Gardon-gauge sensor region in pixel co-ordinates. A 2 mm thick plate was fabricated with a hole matching the position and diameter of the Gardon gauge sensor disc. The plate was coated with a matte white paint to diffuse-reflect ambient light that strikes the surface. Initially, the Gardon gauge was positioned behind the plate so that the dark colloidal graphite coating is exposed when viewed from the front. The front face of the plate was aligned with the Lambertian target so that the two surfaces were flush (Figure 4-15).

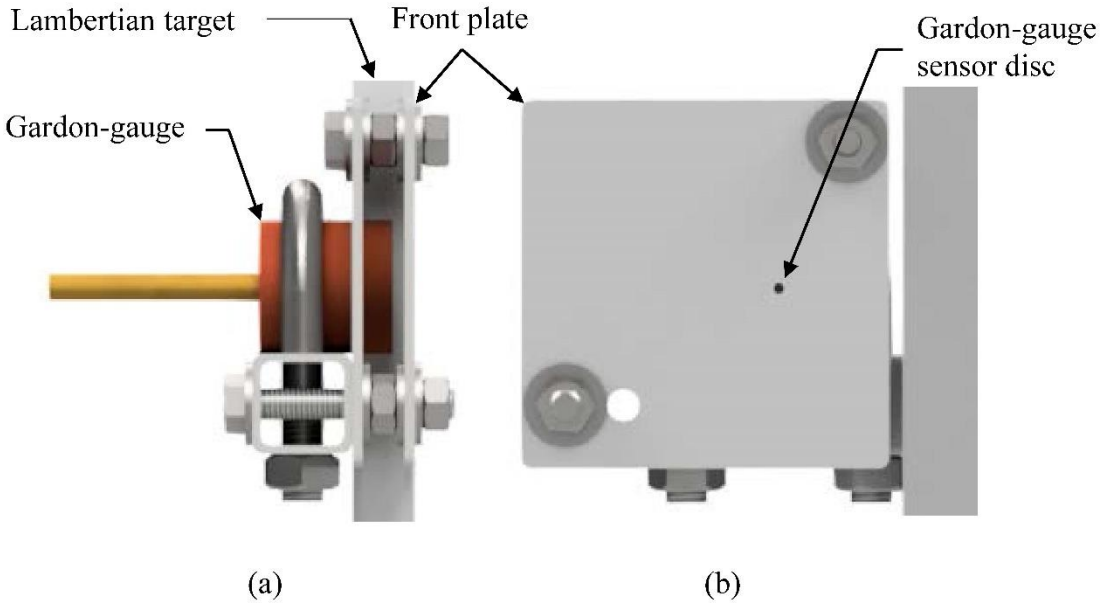

Figure 4-15: Side view of the Gardon gauge mounting fixture (a) and front view (b)

When photographed by the CMOS camera, the pixel grayscale intensities measured at the sensor disc region are of significantly lower magnitude compared to the pixels of the surrounding matte white surface. This made it possible to locate the pixel co-ordinates of the sensor influencing region.

In an ideal calibration environment, the distribution of solar flux across the sensor disc should be relatively uniform to ensure that the response of the gauge is truly representative of the radiative flux it absorbs. However, the distributive nature of concentrated solar flux at the focal plane of a solar furnace system is approximately Gaussian in shape. The Gardon gauge was positioned towards the midpoint of the flux distribution where there are lower gradients in solar flux density to mitigate this error.

Additional controls were added to the ROI front panel of the LabVIEW^{TM} application to assist with positioning the Gardon gauge near the point of peak concentration. The camera was equipped with the neutral density filter with the shutter speed and aperture set to 1/500 s and f5.6 respectively. These settings were selected to prevent pixel measurements from falling into the CMOS camera's logarithmic photo response region, which was above 60 % of the camera's saturation capacity.

With the parabolic concentrator illuminated by the heliostat and the Lambertian target situated at the focal plane, an image of the spatial solar flux distribution was acquired. The image was scanned to find the pixels that measured the highest grayscale intensity. Assuming the nature of distributed solar flux at the focal plane is Gaussian, it follows that the flux distribution surrounding the point of maximum intensity is relatively uniform. With the neutral density filter removed from the camera lens, the Gardon gauge was moved towards the point where the maximum intensity was previously recorded. An ROI was constructed to create a sub-image that only includes the pixel data of the Gardon gauge sensor disc and a small portion of the surrounding matte white surface (Figure 4-16).

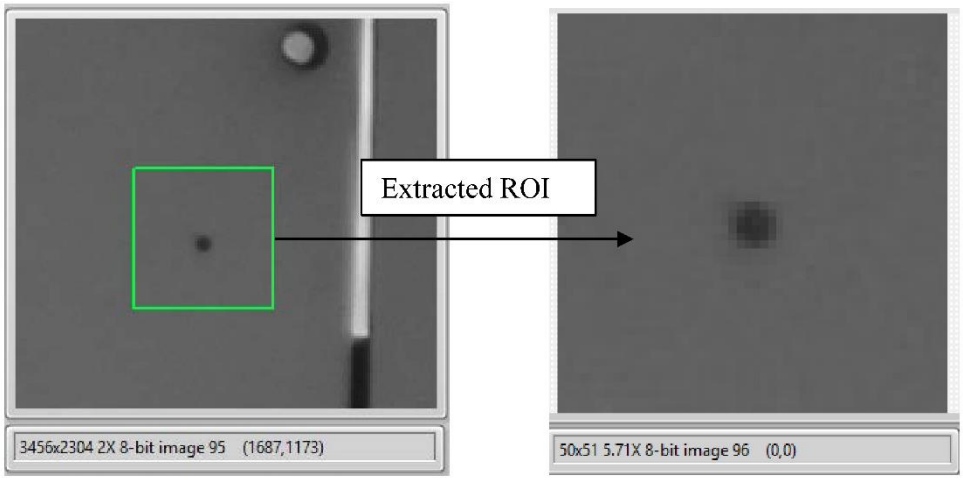

Figure 4-16: Manually defined rectangular ROI of the Gardon gauge sensor region (a) and the extracted ROI displayed in LabVIEW (b)

Utilising the same threshold and Danielsson distance mapping algorithm employed in the spatial correction procedure, the area occupied by the Gardon gauge sensor was mapped in pixel co-ordinates (Figure 4-17).

The fine spatial resolution of the camera identified 21 pixels within a circular pattern that occupied the sensor disc region. However, the pixel area of the sensor disc underestimated the actual area by 9 %. To reduce this error, a square area approximation was used, which included

half-pixels at the corners of the circular sensor region. The overall area underestimation of the Gardon gauge in pixels was reduced to 0.8% using this method (Figure 4-18).

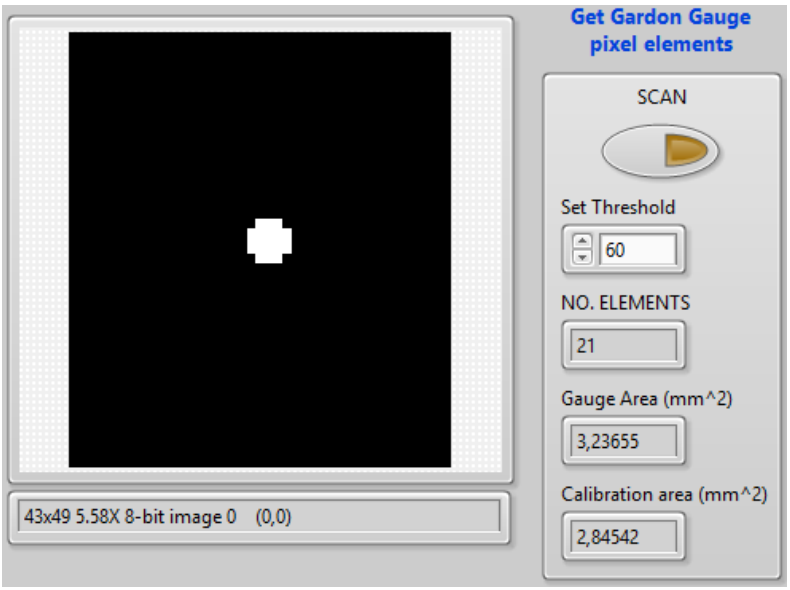

Figure 4-17: Gardon gauge influencing region defined in pixel co-ordinates

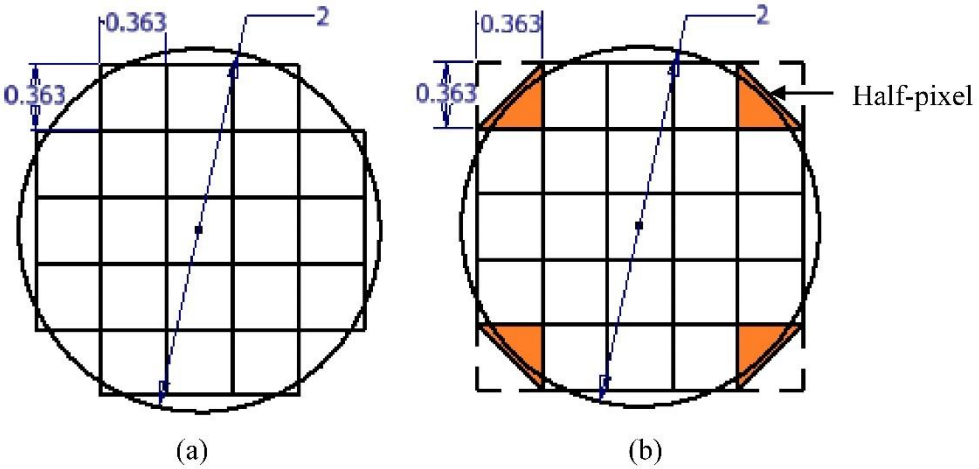

Figure 4-18: Error encountered by the Gardon gauge sensor approximation method (a) and error reduction by including the half-pixel intensity at the corners of the circular area approximation

Solar flux measurements from the Gardon gauge were acquired with a NI-9211 thermocouple module. The sensitivity of the module is 0.008 mV, which corresponds to a sensor output of 4.25 kW/m^2. Data from the Gardon gauge were logged to a PC using a LabVIEW^{TM} code. After spatially mapping the Gardon gauge sensor in pixel co-ordinates, the Gardon gauge was brought forward, such that the front face of the gauge and Lambertian target surface were coplanar. With the solar furnace active, 6 samples of solar flux absorbed by the Gardon gauge were recorded at a rate of 3 Hz. The construction of a circular-foil makes the sensor's calibration independent of the temperature of the cooling water and therefore readings were

acquired immediately after the Gardon gauge was exposed (Vatell, 2011). After a brief delay, the Lambertian target was moved to replace the location of the Gardon gauge and diffusely-reflect the radiative solar radiation towards the CMOS camera.

The grayscale intensity values at the pixels according to the i^{th} and j^{th}spatial co-ordinates of the Gardon gauge influencing region were averaged to calculate the grayscale intensity factor (Φ_{GV}), as given in Equation (4.6).

$$\Phi_{GV} = \frac{\sum_{i,j}^{n,m} GV_{i,j}}{N} \tag{4.6}$$

Differences between the spectral composition of sunlight and the black body radiation used to calibrate the Gardon gauge influence the sensor's response. The absorption coefficient of the Gardon gauge's colloidal graphite coating is not constant over the entire spectral range. Ballestrín et al. (2003) demonstrated that if a Gardon gauge was used to measure concentrated solar flux, the colloidal graphite coating could overestimate the measurement by 27.9%. This is due to the spectral mismatch between the spectral composition of sunlight and the radiative flux emitted by the electrically heated graphite plate used to calibrate the Gardon gauge.

This procedure was repeated at different times during cloudless days to vary the intensity of concentrated solar flux at the focal plane. The camera's position relative to the Lambertian target was kept fixed for each calibration iteration. The averaged grayscale intensity values measured by the CMOS camera were plotted against their respective solar flux readings, measured by the Gardon gauge. Figure 4-19 shows the linear regression curve for the CMOS camera grayscale calibration.

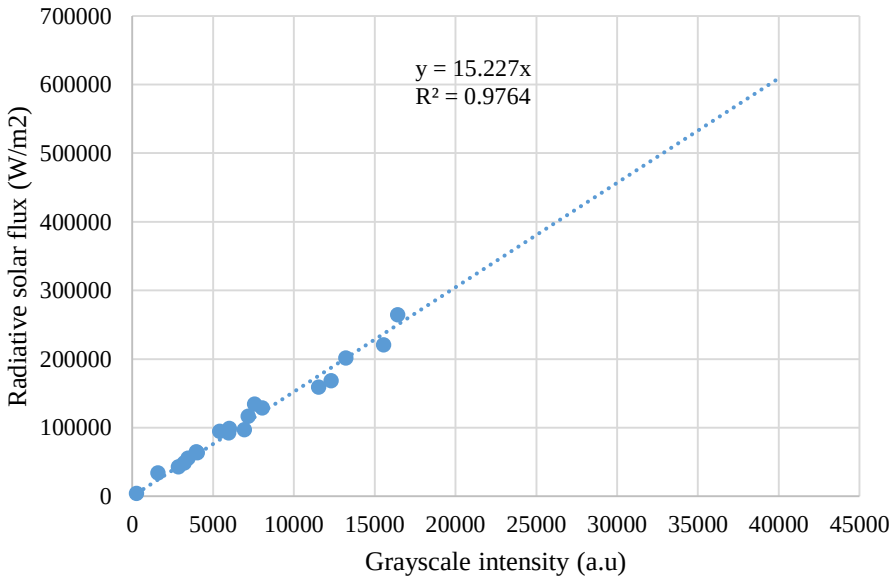

Figure 4-19: Relationship between the radiative solar flux measured by the Gardon gauge and the corresponding pixel grayscale intensity obtained experimentally

The camera's shutter speed and aperture were set so that the maximum grayscale intensity measured during calibration was approximately 50 % of the CMOS camera's linear photo response range (Figure 4-3). This was to account for days when SERAFF's thermal energy output is considerably higher due to an increase in DNI, which is influenced by time, date and weather-related factors. Additionally, geometric factors such as enlarging the active surface area of SERAFF's heliostat and recalibration of the parabolic concentrator's petal array can also increase SERAFF's overall energy output. Therefore, the indirect flux mapping system was calibrated to allow for higher solar flux intensities to be measured. The line of best fit through the data points showed a linear relationship between measurements acquired with the Gardon gauge and the grayscale pixel values measured by the CMOS. The curve shown in Figure 4-19 indicated that measured pixel grayscale intensities must be scaled by a factor of 15.227 to be representative of solar flux.

Ulmer et al. (2004) suggested that a spectral mismatch correction factor (F_s) of 0.782 must be applied to all measurements obtained by the Gardon gauge when measuring solar flux. This factor also considers the hemispherical absorptivity of the colloidal graphite coating. The grayscale calibration factor (F_c) was calculated using Equation (4.7).

$$F_c = 15.227F_s \tag{4.7}$$

This constant is valid for grayscale values that are under 60 % of the camera's saturation capacity ($0 \leq GV \leq 39321$) as discussed earlier in this chapter. By applying equation 4.7 to this range of grayscale intensities, the solar flux measureable by the CMOS camera ranges from 0 kW/m^2 to 468.19 kW/m^2.

Difficulties in positioning the Gardon gauge within the point of peak concentration limited the range of intensities that could be measured. The intensity of light reflected off the Lambertian target decreases with the square distance between the camera and the target. Therefore, if the distance between the camera and target is altered, the camera must be recalibrated.

The spectral composition of sunlight is not constant and changes due to the prevailing airmass (AM) and under certain atmospheric conditions. These conditions are time, weather and season dependant making it difficult to quantify the impact they have on the spectral composition of sunlight. The magnitude and nature of these conditions are likely to cause minimal change to the optical systems calibration. However, measurements of solar flux obtained by the Gardon gauge should be frequently compared to the pixel grayscale intensity to identify any deviations from previously recorded results. If significant changes are identified, the pixel intensity calibration procedure must be repeated. Degradation of the Lambertian target and colloidal

graphite surface coating of the Gardon gauge must also be considered and should be periodically recalibrated.

Chapter 5 SERAFF measured performance

5.1 SERAFF target irradiance mapping system (STIMS)

Spatial flux measurements of the SERAFF focal spot image were carried out using the calibrated CMOS camera. Images of the concentrated radiative flux reflected off the Lambertian target were processed as two-dimensional numerical arrays, with each element in the array representing the grayscale intensity recorded by each pixel. The calibration factor is applied to each element in the array so that the measured non-dimensional grayscale intensity data is representative of solar flux. Figure 5-1 illustrates the procedure for generating the spatial flux maps.

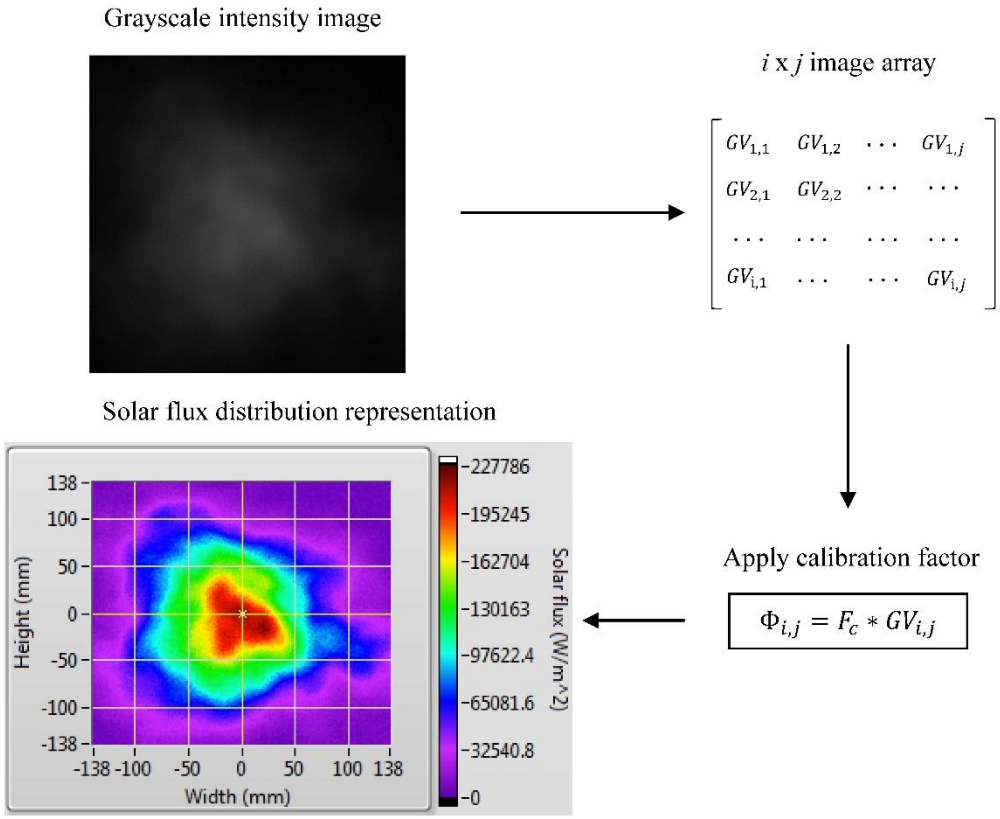

Figure 5-1: Conversion from grayscale intensity image to calibrated spatial solar flux map

Measurements of the spatial flux provide other useful performance metrics. These include thermal power output (Q_{tot}), minimum and maximum solar flux, blackbody stagnation temperature (σ_b) and optical efficiency (η_{opt}). The 300 mm x 300 mm Lambertian target was used to intercept the concentrated solar radiation at the focal plane of the parabolic dish. The diffuse-reflected rays are measured by the Canon EOS 1200D CMOS camera to capture the spatial solar flux distribution at the focal plane. To prevent image perspective distortion, the camera was positioned so that the angle between the Lambertian target surface normal and

central axis of the camera was zero. SERAFF's optical and measurement components are shown in Figure 5-2.

(a)

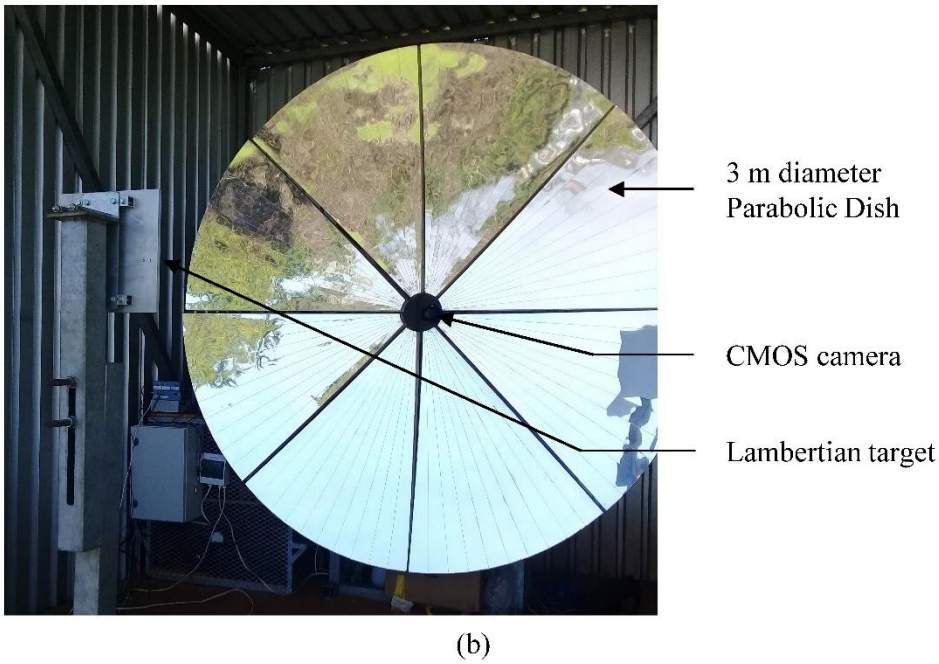

(b)

Figure 5-2: 9 m^2 non-focusing heliostat (a) and the 3 m diameter parabolic dish with the spatial flux measurement components (b)

For the intensity calibration factor mentioned in Chapter 4 to be valid for all flux measurements, the camera shutter speed and aperture were set to 1/500 s and f5.6, respectively. The neutral density filter was mounted on to the camera lens for all measurements. Removal of the neutral density filter or changes to the camera shutter speed and aperture alter the

intensity of light that impinges the image sensor, thus rendering the intensity calibration factor invalid.

5.2 Spatial flux characterisation

The temporal variation in the sun's position and DNI relative to a fixed point on the earth's surface influences the thermal energy output of a solar furnace. SERAFF's concentrated radiative energy output was measured hourly on 24 October 2018, starting from 9:00 am up to and including 15:00 pm, which is the typical operational window for the solar furnace. Spatial flux measurements were acquired under clear-sky conditions to maximise the thermal energy output of the solar furnace.

ROI controls were used to constrain the flux measurements to a large portion of the Lambertian target. A 750 pixel-square ROI was used, which corresponds to a 276 mm x 276 mm square area of the focal plane. Before each measurement was made, an image of the target was obtained in the absence of concentrated solar flux and subtracted by the spatial flux measurements to account for ambient light. The hourly-measured spatial flux maps recorded from 9:00 am to 15:00 pm are shown in Figure 5-3.

After applying the calibration factor (F_c) to each element in the image two-dimensional array, the total thermal power incident on the measurement plane was determined using Equation (5.1).

$$Q_{tot} = \sum_{i=1,j=1}^{N} \Phi_{i,j} A_T \tag{5.1}$$

where i and j are the row and column co-ordinates of the image array respectively, $\Phi_{i,j}$ is the measured solar flux at each i^{th} and j^{th} pixel co-ordinate and A_T is the elemental area of the Lambertian target that each pixel detects. The average flux density ($\bar{q}$) across the measurement plane was determined using Equation (5.2).

$$\bar{q} = Q_{tot} \Big/ \sum_{i=1,j=1}^{N} A_T \tag{5.2}$$

The blackbody stagnation temperature (T_s), which is the highest temperature (in ºC) that a blackbody receiver with dimensions matching the measurement region would reach, with no input losses and ignoring ambient temperature was calculated with Equation (5.3).

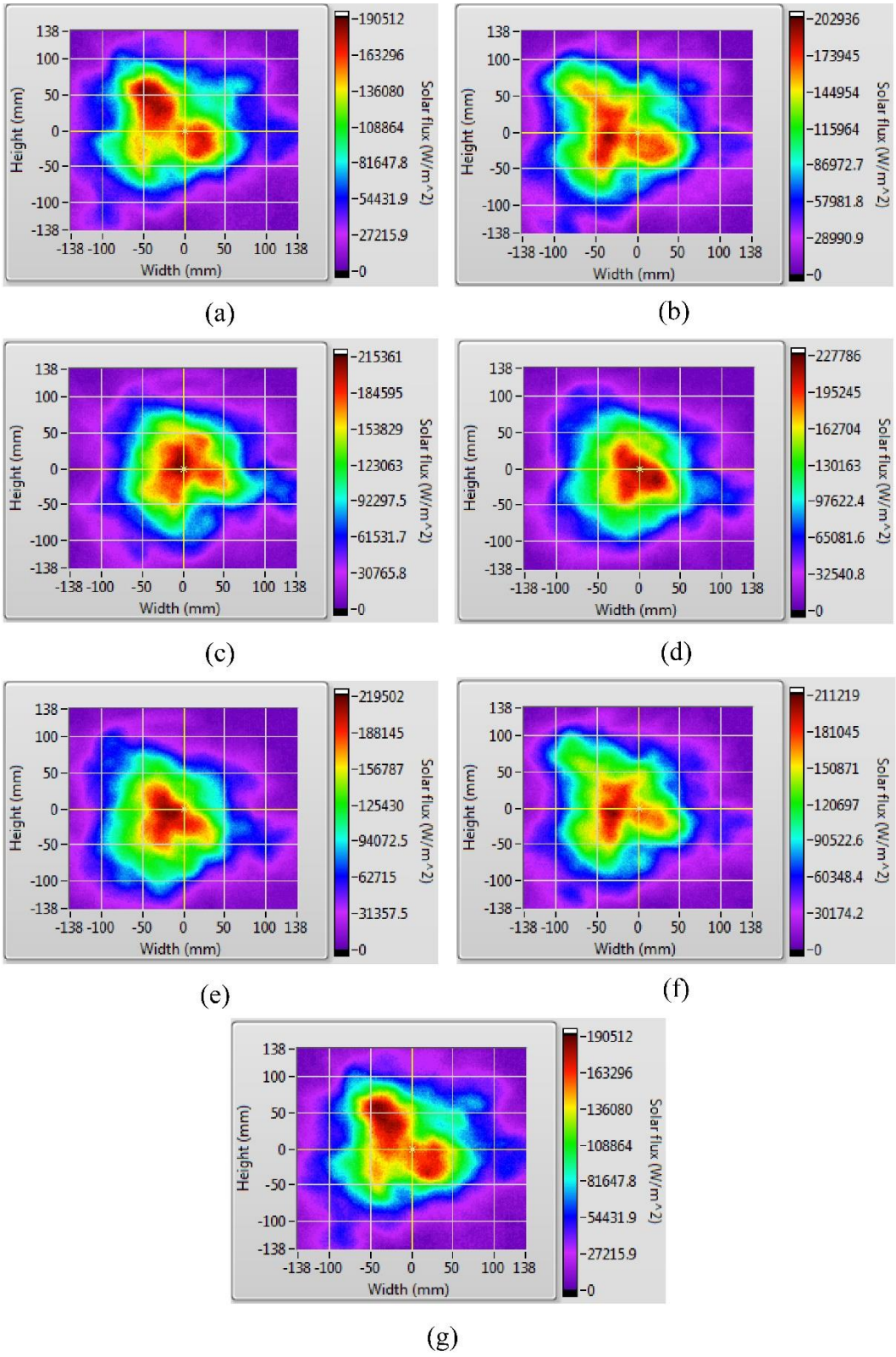

Figure 5-3: Measured spatial flux maps acquired at (a) 9:00 am (b) 10:00 am (c), 11:00 am (d), 12:00 pm (e), 13:00 pm (f), 14:00 pm and (g) 15:00 pm over a square region of 276 mm x 276 mm on 24 October 2018

$$T_s = (\bar{q}/\sigma_B)^{0.25} - 273.15 \quad (5.3)$$

Here, σ_B is the Steffen Boltzmann constant (5.67 x 10^{-8} W/m^{2}K^4). The optical efficiency (η_{opt}), which is defined as the ratio of radiative power generated at the focal plane over the cumulative radiative energy input (q_{DNI}) collected across the heliostat surface (A_H), was calculated with Equation (5.4).

$$\eta_{opt} = \frac{Q_{tot}}{q_{DNI} A_H} \quad (5.4)$$

The seven measurements indicated a peak flux range of 190.5 kW/m^2 – 227.8 kW/m^2, located towards the centre of the measurement plane. Each measurement had a unique distribution profile that was dependent on the time the measurement was acquired. As the sun moves along its trajectory, the zenith and azimuth angles relative to the heliostat change. Since the heliostat redirects sunrays towards a fixed point, the projected area of reflected sunrays changed as a function of time.

This means that the illuminated area of the parabolic concentrator was inconsistent throughout the day, resulting in a varying distribution at the focal plane in terms of spot size and intensity. Furthermore, the heliostat had to be adjusted manually to illuminate the parabolic concentrator due to problems with the automated tracking system. This meant that the angle reflected sunrays were offset from their intended path, but the degree to which this occurred is difficult to determine. This effect causes a drift in the focal spot and influences the quality of the concentrated solar radiation.

An additional factor to consider is the curvature inconsistency associated with the parabolic concentrator. As discussed in Chapter 3, the concentrator is divided into eight segments, with a translational and rotational adjustment mechanism installed at each segment. Since each segment is treated independently, the conformity of the overall dish to a true parabolic shape was compromised. This caused the reflected sunrays to converge at the focal plane in a random and unpredictable manner.

The distribution profile of the measurements was similar to that of a Gaussian distribution, centered towards the middle of the measurement plane. The symmetry of the distributions was evaluated qualitatively, through inspection of the spatial flux maps (Figure 5-3). Furthermore, one-dimensional plots using the pixel intensity data along the vertical and horizontal axis of the spatial flux data were compared. These plots were generated using the spatial *x* and *y* coordinates and their corresponding intensity. The *x*-*y* intensity plot for the spatial flux measurement acquired at 12:00 pm is shown in Figure 5-4. The one-dimensional plots for all the spatial flux measurements are provided in Appendix G.

Due to the asymmetrical nature of the measured spatial flux profiles, the *x-y* coordinates corresponding to the point of maximum measured intensity were different with each measurement. Therefore, the maximum solar flux values depicted in the one-dimensional plots may not be truly representative of the maximum measured solar flux incident on the measurement plane.

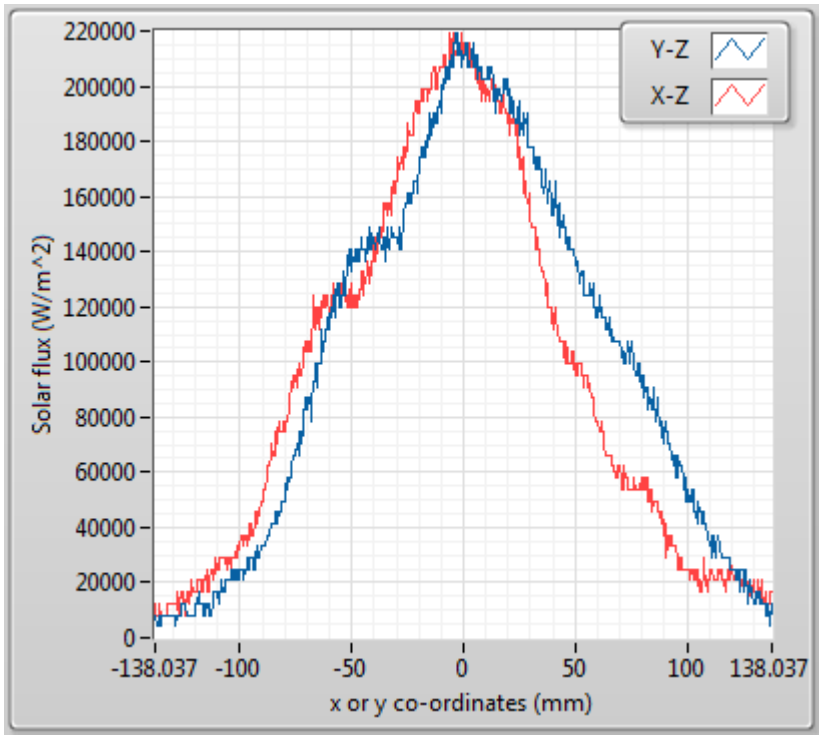

Figure 5-4: One-dimensional plot of the spatial x and y coordinates and their corresponding intensity for the spatial flux data acquired at 12:00 pm

Receivers used in solar furnace facilities are typically cylindrical in shape. Therefore, performance metrics were evaluated across the full measurement plane (that is the 276 mm x 276 mm square region) and within specified circular regions. Due to the asymmetrical nature of the measured spatial flux profiles, the *x* and *y* coordinates relating to the point of maximum measured intensity was different with each measurement. An image masking process was developed in LabVIEW™ to remove the pixel intensity data surrounding a defined circular region located at the centre of measurement plane (Figure 5-5).

By constraining the image data to a circular region, the energy density input for prototype cylindrical receivers being tested at SERAFF can be more accurately defined. The spatial flux data obtained at 12:00 pm was used to investigate how the thermal energy output of SERAFF is influenced by regional boundary constraints. Performance metrics for the full measurement plane and focal regions with diameters of Ø 150 mm, Ø 200 mm and Ø 250 mm were evaluated. These performance metrics are given in Table 5-1.

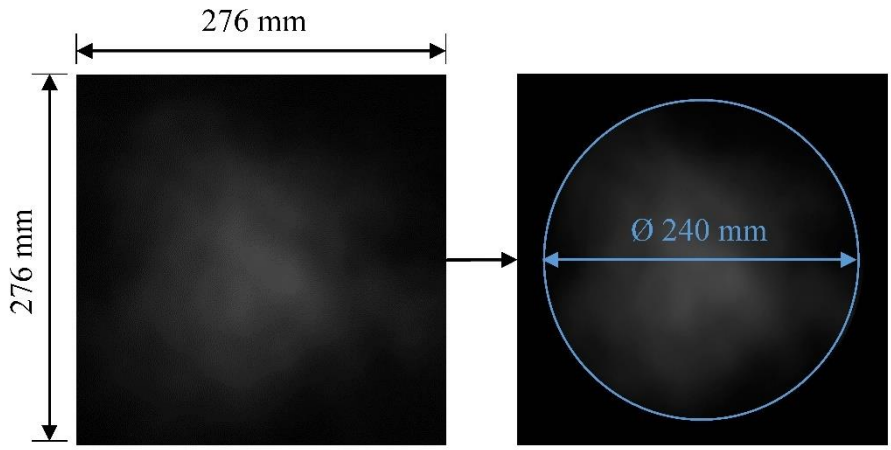

Figure 5-5: Grayscale image conversion to a masked grayscale image with a user defined diameter

Table 5-1: Performance metrics for the spatial flux data measured at 12:00 pm

Focal Region (mm)	**Solar flux range (kW/m^2)**	**Thermal power (kW)**	**Blackbody temperature (ºC)**	**Optical efficiency (%)**
Ø 150	45 - 227	2.36	965.68	28.78
Ø 200	12 - 227	3.24	886.67	39.51
Ø 250	4 - 227	3.83	808.89	46.70
276 x 276	0 - 227	4.22	720.72	51.50

The cumulative power at the focal plane increased with target diameter due to an increase in surface area for the solar radiation to intercept. This is an important factor to consider when designing receiver apertures for SERAFF. Figure 5-6 shows the change in cumulative power as a function of target diameter for the spatial flux distribution measured at 12:00 pm.

The concentration accuracy of a solar furnace is greatly influenced by optical errors, which include surface waviness, poor reflective surface quality, heliostat tracking errors and receiver misalignment. To estimate the errors associated with SERAFF's optical components, the spatial flux measurement obtained at solar noon (12:00 pm) was compared to normalised results acquired through Monte Carlo ray-tracing simulations. To replicate the optical components as they are in reality, a CAD model of the parabolic concentrator was generated for the purpose of acquiring a representative comparison of the measured results with the simulated results. Figure 5-7 illustrates the CAD model of the segmented parabolic concentrator.

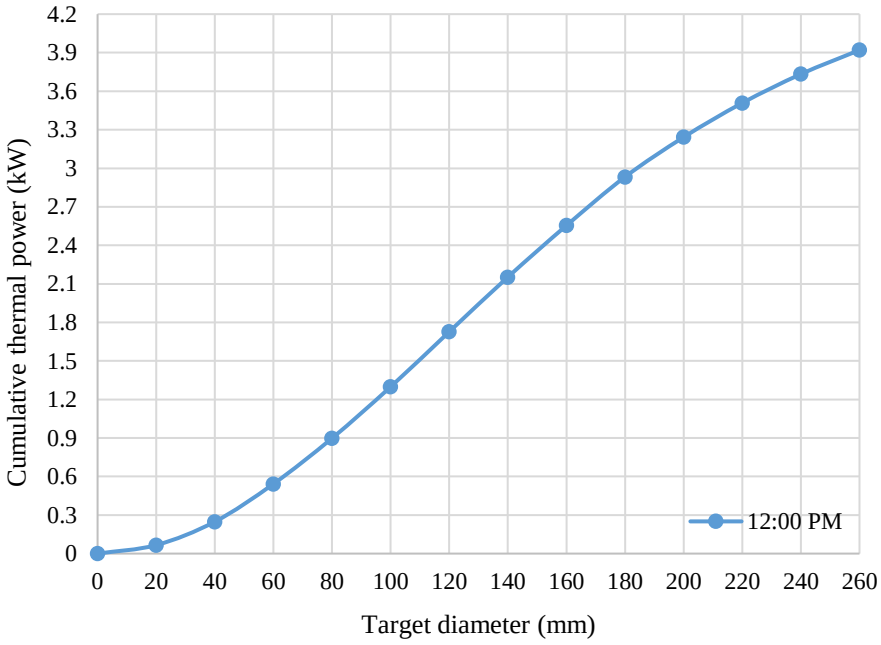

Figure 5-6: Cumulative thermal power vs target diameter for the measured spatial flux distribution obtained at 12:00 pm

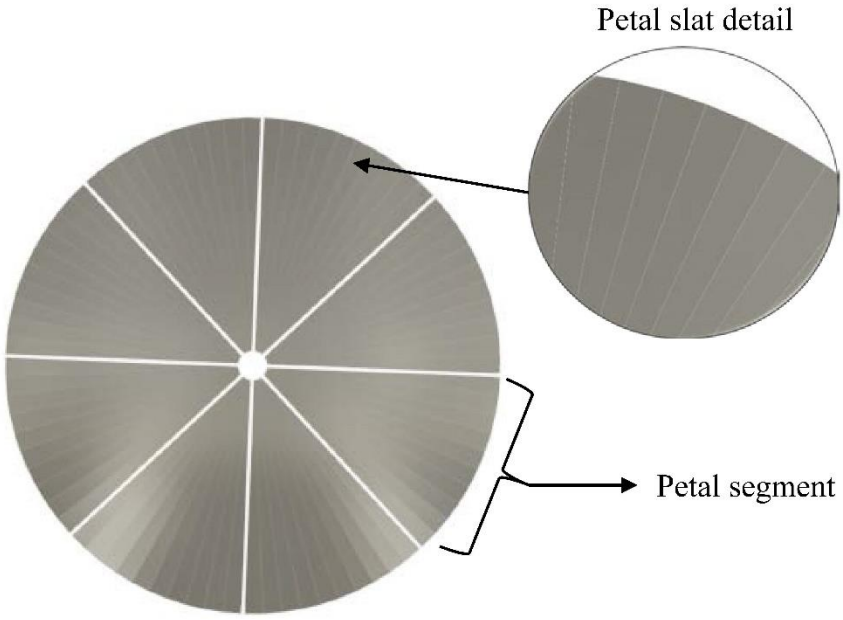

Figure 5-7: CAD model of the SERAFF parabolic concentrator

The heliostat consists of four identical square glass pieces that make up the overall collector surface, providing consistent surface quality. Although slope and specularity errors of flat plate reflectors are reported to be lower than that of parabolic dish reflectors (Bello-ochende et al., 2012), errors with the tracking mechanisms can greatly influence the system's concentration accuracy. The construction of the parabolic concentrator is more complex and is likely to be

the greater contributor of optical errors due to imperfect positioning of the individual reflective surface segments assigned to each petal and incorrect alignment of the eight petals.

The replicated parabolic concentrator (Figure 5-7) replaced the parabolic dish generated in Tonatiuh™ for the idealised ray-tracing analysis, discussed in Chapter 2. Identical slope error (σ_{slope}) and specularity error (σ_{spec}) values were assigned to both the heliostat and parabolic concentrator in the ray-tracing environment. Receiver misalignment error and heliostat tracking error could not be modelled in Tonatiuh™ and therefore were not considered in this analysis. Total standard deviation error (σ_{tot}) magnitudes were calculated with Equation (5.5).

$$\sigma_{tot} = \sqrt{(\sigma_{slope})^2 + (\sigma_{spec})^2} \tag{5.5}$$

Figure 5-8 illustrates the measured spatial flux data and simulated results.

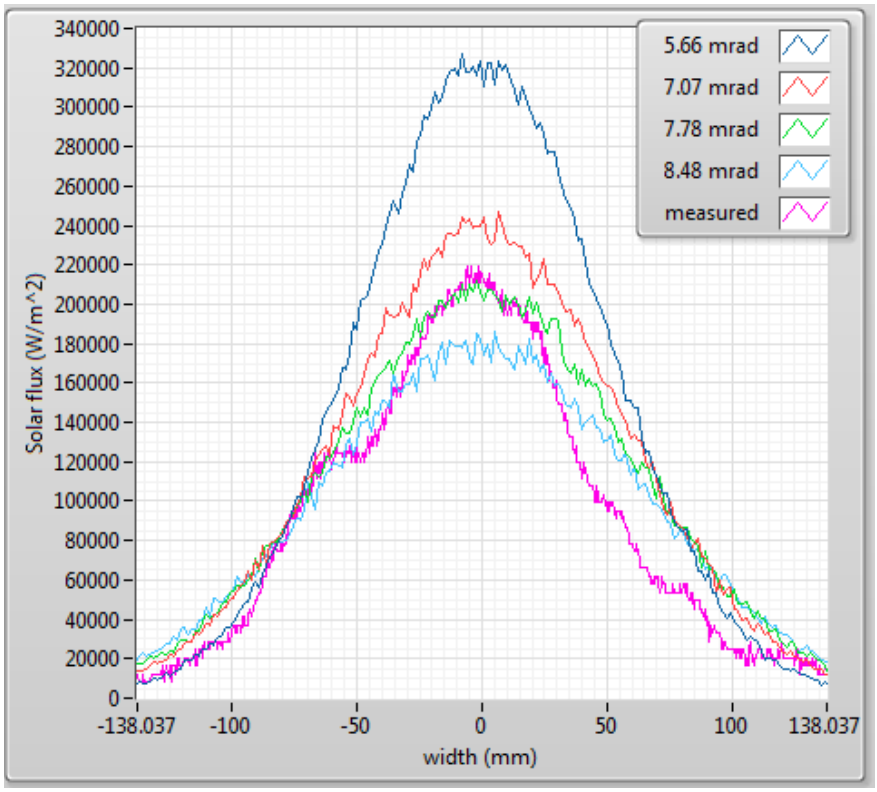

Figure 5-8: Comparison of the measured solar flux distribution at 12:00 pm on 24 October 2018 to normalised simulated results obtained for varying slope and specularity standard deviation errors

The curves of the measured spatial flux data indicated a non-uniform and unpredictable trend compared to the data obtained from the ray-tracing simulations. For this reason, an accurate correlation between the measured and normalised data could not be established. However, the

results indicated a reasonable fit between the normalised curves with total standard deviation errors of 7.78 mrad and 8.48 mrad respectively.

5.3 Pixel measurement errors

To determine the measurement error of the STIMS system, the individual components and procedures incorporated into the spatial flux measurement system were investigated. Conventional indirect flux mapping systems generally categorise errors into camera and Lambertian target errors. Camera errors refer to noise in the signal readout of the pixels in the image sensor. These include camera linearity, dark current and spectral error.

In Chapter 4, the photo response of the Canon EOS 1200D CMOS camera was characterised to investigate the linearity range of the image sensor. These results indicated a camera linearity error of ±0.09% for measurements that fall within the linear portion of the camera's photo response curve. Dark current is another camera pixel error source that generally occurs randomly at each pixel. This error has minimal influence on the flux mapping system's calibration as it is a phenomenon that occurs in the absence of light, as discussed in Chapter 3. However, dark frame ambient lighting images acquired with the neutral density filter mounted on the camera indicated that the effects of dark current are present and therefore must be accounted for. Dark current was calculated to contribute ±0.25% of the overall pixel error.

Spectral errors arise from small changes in the spectral composition of sunlight based on atmospheric conditions and the prevailing airmass. The quantum efficiency of a camera's image sensor is not constant for all wavelengths, and so measurements can be influenced if the spectral composition of sunlight is not coincident with calibration conditions. According to Ulmer et al. (2002) and Xiao et al. (2014), spectral errors contribute ±0.25% to the pixel readout error.

The reflective properties of alumina plasma-sprayed surfaces changes according to the angle of incidence of the ray. For a camera observation angle of approximately 0º between the target surface normal and camera central axis, the intensity of reflected solar radiation measured by the camera is overestimated by +5 % and for larger angles of incidence, up to 45º, measured reflected solar radiation is underestimated by up to -2 % (Ulmer et al., 2002). The angle of incidence of each redirected sunray that strikes the Lambertian target cannot be quantified, therefore, it was not possible to establish an accurate margin of error for the STIMS system. A summary of the described measurement uncertainties is provided in Table 5-2.

These error values are the absolute errors for a given pixel within the image sensor array but are unlikely to be of significant consequence for calibration and measurement of spatial flux as they even out over the whole target area. This is especially true when calculating total

thermal power and blackbody stagnation temperature since the flux values measured by each pixel are averaged over a large area. The total pixel error was calculated by adding the other measurement error values associated with the error sources in the system.

Table 5-2: Pixel measurement error for STIMS

Error source	Measurement error
Camera/optics	
Camera linearity	±0.09 %
Dark current	±0.25 %
Spectral error	±0.25 %
Gardon Gauge heat flux sensor	
Measurement uncertainty	± 3 %
Lambertian target	
Diffuse reflective properties	-2 %... + 5%
Total pixel error	-5.59 %... +8.59 %

Chapter 6 Conclusion

The SERAFF solar furnace was constructed at the University of KwaZulu-Natal's Howard college campus to aid research in various fields, including CSP technology, solar thermal process heating applications and high temperature materials testing. The concentrated radiative energy output of SERAFF defines the energy input for receivers or materials that are to be tested at the facility. It was therefore necessary to quantify SERAFF's energy output so as to facilitate testing. The objective of this research was to design and fabricate a high concentration spatial flux mapping system to characterise the solar flux distribution at SERAFF's focal plane.

The first phase of the design process was to investigate SERAFF's idealised performance parameters through ray-tracing simulations. This provided a theoretical performance model of SERAFF's thermal energy output and spatial constraints. These results were used to conceptualise an appropriate measurement system that met these spatial and quantitative requirements. To this end, an indirect flux mapping system was designed and fabricated to measure the distribution of concentrated solar flux at SERAFF's focal plane. These systems are typically used to measure highly concentrated radiative energy for optical concentrating systems that use natural sunlight. This technique typically involves positioning a Lambertian target at the focal plane of the solar furnace, while a CCD/CMOS image sensor measures the concentrated solar radiation intercepted by the Lambertian target via diffuse reflection.

Image sensor characteristics were investigated to select the appropriate imaging device for this application. Advances in CMOS image sensor technology have placed them on par with CCD technology with respect to performance. For this work, the Canon EOS 1200D CMOS camera was used.

A 500 mm x 500 mm water-cooled Lambertian target was designed to support the parabolic concentrator optimisation procedure. A plasma-spraying technique was used to generate a thin, porous layer of fine alumina particles on an aluminum substrate. This yielded a surface that exhibited near-Lambertian diffuse reflective properties. A conjugate heat transfer analysis was conducted to investigate the effectiveness of the target's closed-loop cooling circuit. The spatial flux results from the Monte Carlo ray-tracing simulations were used as the applied heat flux load to the exposed face of the Lambertian target.

A target-positioning system was designed to mitigate receiver misalignment errors of the solar furnace and improve concentration accuracy of the parabolic concentrator. A mounting fixture was attached to the TPS to accommodate the Lambertian target or any future test articles. Linear actuators were installed onto the designated control axes to incrementally adjust the

target's position within the focal plane. The ideal focal spot location was approximated by moving the water-cooled Lambertian target in directions parallel to the surface normal of the parabolic concentrator, while continuously measuring the spatial flux intercepted by the target. Each image was evaluated qualitatively to determine the ideal location of the focal plane for future measurements.

The photo response curve of the Canon EOS 1200D CMOS camera was characterised. The results revealed that the camera's image sensor incorporate a logarithmic encoding characteristic for measured grayscale intensity values above 63.8% of the sensor's full bit-depth capacity. For measured intensities below this margin, the image sensor responded linearly to incident solar radiation. Light attenuation constraints were implemented to prevent pixel saturation under exposure to SERAFF's elevated radiative output. This was achieved by altering the camera's shutter speed and aperture and by mounting a neutral density filter to the camera lens.

The pixel grayscale intensity output of the CMOS camera was calibrated to represent radiative flux by directly measuring the concentrated solar flux at the focal plane using a circular foil Gardon gauge. The gauge was purchased from Vatell Corporation™ and calibrated using their dual-cavity tube furnace. Image thresholding techniques were used to map the Gardon gauge sensor area in pixel co-ordinates to establish a relationship between the radiative flux measured directly by the Gardon gauge and optically by the CMOS camera. The measurement range of the calibrated CMOS camera was 0 kW/m^2 – 468.19 kW/m^2.

SERAFF's thermal energy output was evaluated on the 24th October 2018. Hourly measurements of the solar flux distributions at the focal plane from 9:00 am to 15:00 pm indicated a peak solar flux range of 190.51 kW/m^2 – 227.78 kW/m^2 and peak thermal power output of 4.22 kW on this particular day. Temporal variations in the sun's radiative output and observer-sun angle influence the performance of the facility and so these results are not representative of the facilities maximum or minimum performance. Comparisons between measured and simulated spatial flux data suggested that effective optical system error falls between 7.78 mrad and 8.48 mrad in terms of total standard deviation error for both the parabolic concentrator and heliostat.

The objective of this study was to design and fabricate a high concentration solar flux mapping system, which was successfully achieved. Quantitative measures of SERAFF's thermal energy output indicated that the optical components of the solar furnace are operating at low efficiencies. Future work should therefore include methods to improve the quality of the parabolic concentrator and solve issues with the heliostat autonomous tracking algorithm. Higher values of solar flux at SERAFF's focal plane can be expected if an accurate algorithm

is used to illuminate the parabolic dish. Degradation of the Lambertian target alumina coating and Gardon gauge colloidal graphite coating may alter the system's calibration. Therefore, periodic recalibration of STIMS must be considered to maintain good measurement accuracy.

References

Alma, E. & Taylor, F. (2000). Lambert's cosine law. In: M. Rea & J. van Derlofske, eds., *Illumination Fundementals,* 1st ed . Troy, New York: Rensselaer, pp. 45

Bailey, D.G. (1995). *Pixel Calibration Techniques*. Technical report. Palmerston North: Massey university, pp. 37-41.

Baldry, M. & Taylor, R. (2016). Prelimanary characterisation of a rooftop solar furnace. In: *Proceedings of 2016 Solar research conference*. Kensington, pp. 1–10.

Ballestrín, J., Rodríguez, J. & Cañadas, I. (2006). Calibration of high-heat-flux sensors in a solar furnace. *Metrologia*, 43, pp. 495–500.

Ballestrín, J., Ulmer, S., Morales, A., Barnes, A., Langley, L. & Rodríguez, M. (2003). Systematic error in the measurement of very high solar irradiance. *Solar Energy Materials and Solar Cells*, 80(3), pp. 375–381.

Ballestrín, J. & Monterreal, R. (2004). Hybrid heat flux measurement system for solar central receiver evaluation. *Energy*, 29(5), pp. 915–924.

Bello-Ochende, T., Meyer, J. & Le Roux, W. (2012). Solar tracking for a parabolic dish used in a solar thermal Brayton cycle . In: *Proceedings of the Postgraduate Symposium 2012*. Stellenbosch, Cape Town: Centre for Renewable and Sustainable Energy Studies (CRSES), pp. 1-9.

Blanco, M., Mutuberria, A., Monreal, A. & Albert, R. (2011). Results of the empirical validation of Tonatiuh at Mini-Pegase CNRS - PROMES facility. In: *Proceedings of SolarPACES 2011*. Granada, Spain, 20-23 September.

Bode, S., Gauche, P. & Landman, W. (2012). The design and testing of a small scale solar flux measurement system for central receiver plant. In: *CRSES Annual Student Symposium*. Stellenbosch, Cape Town: Centre for Renewable and Sustainable Energy Studies (CRSES).

Brooks, M.J., Du Clou, S., van Niekerk, W., Gauche, P., Leonard, C., Mouzouris, M., Meyer, R., van der Westhuizen, N., van Dyk, E. & Vorster, F. (2015). SAURAN : A new resource for solar radiometric data in Southern Africa. *Journal of Energy in Southern Africa*, 26(1), pp. 2–10.

Buie, D., Dey, C. & Bosi, S. (2003). The effective size of the solar cone for solar concentrating systems. *Solar Energy*, 74(5), pp. 417–427.

Buie, D. & Monger, A. (2004). The effect of circumsolar radiation on a solar concentrating system. *Solar Energy*, 76(1–3), pp. 181–185.

Cassim, R., Deena, A. & Levine, G. (2015). *Solar Furnace Primary Concentrator*. Technical report. Durban: University of KwaZulu-Natal, pp. 1-308.

Cho, H.S., Myojin, T., Kawakami, S., Gokon, N. & Kodama, T. (2014). Solar demonstration of thermochemical two-step water splitting cycle using CeO 2 / MPSZ ceramic foam device by 45kWth KIER solar furnace. *Energy Procedia*, 49, pp. 1922–1931.

Ctibor, P., Kraus, L., Tuominen, J., Vuoristo, P. & Chráska, P. (2007). Improvement of Mechanical Properties of Alumina and Zirconia Plasma Sprayed Coatings Induced By Laser Post-Treatment. *Ceramics-Silikáty*, 51(4), pp. 7–9.

Darmont, A. (2009). *Spectral Response of Silicon Image Sensors*. Technical report. Sprimont: Aphesa [online] Available at: https://britastro.org/sites/default/files/attachments/SpectralResponse_WhitePaper_April 09.pdf [Accessed 8 Aug. 2017], pp. 1-13.

de l'Avouerie, R. (2015) *Advanced Coatings, Thermal spraying techniques*. [online] Available at: http://www.advanced-coating.com/english/spraying-plasma.htm. [Accessed: 5 July 2018]

Duncan, G., Nudehi, S., Palumbo, R. & Venstrom, L. (2014). A High-Flux Solar Furnace for Undergraduate Engineering Education and High-Temperature Thermochemistry Research. In: *ASME 2014 8th International Conference on Energy Sustainability*. Boston, USA, pp. 1–7.

Fernández-Reche, J. & Cañadas, I. (2006). PSA Solar furnace : A facility for testing PV cells under concentrated solar radiation. *Solar Energy Materials & Solar Cells*, 90, pp. 2480–2488.

Fossum, E. & Hondongwa, D. (2014). A Review of the Pinned Photodiode for CCD and CMOS Image Sensors. *IEEE Journal of the Electron Devices Society*, 2(3), pp. 33–43.

Funken, K., Pohlmann, B., Lüpfert, E. & Dominik, R. (1999). Application of concentrated solar radiation to high temperature detoxification and recycling processes of hazardous wastes. *Solar Energy*, 65(1), pp. 25–31.

Göhring, F., Bender, O., Röger, M., Nettlau, J. & Schwarzbozl, P. (2011). Flux Density Measurement on Open Volumetric Receivers. In: *Proceedings of SolarPACES 2011*. pp. 1–9.

Goldman, D. (2010). Vignette and exposure calibration and compensation. *IEEE Transactions on Pattern Analysis and Machine Intelligence*, 32(12), pp. 2276–2288.

Gouveia, L. & Choubey, B. (2016). Advances on CMOS Image Sensors. *Sensor review*, 36(3), pp. 231-239.

Guillot, E., Alxneit, I., Ballestrín, J., Sans, J. & Willsh, C. (2014). Comparison of 3 heat flux gauges and a water calorimeter for concentrated solar irradiance measurement. *Energy Procedia*, 49, pp. 2090–2099.

Güven, H. & Bannerot, R.B. (1986). Determination of Error Tolerances for the optical Design of Parabolic Troughs for Developing Countries. *Solar Energy*, 36(6), pp. 535–550.

Haueter, P., Seitz, T. & Steinfeld, A. (1999). Engineering A New High-Flux Solar Furnace for High-Temperature Thermochemical. *Journal of Solar Energy Engineering*, 121(79), pp. 77–80.

Ho, C. & Khalsa, S. (2012). A Photographic Flux Mapping Method for Concentrating Solar Collectors and Receivers. *Journal of Solar Energy Engineering*, 134(4), pp. 1-8

Hoang, T., Pan, B., Nguyen, D. & Wang, Z. (2010). Generic gamma correction for accuracy enhancement in fringe-projection profilometry. *Optics Letters*, 35(12), pp. 1992–1994.

Iqbal, M. (1983). The solar constant and its spectral distribution. In: M. Iqbal, ed., *An Introduction to Solar Radiation*, 1st ed. Academic Press, pp. 43–58.

Jain, U. (2016). *Characterization of CMOS Image Sensor*. Masters in Science thesis. Delft University of Technology.

Khan, A., Govender, K. & van Niekerk, S. (2016). *Solar Furnace Design Enhancements*. Technical report. Durban: University of KwaZulu-Natal, pp. 1-253.

Kluthe, C. & Kollenberg, W. (2013). Thermal shock behaviour of paper-derived alumina ceramics. *Materials Science and Engineering*, 44(12), pp. 997–1004.

Krueger, K.R. (2012). *Design and Characterization of a Concentrating Solar Simulator*. PhD thesis. University of Minnesota, Minneapolis.

Langley, L. & Barnes, A. (2006). Heat flux sensors : Calorimeters or radiometers? *Solar Energy*, 80, pp. 1314–1320.

Lee, H., Chai, K., Kim, J., Lee, S., Yoon, H., Yu, C. & Kang, Y. (2014). Optical performance evaluation of a solar furnace by measuring the highly concentrated solar flux. *Energy*, 66, pp. 63–69.

Levêque, G., Bader, R., Lipiński, W. & Haussener, S. (2017). High-flux optical systems for solar thermochemistry. *Solar Energy*, 156, pp. 133–148.

Llorente, J., Ballestrín, J. & Vázquez, A.J. (2011). A new solar concentrating system: Description, characterization and applications. *Solar Energy*, 85(5), pp. 1000–1006.

Lüpfert, E., Heller, P., Ulmer, S., Monterreal, R. & Fernández, J. (2000). Concentrated solar radiation measurement with video image processing and online fluxgage calibration. In: *Solar Thermal 2000 International Conference*. Sydney, Australia, pp. 241–246.

Meier, A. & Sattler, C. (2009). *Solar Fuels from Concentrated Sunlight*, Tabernas, Spain, pp. 4-34

Meyen, S., Lüpfert, E. & Kennedy, C. (2010). Standardization of Solar Mirror Reflectance Measurements. In: *Proceedings of SolarPACES 2010*. Perpignan, France, pp. 1–11.

Meynants, G., Dierickx, B., Alaerts, A., Uwaerts, D., Cos, S., Scheffer, D. & Noble, S. (2003). A 35 mm 13 . 89 Million Pixel CMOS Active Pixel Image Sensor. In: *IS&Ts 2003 PICS Conference*. Rochester, New York: Eastman Kodak CO., pp. 13–16.

Mojiri, A., Stanley, C. & Rosengarten, G. (2015). Close range radiometry for quantifying the spatial distribution of illumination on flat surfaces. *Solar Energy*, 122, pp. 429–439.

Mouzouris, M., Roberts, L. & Brooks, M. (2012). Heat transfer analysis for high-flux solar measurements using a flat plate calorimeter. *R & D Journal of the South African Institution of Mechanical Engineering*, 27, pp. 10–22.

Neumann, A. & Groer, U. (1996). Experimenting with Concentrated Sunlight Using the DLR Solar Furnace. *Solar Energy*, 58(4), pp. 181–190.

Neumann, A., Jones, S. & Schmitt, G. (2002). Representative Terrestrial Solar Brightness Profiles. *Journal of Solar Energy Engineering*, 124, pp. 198–204.

NREL, (2003). *Solar position algorithm for solar radiation applications*. [online] Available at: https://rredc.nrel.gov/solar/codesandalgorithms/spa/ [Accessed: 5 Mar. 2016]

Oliveira, F., Shohoji, N., Fernandes, J. & Rosa, L. (2005). Solar sintering of cordierite-based ceramics at low temperatures. *Solar Energy*, 78(3), pp. 351–361.

Osório, T., Horta, P., Larcher, M., Pujol-nadal, R., Hertel, J., van Rooyen, D., Schneider, S., Benitez, D., Frein, A. & Denarie, A. (2016). Ray-Tracing Software Comparison for Linear Focusing Solar Collectors. In: *AIP conference proceedings*. pp. 1–8.

Pawlowski, L. (1991). The properties of plasma sprayed aluminium-aluminium oxide cermets. *Surface and Coatings Technology*, 48(3), pp. 219–224.

Peric, M. & Ferguson, S. (2004). *The advantage of polyhedral meshes*. [online] pp 1-2. Available at: www.cd-adapco.com [Accessed 15 Aug. 2016].

Perumall, P. (2016). *Development of a Solar Furnace Heliostat*. Masters in Science thesis, University of KwaZulu-Natal, Durban.

Perumall, P., Pitot de la Beaujardiere, P. & Brooks, M. (2015). An Introduction to the University of KwaZulu-Natal's Solar Energy Research Amplified Flux Facility – SERAFF. *R & D Journal of the South African Institution of Mechanical Engineering*, (31), pp. 1–9.

Porter, W., Kopp, B., Dunlap, J., Widenhorn, R. & Bodegom, E. (2008). Dark current measurements in a CMOS imager. In: *SPIE 6816, Sensors, Cameras, and Systems for Industrial/Scientific Applications IX*. pp. 1-8.

Relf, C. (2004). *Image Acquisition and Processing with LabVIEW*, 1st ed., Bosa Roca, USA: CRC Press, pp. 85-163.

Rhem, L. (2015). *DxOMARK, Photons to Photos*. [online] Available at: http://www.photonstophotos.net/Charts/Sensor_Characteristics.htm [Accessed: 10 July 2016].

Rodríguez, J., Cañadas, I. & Zarza, E. (2014). PSA vertical axis solar furnace SF5. *Energy Procedia*, 49, pp. 1511–1522.

Röger, M., Herrmann, P., Ebert, M., Prahl, C., Ulmer, S. & Göhring, F. (2011). Flux Density Measurement on Large-Scale Receivers. In: *SolarPACES 2011*. pp. 20–23.

Röger, M., Herrmann, P., Ebert, M., Prahl, C., Ulmer, S. & Göhring, F. (2014). Techniques to Measure Solar Flux Density Distribution on Large-Scale Receivers. *Journal of Solar Energy Engineering*, 136(3), pp. 1-10.

Safai, S. & Herman, H. (1977). Microstructural investigation of plasma-sprayed aluminium coatings. *Thin solid films*, 45, pp. 295–307.

Shuai, Y., Xia, X.L. & Tan, H.P. (2008). Radiation performance of dish solar concentrator/cavity receiver systems. *Solar Energy*, 82(1), pp.13–21.

Sierra, C. & Vázquez, A.J. (2006). Dry sliding wear behaviour of nickel aluminides coatings produced by self-propagating high-temperature synthesis. *Intermetallics*, 14(7), pp.848–852.

SolarPACES, (2000). *Catalog of Solar Heliostats IEA-Solar Power and Chemical Energy Systems Task III : Solar Technology and Applications*, Technical report, pp. 1-4.

Stine, B. & Harrigan, R. (1985). *Solar Energy Fundamentals and Design*, New York: John Wiley & Sons Inc., pp. 181-211.

Strachan, J. & Houser, R., (1993). *Testing and evaluation of large-area heliostats for solar thermal applications*. Technical report. Albuquerque, New Mexico, pp. 19-30.

Taylor, S. (1998). *CCD and CMOS Imaging Array Technologies : Technology Review*. Technical report. Cambridge, pp. 1-14.

Toru, D., De Sousa Meneses, D., Echegut, P. & Bianchi, L. (2016). Al2O3 / Al Cermets by Plasma Spraying : Optical Response of Experimental and Numerically Represented Materials Al 2 O 3 / Al Cermets by Plasma Spraying : Optical Response of Experimental and Numerically Represented Materials. *Journal of Thermal Spray Technology*, 25(1), pp. 384–391.

Ulmer, S. et al. (2002). Beam Characterization and Improvement with a Flux Mapping System for Dish Concentrators. *Journal of Solar Energy Engineering*, 124, p.182.

Ulmer, S., Reinalter, W., Heller, P., Lüpfert, E., Martínez, D. (2004). Calibration corrections of solar tower flux density measurements. *Energy*, 29, pp. 925–933.

van Bakel, B., Brooks, M. & Pitot de la Beaujardiere, J. (2016). Development of a high concentration solar flux mapping system. In: *Proceedings of the 4th Southern African Solar Energy Conference*. Stellenbosch, Centre for renewable energy stidies (CRSES), pp. 1–7.

Vatell, (2011). *Use of the Thermogage Circular Foil Heat Flux Gauge*. [online] Christansburg, Virginia, pp. 1-3. Available at: http://vatell.com/vatellwebfiles/Use%20of%20Thermogage%20v2.pdf [Accessed 4 Mar. 2017].

Vázquez, A., Rodriguez, G. & de Damborenea, J. (1991). Surface treatment of steels by solar energy. *Solar Energy Materials*, 23, pp. 212–217.

Veludandi, N. (2015). *CMOS active pixel sensor*. Master's in Science thesis. New Mexico State University, Las Cruces.

Virto, A., Vila, L., Rodrigo, T., Matorras, F., Figueroa, C., Calvo, E., Calderón, A., Arce, P., Oller, J., Molinero, A., Josa, M., Fuentes, J., Ferrando, A., Fernández, M., Barcala, J. (2002). *Study of CMOS Image Sensors for the Alignment System of the CMS Experiment*. Technical report. Universidad de Cantabria, pp. 1-15.

Wheaton, B. (2009). Photoelectric effect. In G. Greenberger, K. Hentschel, & F. Weinert, eds. *Compendium of Quantum Physics*. Berlin, Heidelberg: Springer, pp. 472–475.

Wong, C. & Chong, K. (2016). Solar flux distribution study of non-imaging dish concentrator using linear array of triple-junction solar cells scanning technique, 125, pp. 86–98.

Xiao, G., Guo, K., Xu, W., Ni, M., Luo, Z., Cen, K. (2014). An improved method of Lambertian CCD-camera radiation flux measurement based on SMARTS (simple model of the atmospheric radiative transfer of sunshine) to reduce spectral errors. *Energy*, 67, pp. 74–80.

Xu, Y. (2015). *Fundamental Characteristics of a Pinned Photodiode CMOS Pixel*. PhD thesis. Delft University of Technology, Delft.

Zheng, Y. et al. (2009). Single-Image Vignetting Correction. *IEEE Transactions on Pattern Analysis and Machine Intelligence*, 31(12), pp. 2243–2256.

APPENDIX A Ray-tracing simulation results

Figure A-1 shows the results for the Monte Carlo ray tracing simulations for the winter solstice (22 June) and summer solstice (22 December) at 12:00 pm.

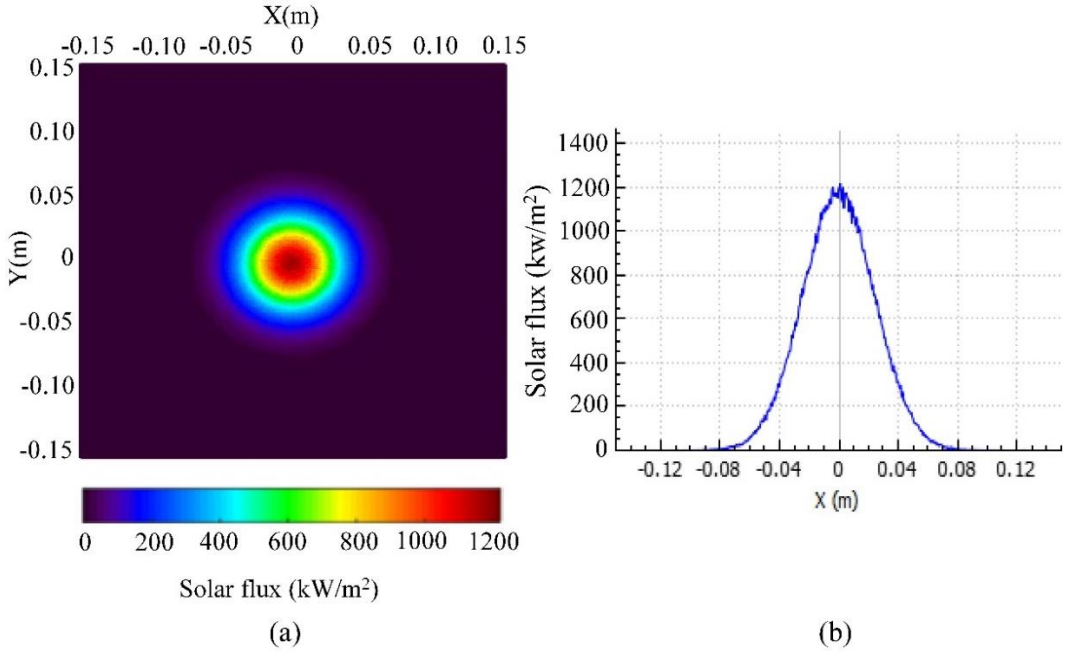

Figure A-1: Spatial flux results (a) and 2-dimensional solar flux intensity curve (b) for the winter solstice ray-tracing simulations

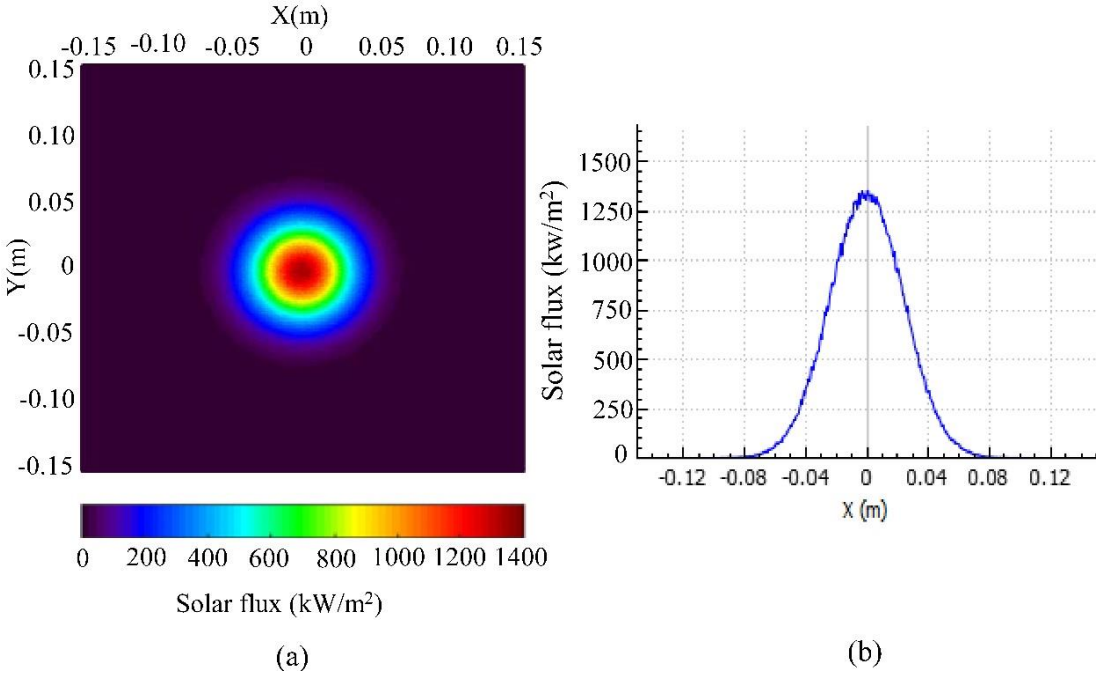

Figure A-2: Spatial flux results (a) and one-dimensional solar flux intensity curve (b) for the summer solstice ray-tracing simulations

APPENDIX B Water-cooled Lambertian target CAD drawings

Figures B-1 and B-2 are the assembly drawings for the water-cooled Lambertian target.

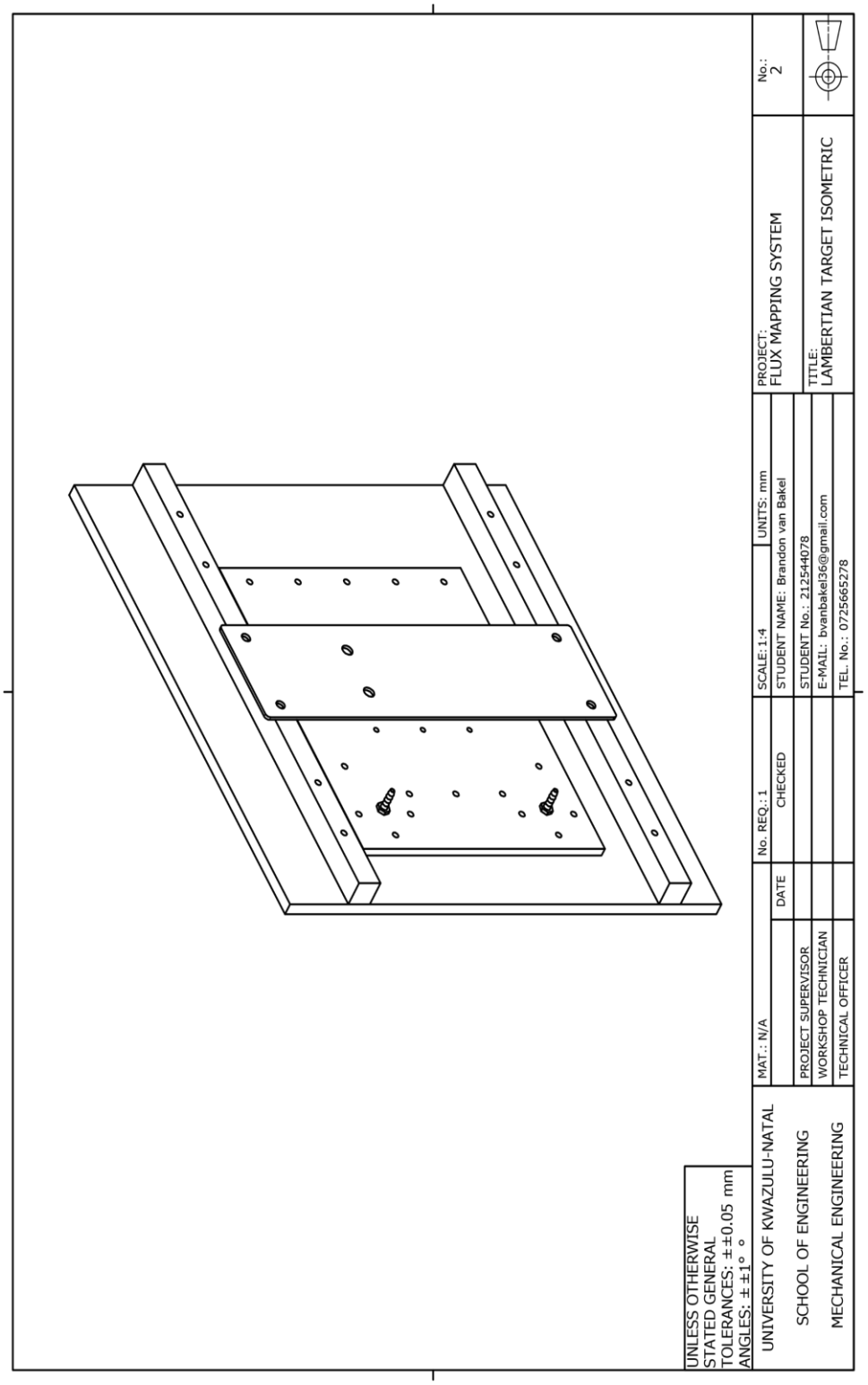

Figure B-1: Water-cooled Lambertian target isometric drawing

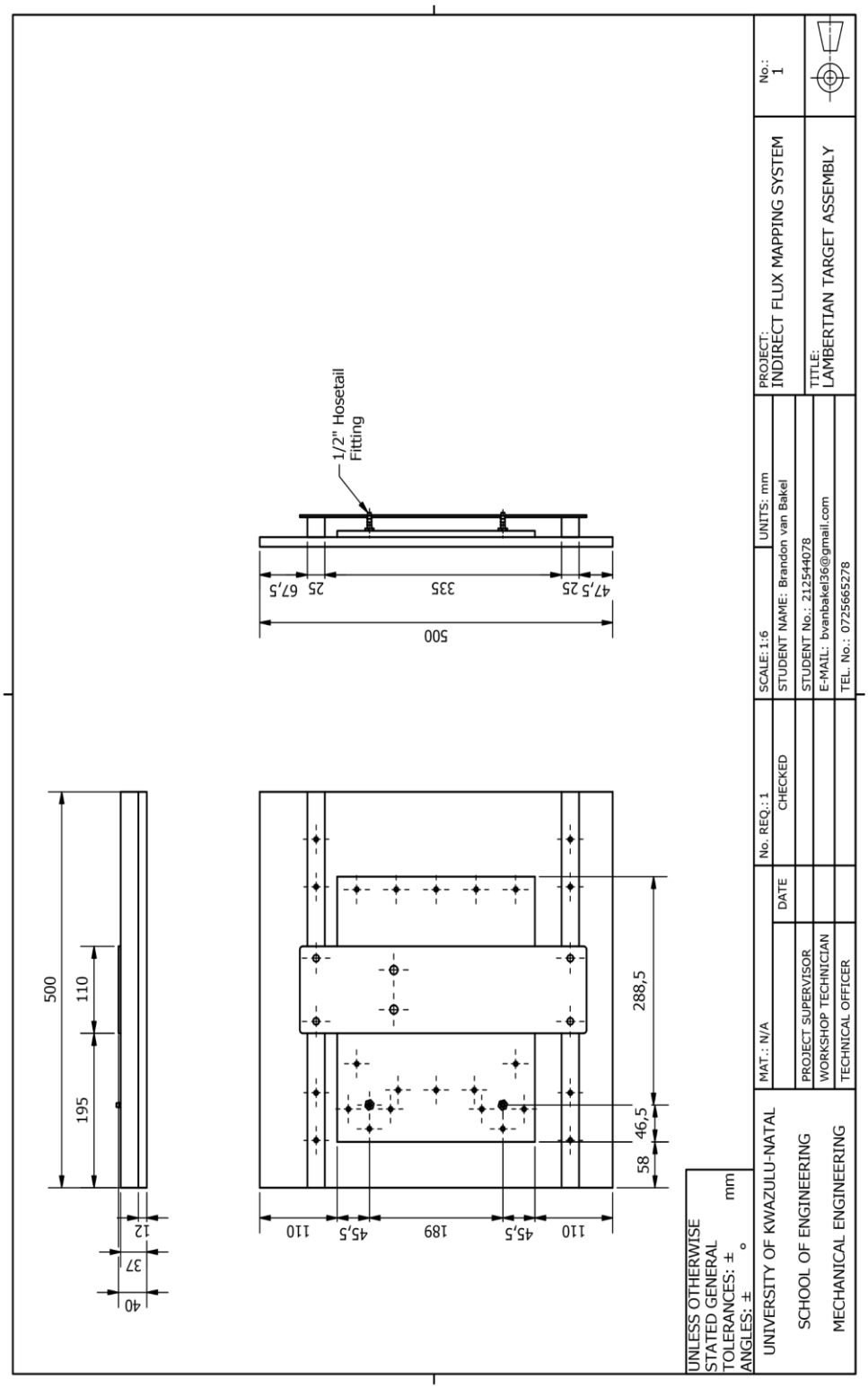

Figure B-2: Water-cooled Lambertian target assembly drawing

APPENDIX C Target positioning system user interface

Figure C-1 shows the user-controlled interface for manual control of the target positioning system (TPS) linear actuators.

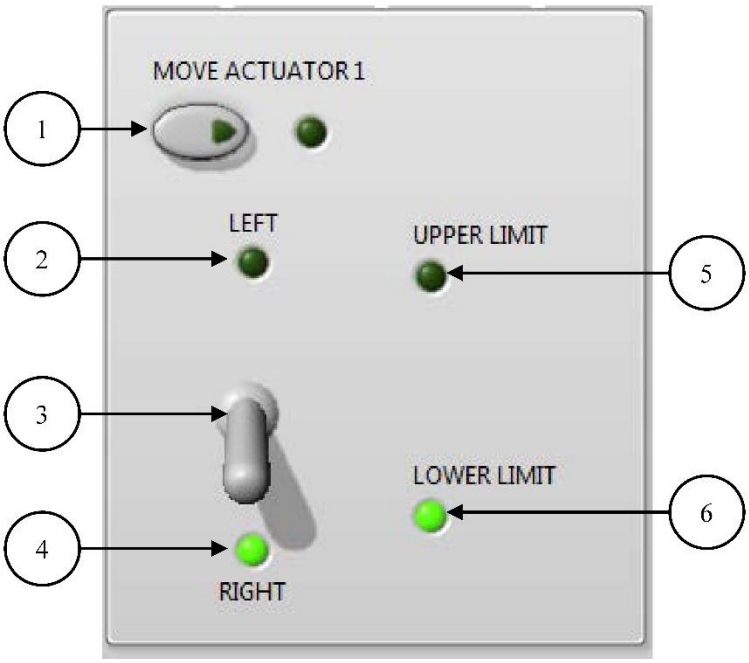

Figure C-1: Target positioning system linear actuator control panel within the SERAFF LabVIEW control software

The description of all the controls and indicators displayed in Figure C-1 are as follows:

1. Toggle button to enable linear actuator motion in the specified direction
2. Left/forward motion True or False indicator
3. Linear actuator direction toggle switch
4. Right/backward motion True or False indicator
5. Upper limit switch True or False indicator. If True, the linear actuator can only be moved again if the direction toggle switch is set to move right/back
6. Lower limit switch True or False indicator. If True, the linear actuator can only be moved again if the direction toggle switch is set to move left/forward

APPENDIX D CMOS camera photo response images

Figures D-1 and D-2 shows the grayscale images acquired for the photo response characterisation of the canon EOS 1200D CMOS digital camera experiment.

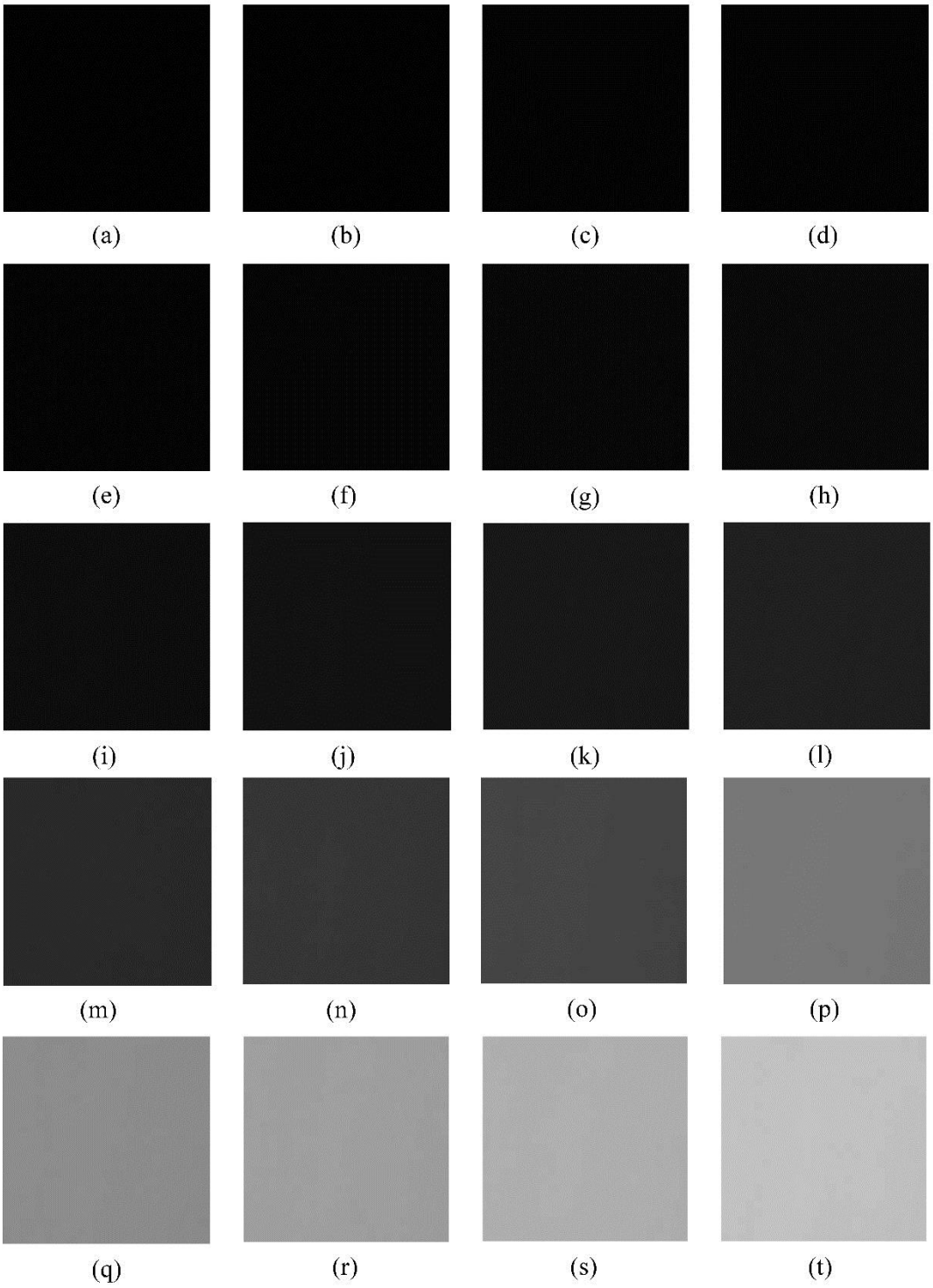

Figure D-1: 100-pixel square region of the Lambertian target for the Canon EOS 1200D photo response characterisation experiment (images ‘a’ to ‘t’ are shown)

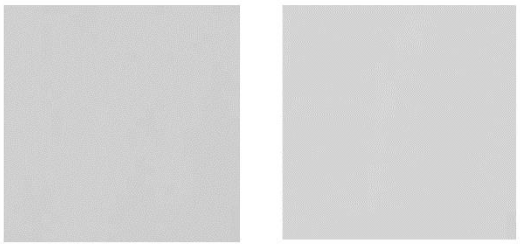

Figure D-2: 100-pixel square region of the Lambertian target for the Canon EOS 1200D photo response characterisation experiment (images ‘u’ and ‘v’ are shown)

The exposure time and measured grayscale intensity of all the images obtained during the photo response characterisation experiment are given in Table D-1.

Table D-1: Results for the images recorded by the Canon EOS 1200D CMOS camera for the phot response characterisation experiment

Image	Exposure time (s)	Grayscale intensity
a	0	0
b	0.00025	1436
c	0.000313	1653
d	0.0004	2074
e	0.0005	2747
f	0.000625	3394.9
g	0.0008	4435
h	0.001	5434
i	0.000125	7010
j	0.001563	8571
k	0.002	10742
l	0.0025	13429
m	0.003125	16256
n	0.004	19881
o	0.00625	33139
p	0.008	41857
q	0.01	46068
r	0.0125	49604
s	0.016667	53752
t	0.02	56819
u	0.025	57761
v	0.1	65535

APPENDIX E Region of interest user interface

Figure E-1 shows the front panel of the region of interest (ROI) controls used to manually specify image boundary constraints.

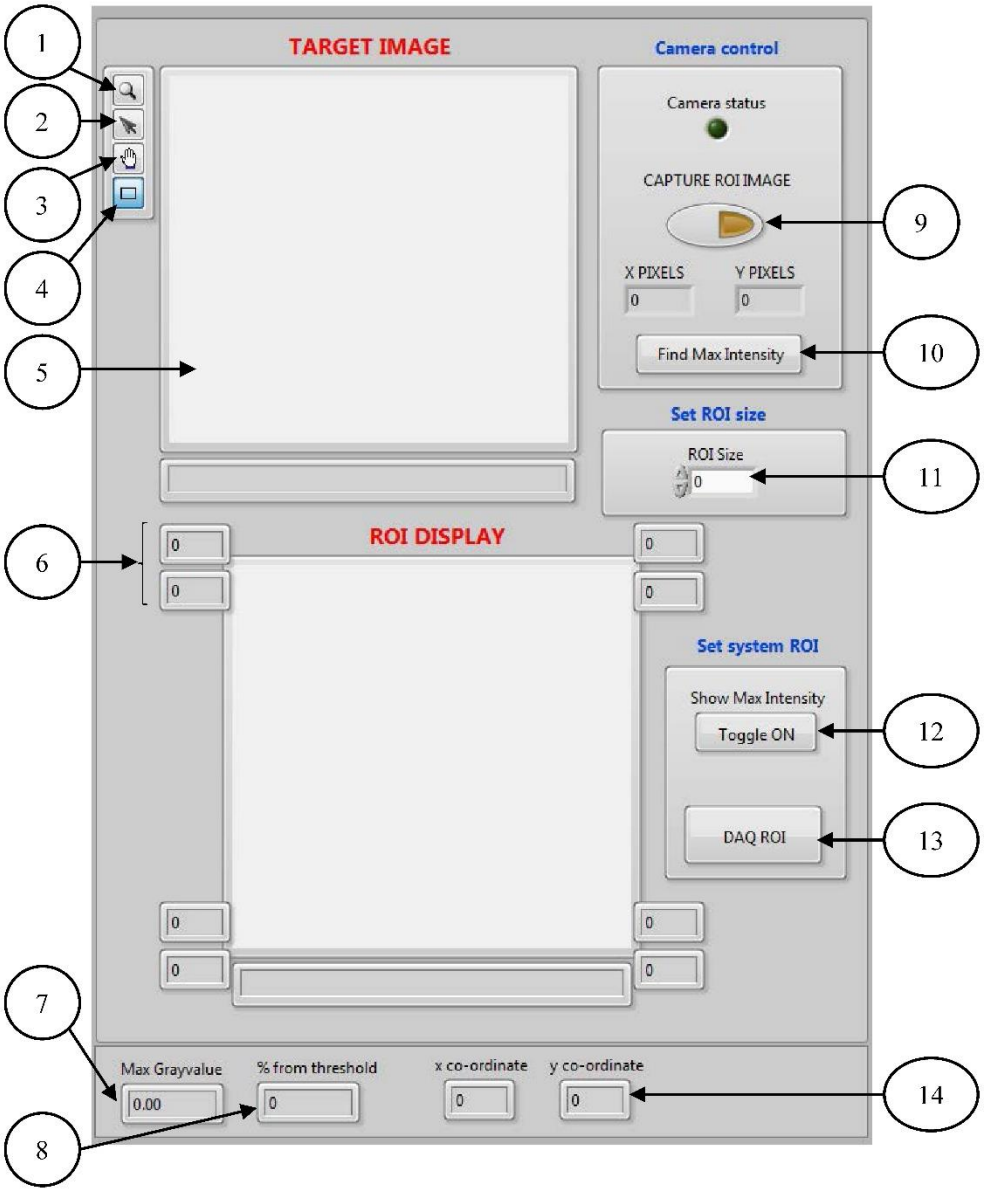

Figure E-1: Region of interest (ROI) control panel within the SERAFF LabVIEW control software

The description of all the controls and indicators displayed in Figure E-1 are as follows:

1. Zoom select tool for an image within the Target Image view window
2. Pixel select tool for an image within the Target Image view window
3. Pan select tool for an image within the Target Image view window

4. Manual rectangle ROI draw tool for an image within the Target Image view window
5. Target image view window
6. X and Y pixel co-ordinates at the four corners of the extracted ROI image
7. Max grayscale intensity within the extracted ROI image
8. Percentage from reaching pixel saturation (out of 65 553 for a 16-bit image)
9. Captures an image of the camera's current viewing plane (this only works if the Canon EOS 1200D CMOS camera is connected to the PC)
10. Searches the image within the ROI display view window and draws a 25-pixel square around the pixel with the maximum recorded grayscale intensity. The pixel co-ordinates of this region are stored for later use
11. User input specification of the size of a square ROI built around the centre of the image within the Target image view window. The extracted ROI is immediately displayed in the ROI display view window when this value is changed
12. Displays the 25 square pixel region at the co-ordinates obtained when the user last pressed the Find max intensity control
13. Stores the current co-ordinates of the ROI in the ROI display view window. This sets the ROI for actual spatial flux measurements

APPENDIX F Gardon gauge calibration certificate

Figures F-1 and F-2 shows the calibration certificate and linear regression curve for the circular foil Gardon gauge heat flux sensor respectively.

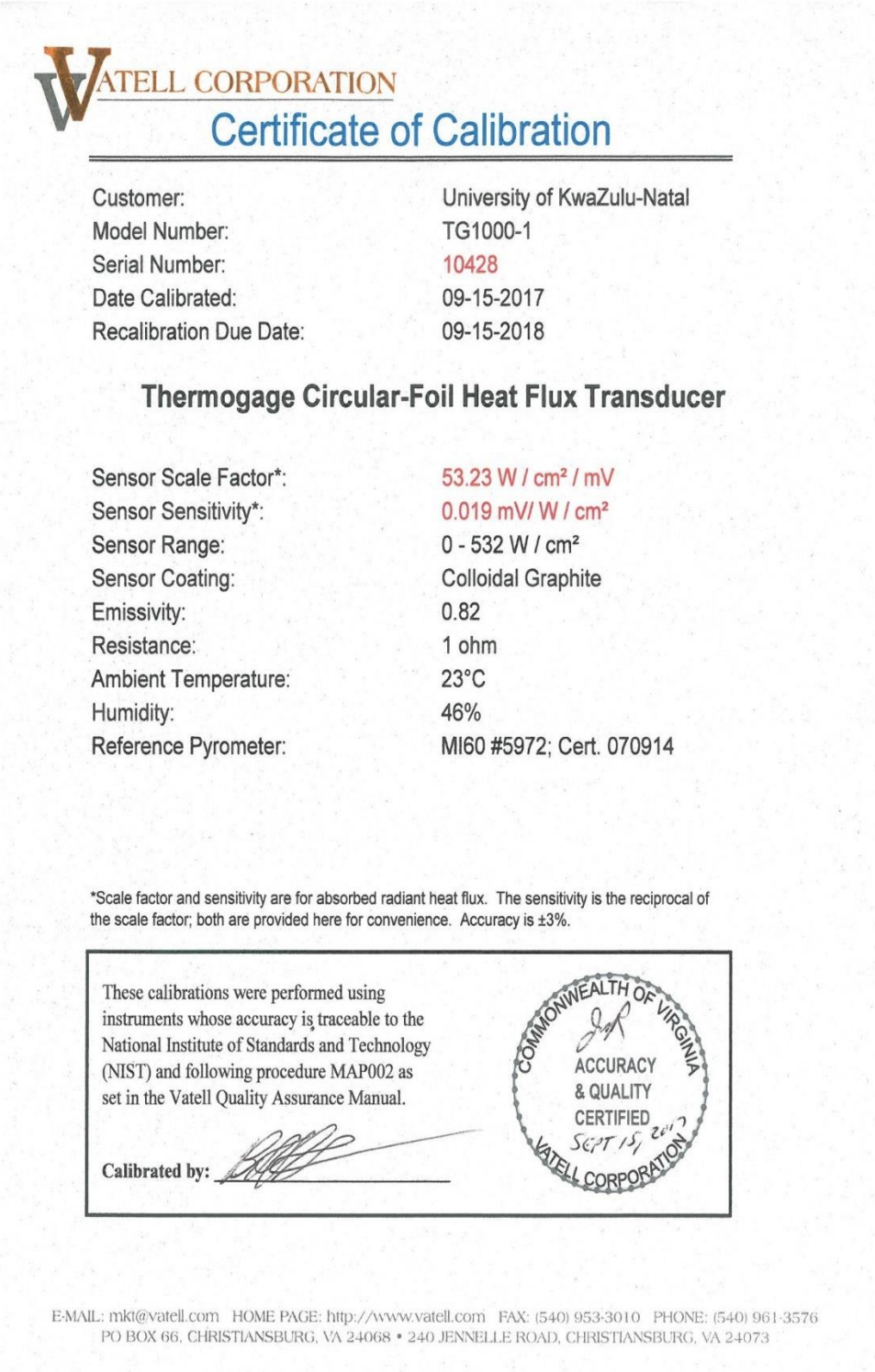

VATELL CORPORATION

Certificate of Calibration

Customer:	University of KwaZulu-Natal
Model Number:	TG1000-1
Serial Number:	10428
Date Calibrated:	09-15-2017
Recalibration Due Date:	09-15-2018

Thermogage Circular-Foil Heat Flux Transducer

Sensor Scale Factor*:	53.23 W / cm² / mV
Sensor Sensitivity*:	0.019 mV/ W / cm²
Sensor Range:	0 - 532 W / cm²
Sensor Coating:	Colloidal Graphite
Emissivity:	0.82
Resistance:	1 ohm
Ambient Temperature:	23°C
Humidity:	46%
Reference Pyrometer:	MI60 #5972; Cert. 070914

*Scale factor and sensitivity are for absorbed radiant heat flux. The sensitivity is the reciprocal of the scale factor; both are provided here for convenience. Accuracy is ±3%.

These calibrations were performed using instruments whose accuracy is traceable to the National Institute of Standards and Technology (NIST) and following procedure MAP002 as set in the Vatell Quality Assurance Manual.

Calibrated by:

COMMONWEALTH OF VIRGINIA ACCURACY & QUALITY CERTIFIED SEPT 15, 2017 VATELL CORPORATION

E-MAIL: mkt@vatell.com HOME PAGE: http://www.vatell.com FAX: (540) 953-3010 PHONE: (540) 961-3576
PO BOX 66, CHRISTIANSBURG, VA 24068 • 240 JENNELLE ROAD, CHRISTIANSBURG, VA 24073

Figure F-1: Calibration certificate for the TG1000-1 circular-foil Gardon gauge purchased from Vatell Corporation™

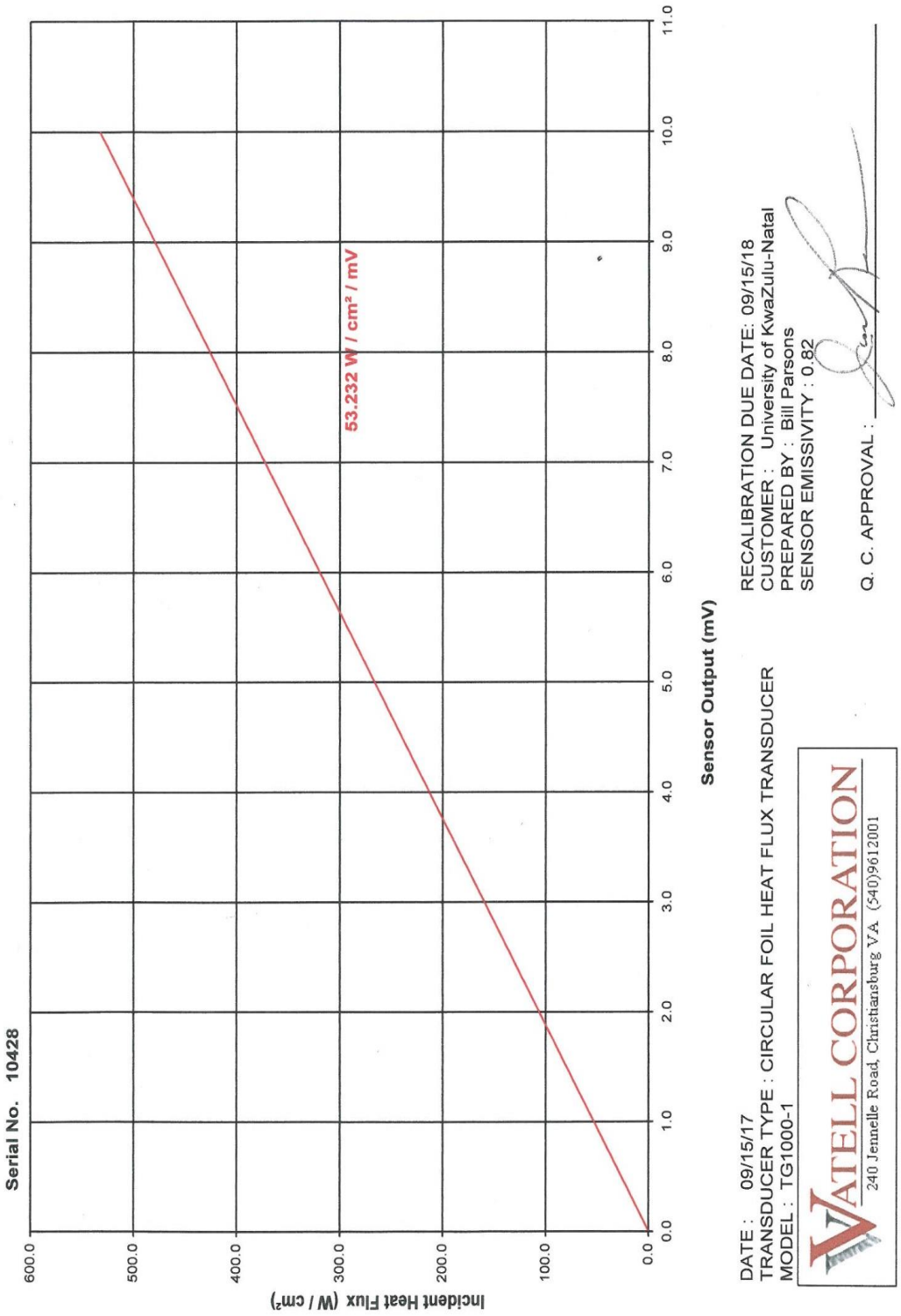

Figure F-2: Linear regression calibration curve of the TG1000-1 circular-foil Gardon gauge purchased from Vatell Corporation™

APPENDIX G Spatial flux plots

Figure G-1 and G-2 shows the one-dimensional spatial flux plots acquired on 24 October 2018.

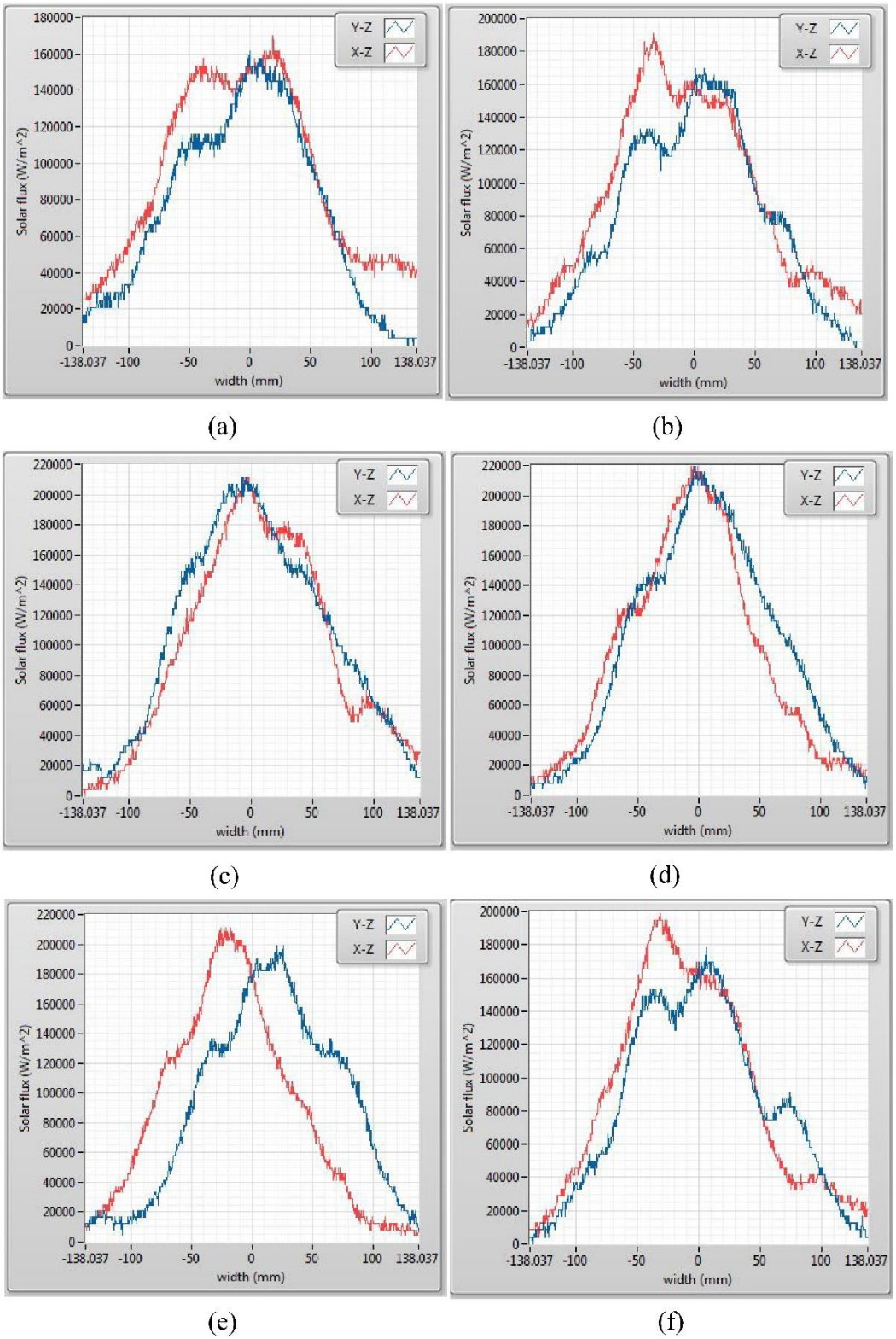

Figure G-1: One-dimensional x-y intensity plots for the spatial flux measurements obtained at (a) 9:00 am, (b) 10:00 am, (c) 11:00 am, (d) 12:00 pm, (e) 13:00 pm, (f) 14:00 pm

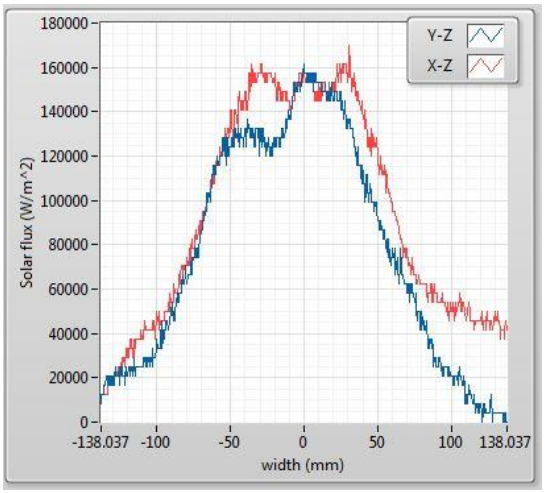

Figure G-2: One-dimensional x-y intensity plots for the spatial flux measurement obtained at 15:00 pm